Characteristics of Scintillating GPS Signal at High Latitudes during Solar Minima

by

Sajan Chandra Mushini

Master of Science, Chalmers University of Technology, 2005
Bachelor of Technology, Nagarjuna University, 2003

A DISSERTATION SUBMITTED IN PARTIAL FULFILLMENT OF THE REQUIREMENTS FOR THE DEGREE OF

Doctor of Philosophy

In the Graduate Academic Unit of Physics

Supervisor(s):	P. T. Jayachandran, Ph.D., Physics
Examining Board:	AbdelHaq Hamza, Ph.D., Physics,
	William Ward, Ph.D., Physics,
	Richard Langley, Ph.D., Geodesy and Geomatics
External Examiner:	Anthea. J. Coster, Ph.D., Physics, MIT, USA

This Dissertation is accepted by the

Dean of Graduate Studies

THE UNIVERSITY OF NEW BRUNSWICK

October, 2012

Dedication

Dedicated to Dr. Girija Vani Mushini, Dr. Vivekananda Murthy Mushini, Jyothi Kandregula, Sameera Mushini, Navneet Chalagalla, Suresh Garapati, Ravi Chandra Vattipalli

Abstract

Occasionally, due to electron density irregularities in the ionosphere, trans-ionospheric radio signals, like GPS signals, can experience rapid amplitude and phase fluctuations that are called scintillations. Due to these rapid fluctuations in the GPS signals, GPS receivers have trouble keeping track of the signals and thus position and navigational errors are introduced. Hence there is a need to study these scintillations to understand the ionospheric irregularities that cause scintillation as well as to minimize errors induced due to scintillation. In order to quantify scintillation, commonly used scintillation indices are σ_ϕ and S_4 that represent phase scintillation and amplitude scintillation, respectively. Before calculating these indices, GPS signals are usually detrended using a 6th order Butterworth filter with 0.1 Hz cut-off frequency. Accuracy and validity of these scintillation indices depend heavily on the detrending method used and the selection of the cutoff frequency of the associated filter. It is shown that using the default 0.1 Hz cutoff frequency for detrending high latitude GPS data lead to erroneous artifacts as this cut-off frequency was designed for mid- and low-latitudes. These arti-

facts are called "phase scintillation without amplitude scintillation". Taking into account the non-stationary aspect of the GPS scintillation signal, a wavelet-based filter is introduced in this dissertation. The performance of the Butterworth filter is evaluated and compared with this new wavelet-based detrending filter using GPS data from Canadian High Arctic Ionospheric Network (CHAIN). It was observed that in detrending high-latitude GPS data, the wavelet filter performed better than the time-invariant Butterworth filter. An improved phase-scintillation index, σ_{CHAIN}, is also introduced in this dissertation, which when calculated using the wavelet-detrended high latitude GPS data introduced no "phase scintillation without amplitude scintillation". Using this new wavelet-detrending method and the new phase scintillation index, two years (March 2009 to March 2011) of CHAIN data was analysed to create scintillation climatology. An annual cycle of scintillation occurrence is observed with maximum in winter and minimum in summer. Signal characteristics like the fading rate, average irregularity size, and power spectra were also calculated for GPS scintillations observed at high latitudes. The average spectral index value for both amplitude and phase scintillation was observed to be around 1.75 and an elevation dependence of the spectral index was also observed. The average characteristic size of irregularities was found to be around 50 m. These signal characteristics and the scintillation climatology are useful in creating both local and global scintillation models which help in predicting and mitigating scintillation.

Acknowledgments

"*Matru devo bhavah,*

Pitru devo bhavah,

Acharya devo bhavah" : Taittiriya Upanishad

This sloka/verse literally means "The Mother is God, the Father is God, the Teacher is God" and I would like to start my acknowledgments in this order. My special gratitude goes to my parents who have worked hard to get me to this stage in life. I would like to thank them for their never ending love, support and encouragement in what ever decision I have made in life. I would like to express my sincere gratitude to my supervisor Dr. P. T. Jayachandran for his constant support, advice and patience over the past several years. Prof. Jayachandran has provided me every opportunity to attend conferences, participate in field work, and gain the knowledge and experience necessary for an aspiring researcher. I would like to thank Prof. Richard Langley, Prof. Abdelhaq Hamza, Prof. John MacDougall, Dr. Paul Prikryl and Prof. William Ward for their constant support, advice and cri-

tique which helped me become a better student of this field. My gratitude also goes to my previous teachers especially Dr. Werner Singer, Dr. Gary Smith, Dr. K. M. Prasad, Dr. Habibullah Khan and Dr. Chalapathi Rao.

I would like to thank Richard Chadwick for his technical support especially with ACEnet. Without him this work would have taken ages. Todd Kelly and Luke Tymowski for their technical support and fun. Adnane Osmane, Chris Watson, Damien Farthomme and Samaneh Sadighi for sharing their knowledge. David Themens, Nathan Hetherington and Eric Webster for their IDL programs. Wendy Wells for her time to proof read my thesis.

Many thanks go to Sameera Mushini, Narayana Kumar Dommeti, Ohm Prakash, Rajat Thomas, Subhani, Tulasi aunty, Rao uncle, Ahmed, Rama Krishna, Nagesh, Praveen, Patricia, Jayakumar, Pavithra, Gul, Akram, Surya, Krishna, Diwakar, Vikram, Amar, Sai, Shalini, Thamer, Khaddour, Hichem, Racheal, Sam, Duncan, Jeff, Dragon, Ayesha, Ranjit, Nirmal, Vaibhav, Ansi, Swapnil Thackeray and many more for making my stay in Fredericton a wonderful experience. Most importantly, special gratitude goes to my wife Jyothi Kandregula for keeping up with me, supporting and loving me in all aspects of the life. Thanks for always being there for me.

My PhD degree was financially supported by the Natural Sciences and Engineering Research Council of Canada (NSERC). Infrastructure funding for

CHAIN was provided by the Canada Foundation for Innovation and the New Brunswick Innovation Foundation. CHAIN operation is conducted in collaboration with the Canadian Space Agency. Science funding is provided by the Natural Sciences and Engineering Research Council of Canada.

Table of Contents

List of Tables

List of Figures

List of Abbreviations

GPS	Global Positioning System
CADI	Canadian Advanced Digital Ionosonde
IPP	Ionospheric Pierce Point
TEC	Total Electron Content
CHAIN	Canadian High Arctic Ionospheric Network

Chapter 1

Introduction and Thesis Outline

1.1 Introduction

The Global Positioning System (GPS), a space-based satellite navigation system that provides location and time information, became a household name in recent times. GPS-based industry has expanded in the last decade and is worth billions in dollars worldwide. We now use GPS in many diverse applications such as in defense where millimeter accuracy is needed or to navigate in a city where the accuracies of the order of hundreds of meters is sufficient. As we grow more dependent on satellite navigation systems, like GPS, there is a need to study their vulnerabilities and try to overcome them to make these systems robust. Since the signals from satellite-based communication and

navigation systems transit the ionized part of the Earth's upper atmosphere (ionosphere) for propagation, these systems are vulnerable to the structures and variabilities of the ionosphere. The ionosphere affects any radio signal passing through it by introducing a phase advance and a group delay in the signal because of the dispersive nature of the medium. This effect in GPS, at least to first order, is usually removed by combining two GPS signals that are transmitted from the same satellite but with different frequencies [40].

Occasionally, due to small-scale electron density variations in the ionosphere, the radio signal can experience amplitude and phase fluctuations called scintillation [24]. These fluctuations can lead to degradation in a satellite's performance and/or there can be loss of accuracy if the radio signal is from a navigation system. In the case of extreme scintillation, receivers on Earth can also lose lock of the satellite signal. The most important factor is that because of the random and uncorrelated nature of scintillation, it cannot be corrected like the phase advance/group delay. It should also be noted that there is a productive part of scintillation too. Scintillation signals can be analyzed to obtain information about the ionospheric irregularities that are producing these effects. So the best possible way to mitigate them is to have an indepth understanding of the phenomena.

This can be achieved by a combination of methods, One such method is to create and test accurate scintillation indices to represent the statistical prop-

erty of the time varying signal for use in model/mitigating techniques. The other method is to understand the generation of the scintillation producing plasma structures using climatology of occurrence of scintillation and spectral properties of scintillation. In order to comprehend scintillation one has to study the ionosphere and the physical phenomena that take place in it. Due to the interactions among the solar wind, the interplanetary magnetic field and the Earth's magnetic field, the Sun's activity is directly mapped on to the high latitude regions of the Earth's ionosphere. Hence solar activity has a direct impact on the Earth's ionosphere especially at these high latitudes. It should be also noted that the Sun's magnetic activity goes through a periodic variation of maxima and minima approximately every 11 years. This modulates a long term temporal variation on how the Earth's ionosphere behaves, which in turn affects scintillation occurrence. Along with this long term variation, seasonal variation in scintillation occurrence has also been observed. [75, 30, 63, 51, 64]

The first scintillation studies [27, 62] were mainly conducted using natural radio sources. With the birth of artificial radio satellites, scintillation studies were conducted mainly by using VHF and UHF communication systems at mid and low latitudes. Systems like Wide-band satellite system, have made it possible to study the irregularity structures present in the ionosphere and also understand different phenomena which may be producing scintillations. These studies [33, 56] were among the first to indicate that the ionospheric

irregularities, which create scintillation, obey a power-law structure and that it is not a single size of irregularity but various sizes of irregularities that create scintillation. Seasonal variation of scintillation occurrence was also analyzed [8]. With the advent of GPS, scintillation studies got an additional boost given the spatial and temporal coverage of GPS. Scintillation indices like S_4 and σ_ϕ and cutoff frequency of 0.1 Hz for detrending filters, which were previously used in, e.g., Wide-band satellite system, became the default GPS scintillation indices [21, 17]. This replication of indices and detrending filter settings did not cause any problems as long as the studies were at mid- and low-latitudes, the area for which these indices and methods were developed [17].

An area which has been long uncharted territory as far GPS scintillation is concerned is the high latitude region. The high latitude ionosphere is usually more active than mid and low latitude regions. Studying these regions would not only give us information about the phenomenon happening in the ionosphere but also about space weather due to the direct connection between high latitude ionosphere and the interplanetary magnetic field through the Earth's "open" magnetic field lines [30]. Even though important reasons like these exist, GPS based ionospheric studies at these latitudes have not been performed as throughly as they have been in mid- and low-latitudes. The reason for this is the lack of GPS scintillation receivers and other necessary infrastructure at high latitude regions. This has changed greatly with the

arrival of GPS networks like the Canadian High Arctic Ionospheric Network (CHAIN) and the focus has shifted to GPS scintillation studies at high latitudes [31].

Recent studies [19, 17] involving high latitude GPS scintillation data have shown that if the default setting of 0.1 Hz cutoff frequency is used in the detrending filter, there is a possibility of an artifacts called "phase scintillation without amplitude scintillation", occurring in the data. This suggested the need for a better detrending method for high latitude GPS scintillation data. Also σ_ϕ, the default phase scintillation index, is shown to be prone to errors mainly because of the domination of low frequency components in the phase signal. Hence there is a need for a better detrending filter as well as a better phase scintillation index suitable for high latitude GPS signal scintillation. In order to address these issues, a new wavelet-based detrending filter in place of the default 6th order Butterworth filter and also a new phase scintillation index, σ_{CHAIN}, in place of the default phase scintillation index, σ_ϕ, are introduced in this dissertation. It is shown that using this new detrending filter and the new phase scintillation index, artifacts like the "phase scintillation without amplitude scintillation" are significantly decreased.

The wavelet detrended scintillation indices, S_4 and σ_{CHAIN}, are then calculated for the years March 2009-March 2011 to create GPS scintillation morphology for high latitudes. By looking into the morphology of scintil-

lations, one can try to understand the different phenomena causing both temporal and spatial variations of scintillations. As mentioned before, scintillations cannot be corrected and thus studying the morphology of scintillations is important as it can be used to create models which help to forecast scintillations. Analyzing the spectral slopes of scintillation signals can help to understand the physical mechanism(s) that are creating the ionospheric irregularities. It is shown that a power-law structure is observed in the scintillation spectra, which indicates that not one but a range of irregularity sizes contribute to scintillation. Estimation of the characteristic size of irregularities causing scintillation is also studied.

1.2 Thesis Outline

Chapter 2 starts with the introduction of the solar wind, its interactions with the Earth's magnetic field, and its impact on the Earth's ionosphere. Different layers of the ionosphere and their characteristics are also introduced. As the high latitude ionosphere is the area of interest in this dissertation, the main differences between high and low latitude ionosphere is briefly discussed. Also different regions, Auroral and Polar regions, of the high latitude ionosphere are discussed with respect to the alignment of magnetic field lines at these regions. Important phenomena like the Polar patches and cusp precipitation are also discussed. Two instruments, the ionosonde and GPS, are

used in this dissertation. Information about the ionosphere can be obtained by studying the affect ionosphere has on the electro-magnetic signal transmitted by these instruments. Hence, magneto-ionic theory, which forms the backbone of ionospheric probing using electromagnetic signals, is introduced. At the end of this Chapter, the ionosonde and its working principles are presented with some examples of the products that are derived from ionosonde data.

Chapter 3 provides a brief introduction to GPS, the main technique used in this thesis to study the ionosphere. GPS history, signal structure, and positioning techniques are discussed. Total electron content (TEC), the measure of electron content in the ionosphere along the GPS signal is defined, and the methods to calculate different versions, like slant TEC, vertical TEC, and phase-levelled TEC, are introduced. The concept of shell height and its importance are explained. A new method of combining the ionosonde derived shell heights with GPS TEC calculations is introduced. Also two different topside models, Chapman and Exponential, are used to obtain ionosonde derived TEC which are then compared to GPS derived TEC in order to check the compatibility of these top-side models at high latitudes. The problem of bias calculations at high latitudes as well as problems such as multipath and scintillation which are encountered during GPS data analysis are also discussed.

Chapter 4 introduces scintillation in radio signals at different frequencies and its importance in GPS signals. The wave equations in the ionosphere irregularities are derived from Maxwell's equations and how these equations can be used to form different scintillation models using different approximations are discussed. Given the stochastic nature of scintillation, it is shown how scintillation models can be used to understand the ionospheric irregularities using radio signals received at the ground. Phase screen theory which is considered to be a well established theory to understand weak scintillation is introduced. Scintillation in GPS signal, the default GPS scintillation indices, the problems involved with these indices (phase scintillation without amplitude scintillation), and the implications in using these problematic indices in scintillation models are discussed. A new detrending filter using wavelets is recommended.

Chapter 5 deals with the concept of wavelets. It starts with Fourier transforms and their advantages and disadvantages with respect to analyzing non-stationary signals like GPS scintillation signals. Wavelets being more localized and able to provide information in both time and frequency are introduced as better tools to analyze GPS scintillation signals. The main wavelet concepts like scaling, shifting, "Mother" wavelet, different "Mother" wavelets present in the community and the choice of using "Morlet" wavelet as the "Mother" wavelet in this study are discussed. A new method of filtering GPS scintillation signals using wavelets is introduced.

Chapter 6 describes the data analysis undertaken. There is an introduction to the Canadian High Arctic Ionospheric Network (CHAIN) from which the data has been obtained and the GPS receivers (NovAtel GSV 4004B) that are used in this network. The problems with the default phase scintillation index (σ_ϕ) and the Butterworth detrending filter used in these receivers are discussed. The need for a better detrending filter and a new phase scintillation index is revealed. The performance of the new wavelet filter introduced in Chapter 5 is compared with the default Butterworth filter as well as a new phase scintillation index (σ_{CHAIN}). The performance of σ_{CHAIN} is also analyzed. It is shown that σ_{CHAIN} along with the wavelet detrending filter seem to remove problems like the phase scintillation without amplitude scintillation.

Chapter 7 introduces the climatology of scintillation and its importance in creating scintillation models used to predict and mitigate scintillation. Scintillation climatology at different frequencies are discussed before introducing the GPS scintillation climatology. In this study GPS scintillation climatology was created using S_4 and the new phase scintillation index σ_{CHAIN}. CHAIN data for the years March 2009 to March 2011 were used to create these climatologies. The GPS climatology results are analyzed and compared with previous results. Possible physical phenomena responsible for the observed spatial and temporal variations in the scintillation occurrence are also dis-

cussed. Climatology of TEC gradients developed using GPS TEC data is also analyzed with respect to scintillation climatology.

Chapter 8 reveals the characteristics of the GPS scintillation signals. It explains the importance of GPS scintillation signal's spectral index. Spectral slopes of both amplitude and phase scintillation for over 1000 scintillation events are calculated and their distributions are analyzed. Elevation-angle dependence of the spectral slope is also discussed. Fading rate of the scintillation events is calculated and is used to calculate the characteristic size of the irregularities. The distribution of these characteristic sizes is also analyzed and discussed.

Chapter 9 summarizes the main contributions of this work and provide suggestions for future work that can be done using the results obtained from this work. The most interesting among them are the use of newly introduced scintillation indices in scintillation models created specifically for high latitudes, predicting ionospheric drift by calculating the Fresnel frequencies, and creating a real-time wavelet filter that can be used in GPS receivers.

Chapter 2

Ionosphere

2.1 Introduction

The Sun emits a stream of particles into the solar system called the solar wind. The solar wind also has a magnetic field associated with it, which moves along with it or more commonly referred to as the magnetic field being frozen into the solar wind. This magnetic field is called the interplanetary magnetic field (IMF). When looking down from the Sun's rotation axis, the magnetic field rotates with the Sun in a changing spiral formation. When observed from the Earth, the IMF is incident at an angle of 43^0 to the Earth-Sun line due to this spiral formation. In three-dimensional space, the IMF of opposite polarity is separated by a current sheet that co-rotates with the Sun. As shown in Figure 2.1, this current sheet has a wavy structure which exposes the Earth to IMF which is both directed towards and away from the

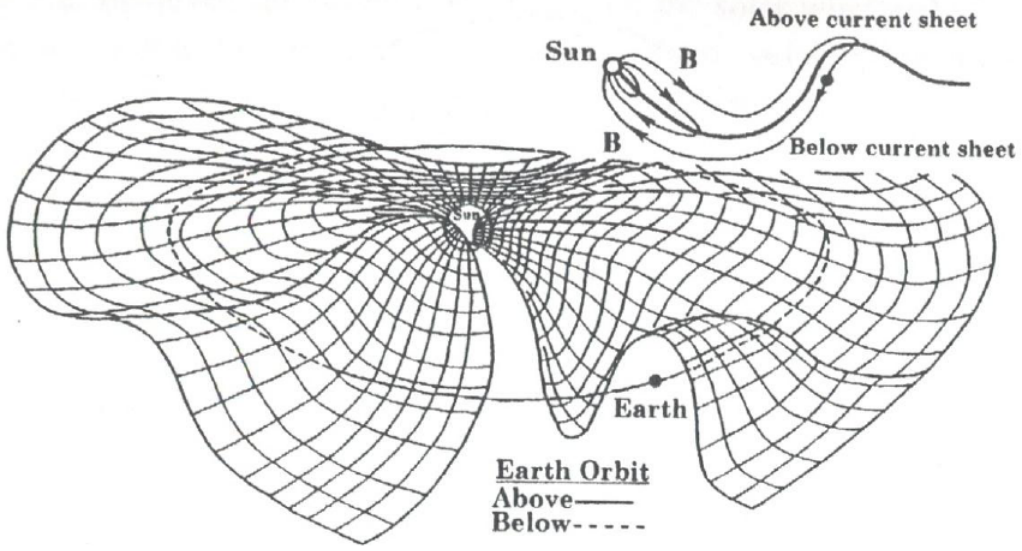

Figure 2.1: Diagram of the heliospheric current sheet (grid) that separates the IMF directed away from (above the sheet) and towards (below the sheet) the Sun. The Earth deviates above and below the sheet as it orbits the Sun as seen in the Earth-centric view. [30]

.

sun as seen in the Earth-centric view [35, 30].

Earth being part of the solar system, gets affected by this wind. The speed of the solar wind can go up to 1000 km/sec from its average speed of 200-700 km/sec in hours or sometimes in minutes depending on the solar activity level. Along with these short-term variations, the level of the sun's magnetic activity also follows a approximately 11-year cycle where a reversal in magnetic polarity occurs [30]. The Sun's activity fluctuates during these 11 years. The time period when the magnetic activity is high is called the "solar maximum", while the time period when the magnetic activity is less is called

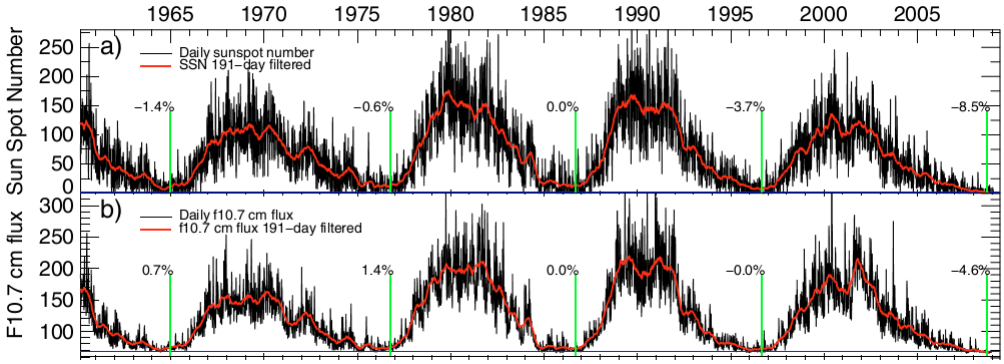

Figure 2.2: Daily values of the time series of (a) Sun spot number and (b) F10.7 for the period 1960-2009. [22]

"solar minimum". Most commonly used indices to represent solar activity are the Sun Spot Number (SSN) and the Solar Radio Flux at 10.7 cm wavelength (F10.7). Figure 2.2 shows a plot of both SSN and F10.7 flux for the years 1960-2009.

From Figure 2.2, the 11-year cycle in the sun's activity can be observed clearly and it should be noted here that the data used in this thesis (March, 2009-March, 2011) is from the period of solar minimum. The Earth also has its own magnetic field that is believed to be produced by the rotating core inside the Earth. This magnetic field is very important as it shields the Earth from the highly energetic particles that are present in the solar wind. Close to the Earth, the geo-magnetic field can be approximated by a dipole-like topology. The magnetic dipole axis is tilted by about 11^0 with respect to the Earth's rotation axis. The Earth's magnetic south pole is near its geographical north pole and vice-versa for the magnetic north pole. Thus the magnetic

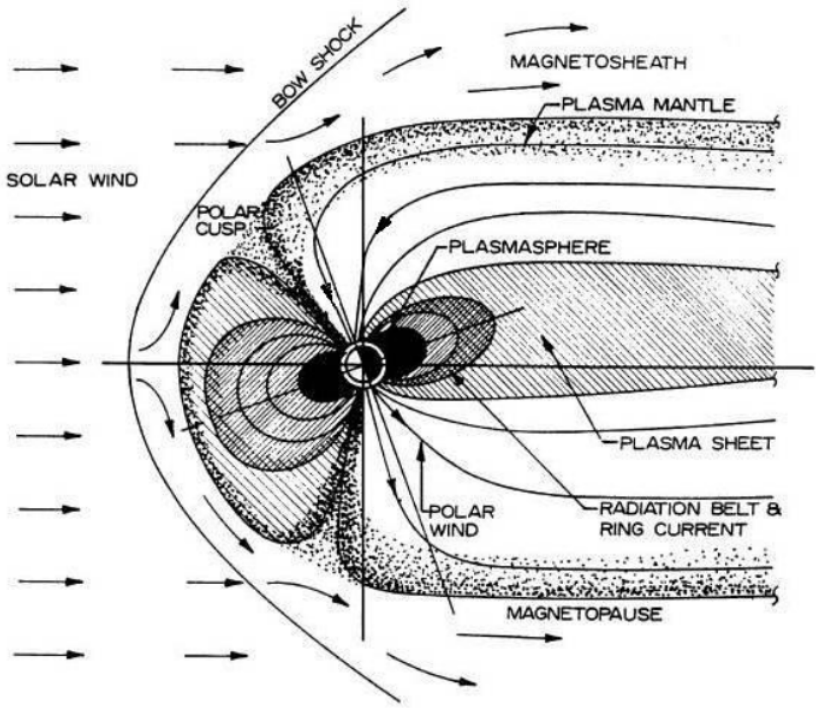

Figure 2.3: Diagram showing the basic structure of the magnetosphere for an observer situated at dusk in Sun-Earth plane in Summer of Northern Hemisphere. [30]

field lines are directed away from the Earth in the southern hemisphere and toward the Earth the northern hemisphere. As we move further away from the Earth, the solar wind pressure compresses the dayside geomagnetic field, while the night time geomagnetic field is dragged anti-sunward resulting in an elongated tail-like topology. This topology, which depends on the Earth's magnetic field, inter-planetary magnetic field, and the solar wind is called the magnetosphere [30].

As shown in the Figure 2.3, the magnetosphere is a complex system and is a subject on its own. In this dissertation, pertinent topics will only be discussed. The main interest in this dissertation is the high latitude ionosphere, the sphere of plasma around the Earth which is affected by the solar wind, magnetosphere, and their interactions.

2.2 Ionosphere

The ionosphere is a sphere of ionized plasma around the Earth's surface at a height of around 70 km to about 1000 km with the exact boundaries not well defined [35, 30]. Above ≈1000 km electron density thins out into the plasmasphere and subsequently to interplanetary plasma. The ionosphere plays an important role in the atmospheric electricity and forms the inner edge of the magnetosphere. The main source of ionization is the solar irradiation where the neutral atoms and molecules are ionized by the solar X-rays and extreme ultraviolet radiation to produce free electrons.

As seen from Figure 2.4, the major neutral constituents that photo-dissociate to form the ionosphere are molecular oxygen (O_2), diatomic nitrogen (N_2) and atomic oxygen (O). Ionization of these neutral species depends on such variables as altitude, local time, season, and solar activity. At high latitudes, high energy ions and electrons precipitating through open field lines can also be an important source for ionization. These ionized particles again recom-

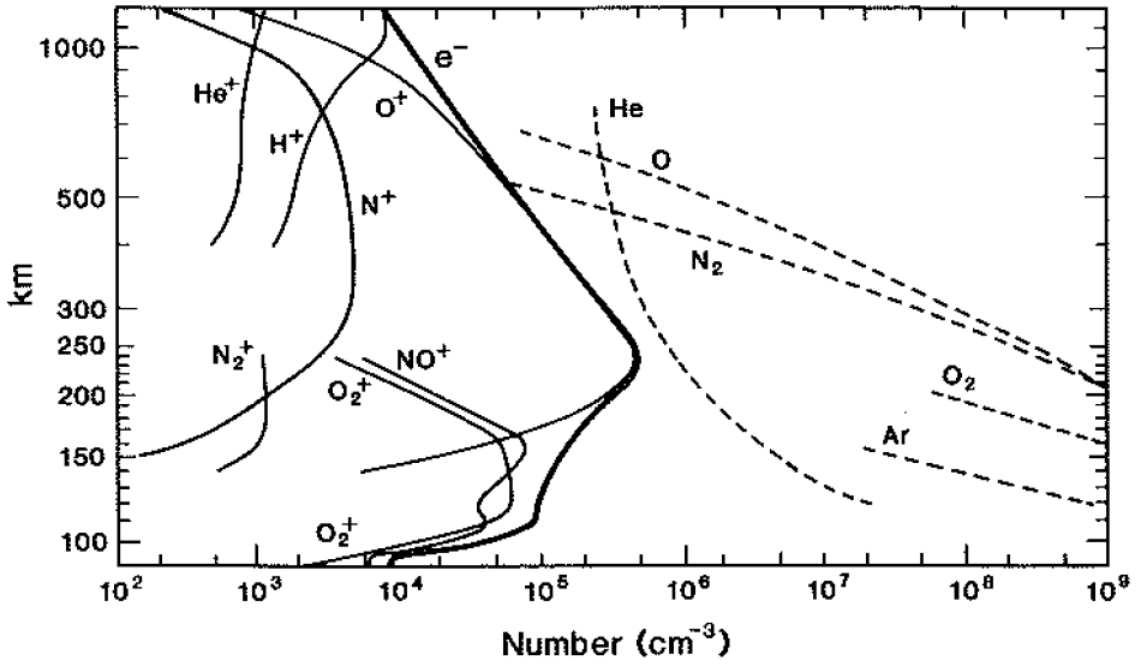

Figure 2.4: Number density of charged and neutral constituents of the ionosphere. Altitude in the ionosphere is indicated on the vertical axis. [30]

bine to form neutral atoms or molecules. The structure of the ionosphere at any instant of time or space depends on the balance between the production, recombination, and transport processes of these ionized particles. As the major neutral particles have different molecular weights, they are horizontally stratified and thus the ionosphere is also stratified horizontally. As shown in Figure 2.5, for a mid-latitude region, depending on the neutral constituents and the range of energies that ionize these neutral constituents, the ionosphere is divided into four main layers; namely, D, E, F1 and F2.

2.2.1 D Layer

The D Layer is the bottom-most layer of the ionosphere and is defined as the layer in the ionosphere that is at a height of 70 km to 90 km. This layer is mainly formed from ionization of nitric oxide (NO) molecules due to Lyman α radiation which is at a wavelength of 121.5 nm. This radiation is one of the two radiation bands which penetrate down to the altitudes of the D Layer. Another radiation band which ionizes the neutrals like N_2 and O_2 in the D layer is the hard X-rays. These rays have a wavelength of about 0.1-1 nm and are usually found when there is moderately high solar activity. NO^+ and O^+ are the main positive ions present in the D layer. During the day solar radiation can also extract electrons from negative ions like O_2^-:

$$O_2^- + h\nu \rightarrow O_2 + e$$

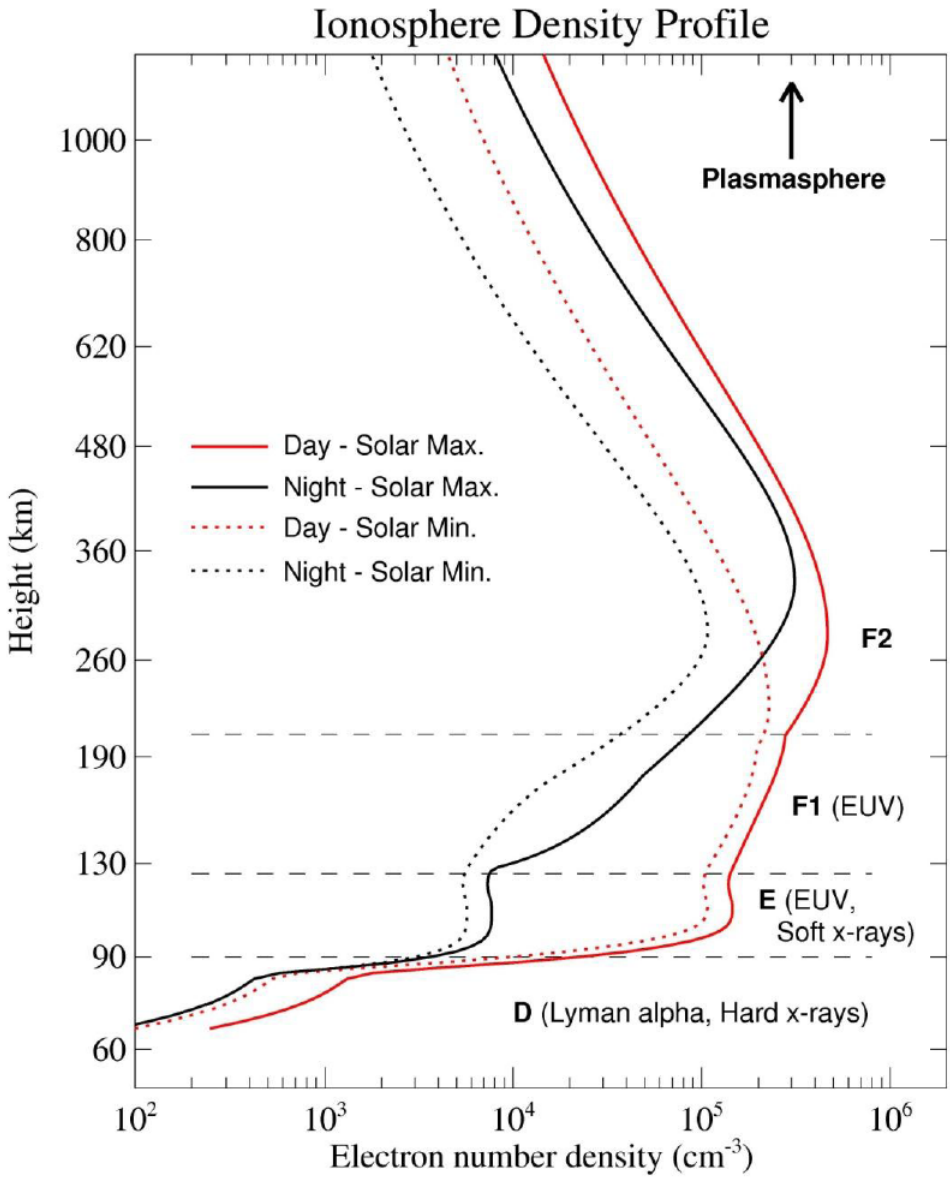

Figure 2.5: Density profiles of ionospheric electrons under various conditions for a mid latitude region ionosphere. Electron densities are from IRI-2007. Heights of ionospheric layers and the main radiation type contributing to ionization are also indicated. [70]

This reaction shows why there is more electron density when the solar radiation is present and less electron density at night as shown in Figure 2.5. Since this reaction depends on solar radiation, it is highly dependent on the solar zenith angle, latitude, and season. Recombination or loss of ionization occurs mainly due to the attachment of electrons with the neutral species, mainly diatomic oxygen. Owing to their weight, there tends to be a presence of heavier ions in the D layer. These heavier ions generally have higher recombination rates which results in lower electron densities. The D Layer is also important in radio communications as this layer is mainly responsible for absorption of high frequency (HF) radio waves. Also at high latitudes, during solar events, there can be large precipitation of high energy particles into the D layer which causes high ionization and thus significantly increases the absorption of radio waves which can sometimes cause total radio "black out". These events of high absorption are called Polar Cap Absorption (PCA) events [35, 30].

2.2.2 E Layer

The middle layer in the ionosphere that stretches from a height of 90 km-150 km is called the E layer. It usually has a peak around 100 km-120 km. The main source of ionization at this layer is extreme ultra violet (EUV) radiation that has penetrated the F layer without being absorbed and has enough energy to ionize O_2 and from soft x-rays which have a wavelength of 1-10 nm and that can ionize neutral species. The most dominant ions formed in this

layer are O_2^+, N_2^+ and NO^+ and dissociative recombination of these ions are the main cause of electron loss in this region [35, 30].

The balance between the ion-production and recombination determines the electron densities present in this layer. Electron densities diminish significantly at night as there is no sunlight and hence no primary source of ionization. The positive ions present in this layer are mostly molecular. Some times there is an anomalous enhancement of electron density in the E layer called Sporadic E.

2.2.3 F Layer

The F layer in the ionosphere ranges from around 150 km until the bottom of the plasmasphere. Most of the ionospheric plasma is in this layer. Sometimes, depending on the time of day, the thickness of the layer, and the location, there are two distinct layers in this region, F1 and F2. The F1 layer extends from 150 km to 200 km altitude and is most pronounced during the day, summer, and at solar minimum. The interesting thing about the F1 layer is that it seldom exists as a distinct peak and for this reason it is some times called the F1 ledge. Usually at nights, due to a lack of solar radiation, F1 merges into F2. This also happens during solar maximum where there are high electron densities present in the F layer.

The F2 region is the region from the F1 layer into the plasmasphere. As

shown in Figure 2.5, a majority of F2's structure remains intact even at night unlike other lower layers. This is mainly due to the decreasing atmospheric pressure with altitude which results in a bulk movement (diffusion) of ionospheric plasma in the vertical direction. The peak density of this layer is at a height of 200-400 km [35, 30].

At F2 region, despite a decreasing ionization rate, electron density increases. This is due to the increasing O to N_2 density ratio, where density of N_2 governs the loss rate, while density of O governs the production rate of the electrons. The electron loss in the F2 region occurs in two stages:

$$O^+ + N_2 \rightarrow NO^+ + N$$

$$NO^+ + e \rightarrow N + O$$

This transfer reaction becomes the factor which controls the loss rate in the F2 region. Since N_2 density decreases at a higher rate than that of O density, the decrease in electron loss rate will be faster than the decrease in electron production rate.

2.2.4 Plasmasphere

The plasmasphere is the region above 1000 km in altitude where the Earth's ionosphere extends into the inner-most layer of the magnetosphere. At low

and mid-latitudes, the plasmasphere has an important influence on the top side layer of the ionosphere due to the ion-exchange that takes place between the F layer and the plasmasphere. The dominant ion present in the plasmasphere is H^+. The influence of the plasmasphere on radio signals is not prominent and mostly absent as we go higher in latitude [30]. This can be understood by observing the shape of the plasmasphere in Figure 2.3, where one can observe that at high latitudes there is less or no plasmasphere. This is one of the many differences between the ionosphere at low and high latitudes. As this dissertation deals with the high-latitude ionosphere, it is imperative that some important characteristics of the high latitude ionosphere are discussed.

2.3 High Latitude Ionosphere

The high latitude ionosphere is different both in structure and dynamics. As shown in Figure 2.3, the magnetic field lines at these latitudes are connected to the outer part of the magnetosphere, which is mainly driven by the solar wind, unlike the magnetic field lines from low latitudes that are connected to the inner magnetosphere. The magnetic field lines at very high latitudes ($\approx 70^0$N/S) are also called "open" field lines as they have one end on the Earth's surface and the other in the inter-planetary field which make this region vulnerable to space weather. The inner magnetosphere is mainly influenced by the geomagnetic field and only controlled to a certain extent by the solar wind [30]. The coupling between the ionosphere, magnetosphere,

and solar wind made possible by the open field lines is one of the main driving forces for all the mechanisms in the ionosphere. This coupling is more pronounced when the solar activity rises and signatures of these solar storms are seen in the Earth's ionosphere in many manifestations. Along with solar wind, other mechanisms which affect the ionosphere are thermal tides, coupling from troposphere/stratosphere and winds. Thus studying the high latitude ionosphere would not only provides information regarding the mechanisms present in the ionosphere but also information regarding space weather. In this dissertation, the area of interest is the northern high latitude region especially the Canadian north. As shown in Figure 2.6, the high latitude ionosphere can be divided into two distinct regions namely, the Auroral Region (regions where aurora is visible) and Polar Region (region enclosed by the auroral region) [30].

2.3.1 Auroral Region

The auroral region, or more commonly called the auroral oval, is the region usually defined as being between the closed magnetic field lines and the "open" magnetic field lines. This region is one of the prominent regions on Earth where phenomena like Aurora Borealis/Australis, geomagnetic field disturbances are observed. These phenomena are mainly due to the influx of energetic particles from closed magnetic field lines. The auroral oval gets its name from its oval shape that encloses the polar region. It is observed that the size of the auroral oval changes with magnetic activity. High geomagnetic

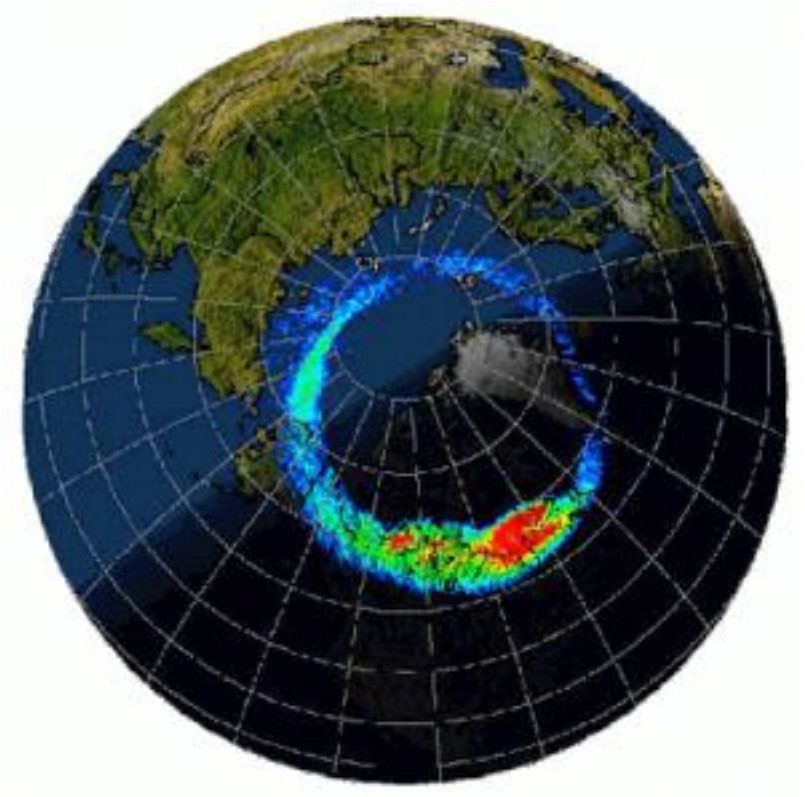

Figure 2.6: This ultraviolet image shows an auroral display as seen from space, overlaid on top of a visible image of Earth. The false-color reds indicate the brightest aurora and blue the dimmest. The brightest aurora is typically found at midnight. Courtesy: National Space Science Data Center, NASA.

activity increases both the equatorial and the polar edges of the auroral oval boundary. Figure 2.7 shows the location of the auroral oval for moderate and active geomagnetic levels as estimated from all-sky camera images.

2.3.2 Polar Region

The region enclosed by the auroral oval and that has the foot prints of the "open" field lines is called the polar region. When the magnetosphere (plasma) goes through a magnetic field (IMF), this interaction between plasma and magnetic field can be considered in terms of a dynamo action. This results in an electric field perpendicular to both the plasma and the magnetic field. As the magnetic field lines are equi-potential, the electric field due to this dynamo action is mapped to these polar regions via the open field lines. The direction of this electric field is in the direction of dawn to dusk. Now this electric field is near perpendicular to the magnetic field lines which in turn causes an $\mathbf{E}\times\mathbf{B}$ drift (a drift in the direction perpendicular to the $\mathbf{E}$ and $\mathbf{B}$ field vectors) of the charged particles as shown in Figure 2.8. This $\mathbf{E}\times\mathbf{B}$ drift is a very important phenomenon in the polar cap dynamics as this is the major means of plasma transport in these regions. Typical values for this drift are 200 m/s-300 m/s for magnetically quiet days but can go up to 1000 m/s-1500 m/s on magnetically active days [35]. Other important phenomena that occur in the polar regions are the polar cusp precipitation, polar patches and polar tongue of ionization. Out of these, two important processes with respect to this thesis are the polar cusp and polar patches [30].

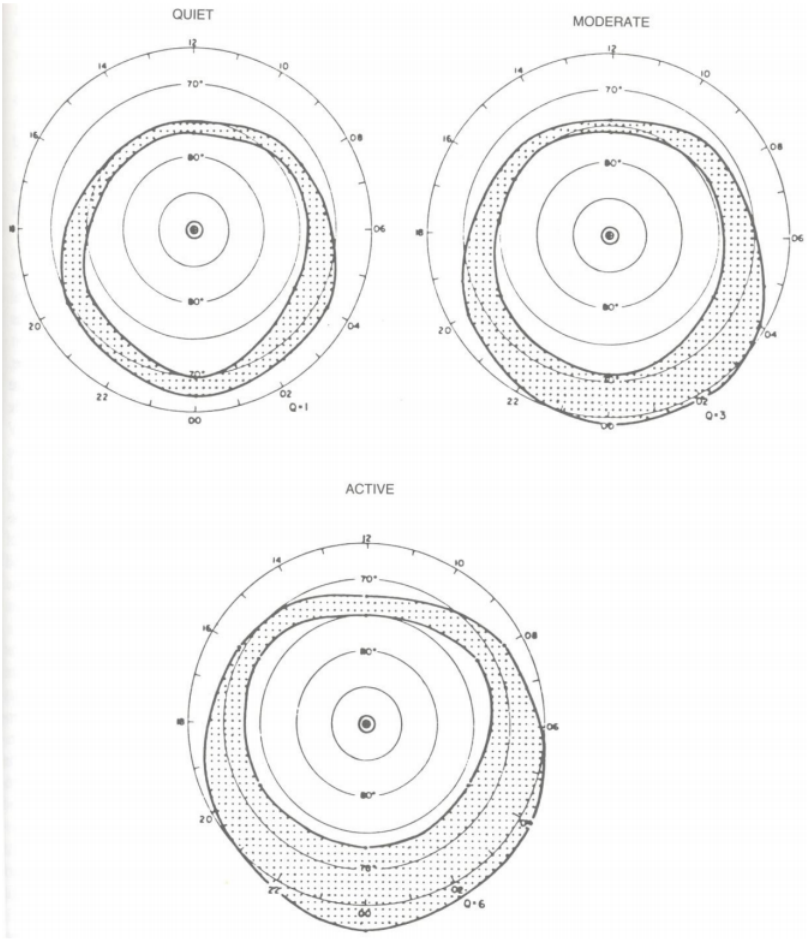

Figure 2.7: Statistical location of auroral activity during periods of quiet, moderate and active geomagnetic activity. Data is from all-sky camera images. [38]

Polar Cusp

Initial studies of the cusp region were done using satellites [26, 30], which have indicated that around 73^o-83^o magnetic latitude and over 8 hr of local time around the local noon, there is a flux of low energy electrons on the day side. One such example is shown in Fig 2.9 which shows the electron and proton flux data as observed by a soft particle spectrometer (range=10 ev to 10 kev) on the ISIS satellite for a particular orbit on 3 February 1969. It can be seen that the low energy flux values increased considerably at 73^o magnetic latitude. It has been seen that these low energy particles have the characteristics of particles in the magnetosheath which led to the conclusion that these electrons may have entered the Earth's ionosphere from the magnetosheath via the "open" magnetic field lines that have their foot prints at these latitudes.

Even though there is an intense debate on how the electrons enter the ionosphere via these "open" magnetic field lines, two main mechanisms are usually credited [26]. One is that the magnetic field lines merging, where a southward pointing IMF would merge with the Earth's magnetic field line. This would then cause the electrons to have a free passage into the Earth's ionosphere. The other mechanism is through the cross field diffusion of electrons. The latter can work when IMF is southward and when it is northward

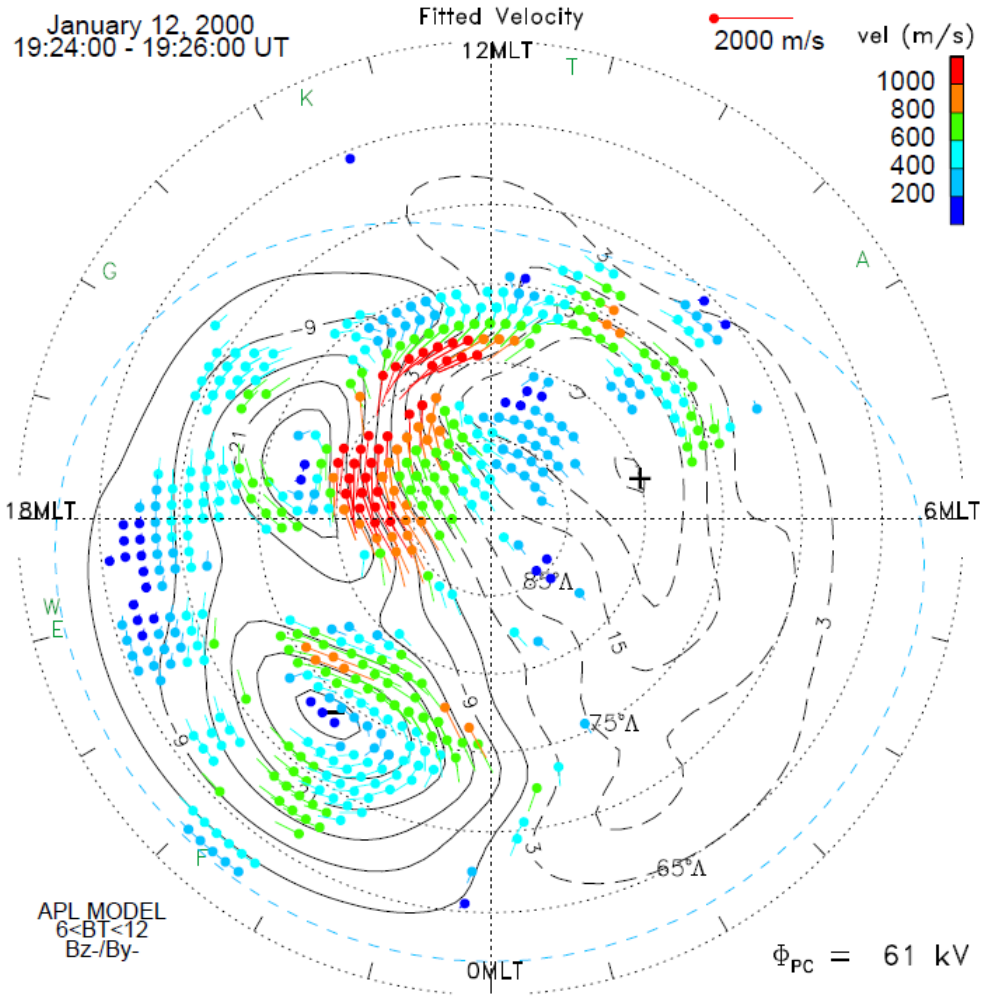

Figure 2.8: Fitted velocity vectors and electrostatic potential contours from the LOS measurements obtained from SuperDARN at high latitudes in Northern Hemisphere. Since the electric field, **E**, is in the dawn-dusk direction and magnetic field, **B**, is pointing into the earth, the **E**×**B** drift is in the anti-sunward direction as shown here. [60]

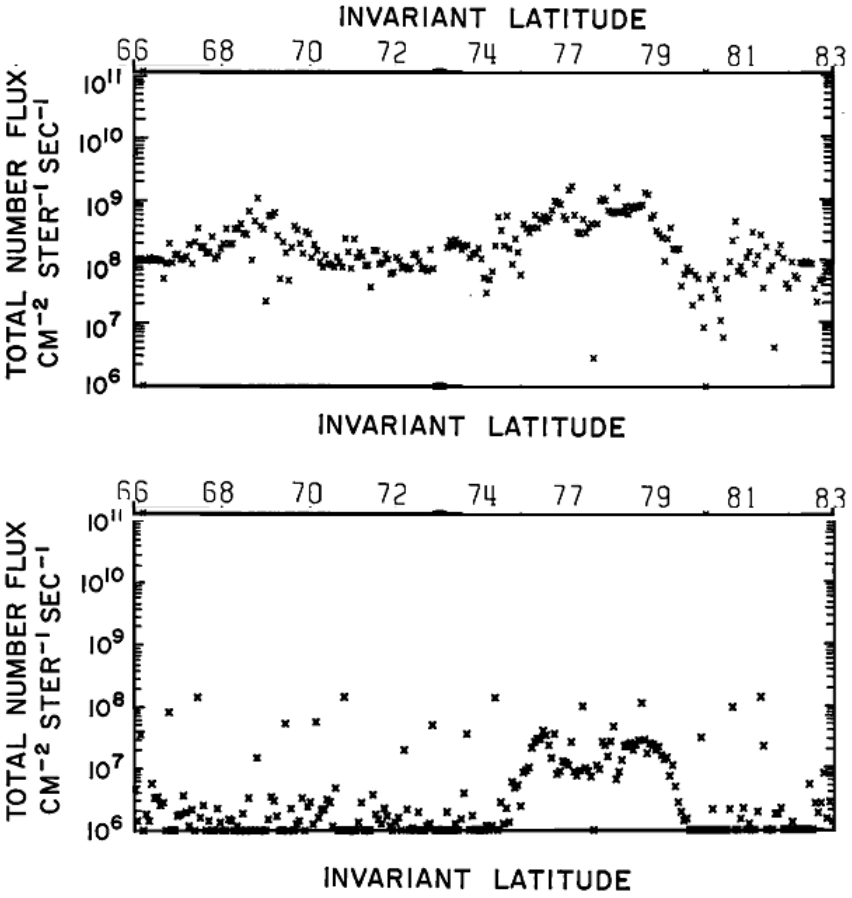

Figure 2.9: Total number flux of electron (top panel) and proton (bottom panel) as observed by soft particle spectrometer on ISIS satellite on its orbit 49 on 3 February 1969. [26]

as well. These precipitated electrons form electron density enhancements, which can effect radio-communication systems. These enhancements can vary in size from a few hundred meters to a few hundred kilometres. Electron density enhancements that are more than a few kilometres in size are called polar patches. It should be noted that particle precipitation is one of the mechanisms that causes patches but not the only one. Other mechanisms like the Tongue of ionization (TOI), which is an enhanced electron density drawn out from the sunlit side over the pole towards the night side. [30, 35]

Polar Patches

Polar patches are regions of enhanced density in the ionosphere where the electron density is usually 2-10 times the background electron density. The patches have a size of tens of kilometres to few hundred kilometres in size. They are usually circular in form and are smaller than the gap between them, which indicates that they are enhancements of ionization above a low background rather than depletions in a higher background density. These patches usually appear when there is a southward IMF and occur in all seasons but predominantly in winter. They tend to move with the general plasma drift. An increase in the TEC (total electron content) of the ionosphere, or an increase in the F2 layer density, or 630 nm emissions are generally used to identify polar patches. Several investigations [42] have been conducted to study the patch formation and convection. It is also observed that there are

gradients at the edges of the patches and these gradients are thought to be the primary cause for signal degradation of satellite navigation and communication systems, making polar patches an important phenomenon to study in the polar regions. [30]

2.4 Ionospheric Measurements

In this study, the ionosphere from high latitudes, especially the region in the Canadian north, is of main interest and the two main instruments that were used to study this region are ionosondes and the GPS satellites. Both of these instrument types study the effect of the ionosphere on the radio signals emitted by them and through this information is obtained on the ionosphere. Thus, a good starting point is to know how the ionosphere affects any radio signal that transverses it.

2.4.1 Radio Wave in the Ionosphere

The ionosphere is a refractive and dispersive medium. It is refractive because of the change in velocity of the electromagnetic wave as it passes through the ionosphere. Quantitatively this can be represented by the refractive index (n) of the medium, which is the ratio between the speed of the electromagnetic wave in a medium compared to the speed of the electromagnetic wave in vacuum. This refractive index of the wave in the ionosphere depends on

many factors like the magnetic field strength, electron density, frequency of the wave, etc. The ionosphere is also birefrengent medium where two characteristic modes of propagation can appear as the wave traverses through it. Sir Edward Appleton derived an empirical formula that describes the characteristics of a wave propagating through an ionized medium at an angle with the magnetic field. An illustration of such a wave front propagating in the x-direction at an angle θ with the magnetic field vector B is shown in the Figure 2.10.

The Appleton equation for refractive index for such a wave is [35]:

$$n^2 = 1 - \frac{X}{1 - iZ - \frac{Y_T^2}{2(1-X-iZ)} \pm \sqrt{\frac{Y_T^4}{4(1-X-iZ)^2} + Y_L^2}} \tag{2.1}$$

where n is the complex refractive index $(\mu - i\chi)$ with μ being the real part and χ being the imaginary part and : X=(ω_p^2/ω^2), $Y_T = (\omega_B/\omega)sin\theta$, $Y_L = (\omega_B/\omega)cos\theta$, Z=$\nu/\omega$

ω = angular frequency of the propagating wave = 2πf, f is the frequency of the propagating wave

ω_p= plasma frequency of the ionosphere = $\sqrt{(\frac{Ne^2}{m_e\epsilon_0})}$

N = electron density of the ionosphere

f= frequency of the propogating wave

e= electron charge (1.602 * 10^{-19} C)

m_e = mass of the electron (9.109 * 10^{-31} Kg)

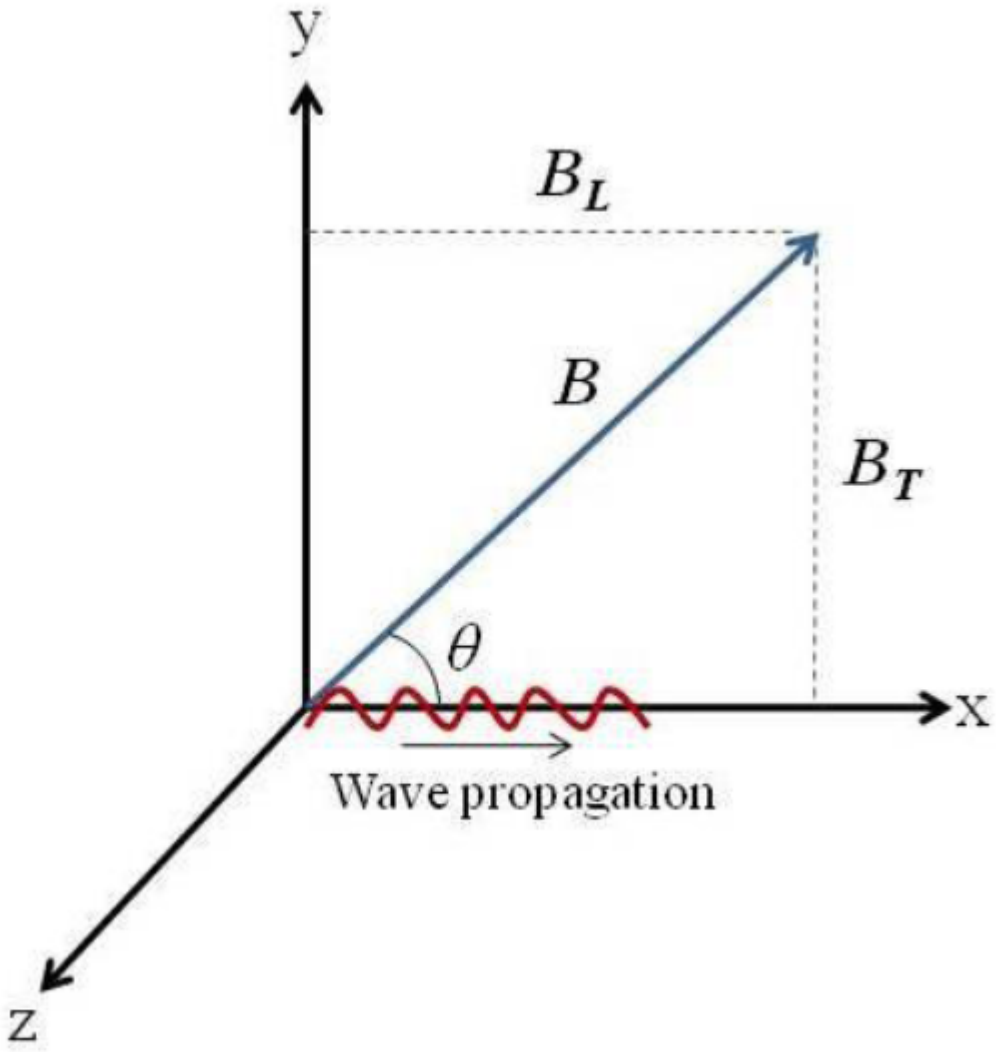

Figure 2.10: Orthogonal coordinate system for a plane wave propagating along the x axis at an angle θ to the geomagnetic field (B). The geomagnetic field is in the x-y plane. [70]

ϵ_0= permitivity of vaccum = 8.854 * 10^{-12} C^2 N^{-1} m^{-2}

ω_B= electron angular gyro-frequency = $\frac{eB}{m_e}$

B= geo magnetic field strength

ν= electron collision frequency in the ionosphere

θ= angle between the wave normal and the geomagnetic field

As seen in equation 2.1, the refractive index has a complex form since the ionosphere is both refractive (real) and dissipative (imaginary). This equation can be simplified depending on the characteristics of the instrument that is being used to probe the ionosphere. At frequencies that are of interest in this dissertation (1-2 GHz), the collision frequency of around 10^4 Hz in the E, F layer can be considered negligible. Using this approximation (Z=0) in equation (2.1), it can be re-written as [35, 40, 30]:

$$n^2 = 1 - \frac{2X(1-X)}{2(1-X) - Y_T^2 \pm [Y_T^4 + 4(1-X)^2 Y_L^2]^{\frac{1}{2}}} \tag{2.2}$$

This equation can then be expanded up to the 4th inverse power of frequency:

$$n \cong 1 - \frac{1}{2}X \pm \frac{1}{2}XY\,|cos\theta| - \frac{1}{8}X^2 - \frac{1}{4}XY^2(1 + cos^2\theta) \tag{2.3}$$

As the other terms are at least 2 to 3 orders of magnitude less than the second term, this equation can be further approximated to [35, 40, 30] :

$$n \cong 1 - \frac{1}{2}X \tag{2.4}$$

Now substituting for X:

$$n \cong 1 - \frac{40.3N}{f^2} \tag{2.5}$$

The ionosphere is also a dispersive medium as the velocity of propagation of a wave traveling in the ionosphere depends on its frequency [35, 40, 30]. For a modulated wave, two types of velocities can be defined namely "phase velocity" and "group velocity". The magnitude of Phase velocity (V_p) is defined as :

$$V_p = \frac{\omega}{k} \tag{2.6}$$

while the magnitude of group velocity (V_g) is defined as [35, 40] :

$$V_g = \frac{\partial\omega}{\partial k} \tag{2.7}$$

where k = $\frac{2\pi}{\lambda}$; λ= wavelength of the signal that is being transmitted.

The phase velocity and group velocity are related to their corresponding refractive indices, n_p and n_g respectively, as follows [35, 40] :

$$n_p = \frac{c}{V_p} \quad n_g = \frac{c}{V_g} \tag{2.8}$$

Using these equations it can be seen that that the relation between the group

refractive index and the phase refractive index using equations 2.7 and 2.8 :

$$n_g = n_p + f\frac{\partial n_p}{\partial f} \tag{2.9}$$

and now substituting equation (2.5) as the phase refractive index in equation 2.9 we have [35, 40, 30] :

$$n_g \cong 1 + \frac{40.3N}{f^2} \tag{2.10}$$

This shows that for a modulated signal passing through the ionosphere, there is a group delay and phase advance. These properties are very important and are used in many ionospheric measurement techniques like the one used in this dissertation.

2.5 The Ionosonde

The ionosonde is a special radar used to study the ionosphere. It transmits HF radio waves, sweeping from low to high frequency, and measures the time taken for these waves to come back to the receivers after being reflected by the ionosphere. This time can then be multiplied with the speed of light to get an estimate of the height of reflection. This height is called the "virtual" or group height. As noted in the Section 2.4, the group velocity of the wave depends on the refractive index, which in turn depends on the electron densities present in the ionosphere. Thus it cannot be assumed that the wave is traveling at the vacuum speed of light and hence the heights calculated are

virtual but not real heights.

An ionosonde works on the principle of total reflection of the wave at the ionosphere. To understand this better, one needs to look at equation (2.5) again. At the point of reflection the refractive index is equal to zero. Equation (2.5) can be re-written as :

$$f^2 = 40.3N \tag{2.11}$$

Thus a certain wave with a frequency "f_1" would be reflected from the ionosphere where the corresponding electron density is "N_1". Any frequency higher than this frequency (f_1) will penetrate that layer of density (N_1). Hence that particular frequency "f_1" is called the critical frequency for that layer with density "N_1". Since the ionosonde sweeps through a set of frequencies, one can obtain an electron density profile of the ionosphere. These profiles are usually plotted in an ionogram. A diagram depicting such an ionogram is shown in Figure 2.11.

From these ionograms one can clearly see the profile of the ionosphere as well as the critical frequency at different layers, of particular note is the critical frequency of the F2 layer, which is useful in ionospheric studies. As indicated, the heights are virtual heights and one needs to convert them into real heights for scientific purposes. The real height (h_r) is related to the

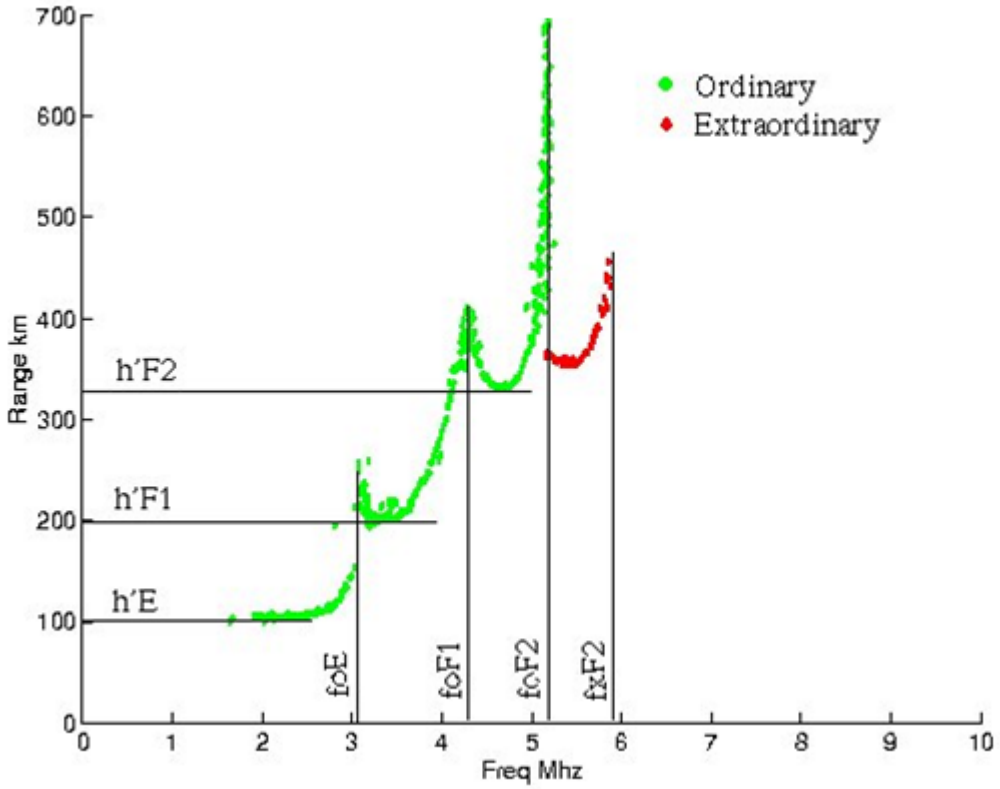

Figure 2.11: Diagram depicting an ionogram obtained using an ionsonde. X-axis represents frequency and Y-axis represents virtual height. Critical frequencies of ionospheric layers and corresponding heights are also seen. [12]

virtual height (h_v) in the following way [30, 35]:

$$h_v = \frac{1}{2}ct = c\int_0^{h_r} \frac{dh}{v_g} = \int_0^{h_r} n_g dh \tag{2.12}$$

where

c=speed of light

t=time taken to receive the reflected signal

v_g, n_g= group velocity and group refractive index respectively.

Solving for h_r is not trivial. In this dissertation, the Polynomial Analysis program (POLAN) [66] which calculates the real heights by using the virtual heights as one of the inputs is used. The process of converting virtual heights into real heights is called inversion. In this analysis manually selected virtual heights (manual inversion) were given as inputs to POLAN. POLAN also gives peak frequencies, shell height and other ionospheric parameters as outputs. It should be noted that the ionosonde can only give information up to the F layer as frequencies above the F2 peak frequency would not be reflected as there is not enough electron density to reflect those waves. Thus the ionosphere profile obtained using the ionosonde is called the "bottomside" profile. The whole profile of the ionosphere can be obtained by modeling the "top-side" ionosphere using the variables obtained from an ionosonde derived "bottomside" [35]. In this dissertation, two top-side models that can be used in modeling the high-latitude ionosphere were compared. These results will

be discussed in Chapter 3.

2.5.1 Canadian Advanced Digital Ionosonde

The Canadian Advanced Digital Ionosonde, more popularly known as CADI, was designed at the University of Western Ontario, Canada. It "is a state of the art, low cost, full featured ionosonde ideal for both routine ionospheric monitoring and scientific research" [12]. CADI consists of a transmitter antenna and four receiving antennas arranged in a square. Its frequency range is 1-20 MHz and it transmits a pulse of 600 W of power. Figure 2.12 shows a picture of a CADI transmitting antenna installed at Cambridge Bay [12].

As with any ionosonde, CADI also gives information about the electron density profiles in the ionosphere. Using CADI, these profiles can be obtained up to a height of 500 km with a 6 km resolution. An example of such a profile is shown in Figure 2.13 where the "black" line indicates the real height obtained using POLAN after manually scaling the ionogram.

CADI can also be used to calculate ionospheric drifts which can be very useful in ionospheric studies. To do this, a CADI assumes that the ionosphere is drifting at a constant rate above it. The main principle behind calculating the drift is the principle of interferometry. Here, CADI first finds the Fourier transform of every received signal/source to obtain its received frequency and thus measures its Doppler shift (d). Then by using the four receiving

Figure 2.12: Canadian Advanced Digital ionosonde (CADI) installed in Cambridge Bay, Canada.

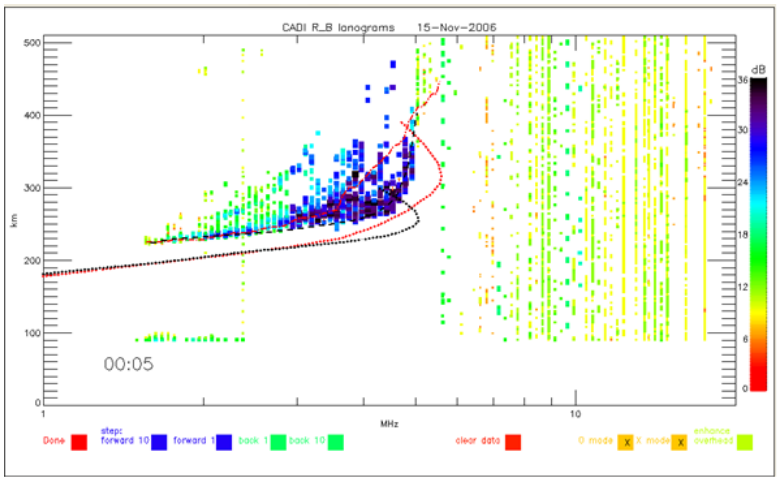

Figure 2.13: An example of an ionogram obtained from Resolute Bay, Canada on 15 November 2006 at 00:05 UTC. [12]

antennas and applying interferometry principles, the angle of arrival (zenith angle and azimuth angle) is calculated for those reflected points. Using these variables, normalized sky-plots are created. An example of such a skyplot is shown in Figure 2.14.

From the data from these skyplots, the direction and magnitude of the ionospheric drift can be obtained by least-squares fitting the data using the formula [52] :

$$\epsilon^2 = \sum_{i=1}^{l} [\frac{1}{2}\lambda d_i - (v_x cos\phi_i sin\theta_i + v_y sin\phi_i sin\theta_i + v_z cos\theta_i)]^2 \qquad (2.13)$$

where

v_x,v_y,v_z = x,y,z components of the drift velocity.

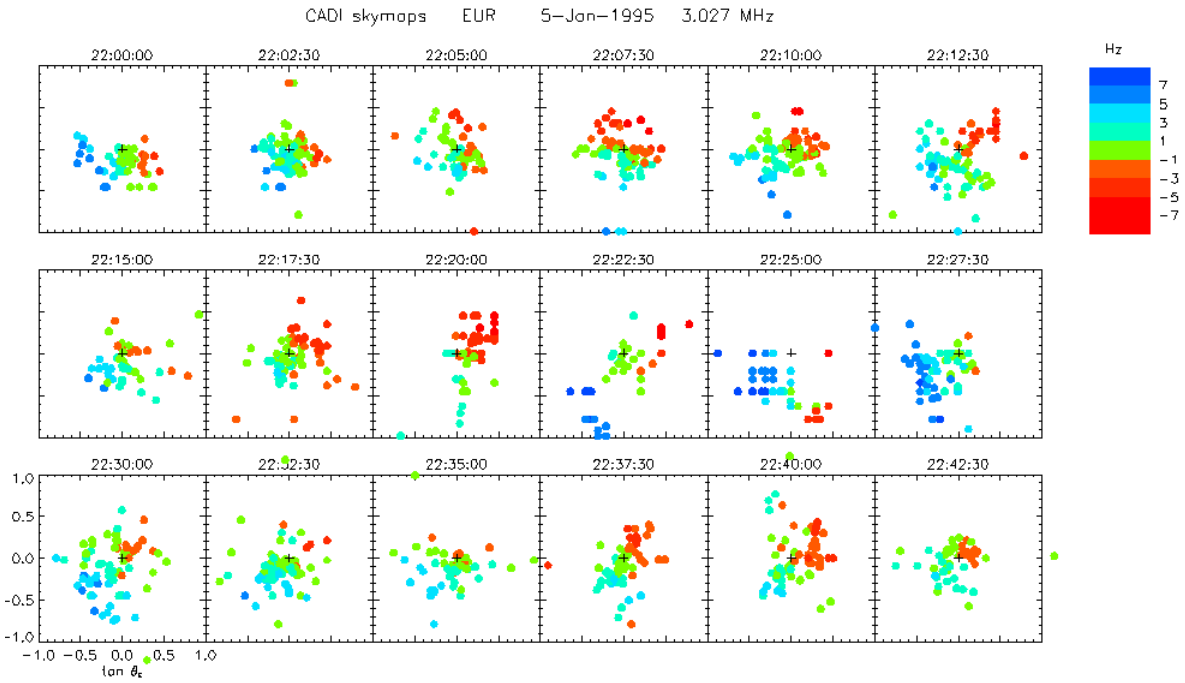

Figure 2.14: An example of a CADI skyplot obtained at Eureka, Canada on 5 January 1995. The over head point is marked with "+" and the angular position coordinate information is shown on the bottom left panel. The color coding represents the Doppler shift frequency. [12]

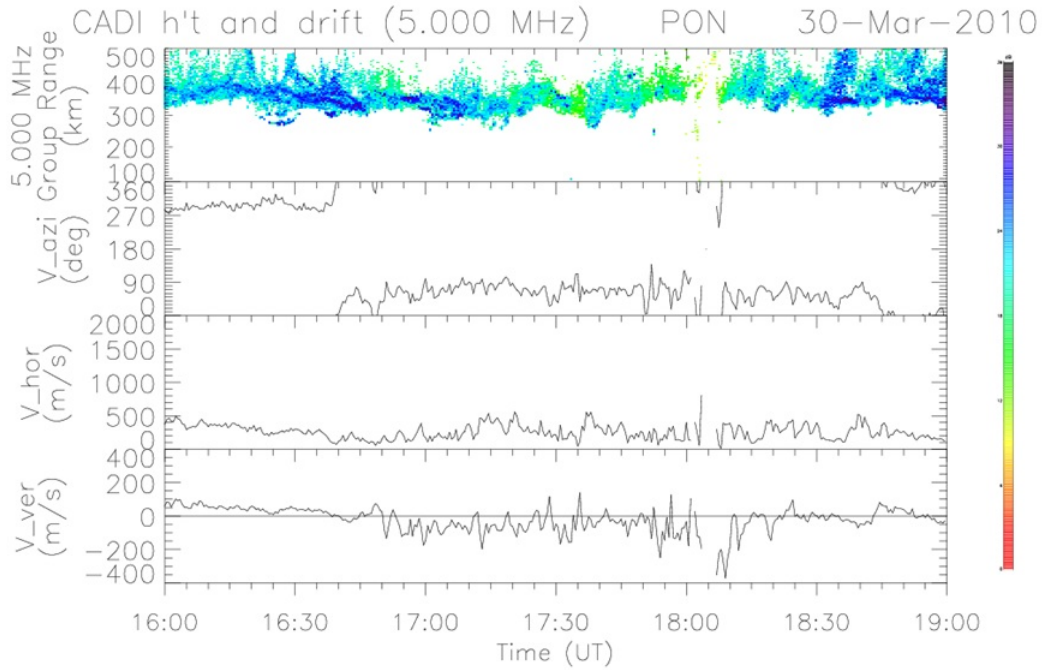

Figure 2.15: Three-hour ionosphere drift information obtained from the CADI at PondInlet, Canada, on 30 March 2010 at 16:00-19:00 UT. Virtual height of the ionosphere is shown in the top panel followed by the horizontal velocity azimuth (degrees) and magnitude (m/s).

θ_i= zenith angle of the ith source.

ϕ_i= azimuth angle of the ith source.

d_i= Doppler shift of the ith source.

λ = wavelength of the wave used.

An example of a plot showing the ionospheric drift for PondInlet, Canada, on 30 March 2010 at 16:00-19:00 UT is shown in Figure 2.15. The ionosonde gives valuable height, electron density and drift information, but only up to

the height of maximum electron density as mentioned earlier. Ionospheric measurements obtained using the ionosonde however are very local. To get a much wider perspective of the ionosphere, one has to use an instrument with more extensive temporal and spatial coverage. In the last two decades, such an technique GPS, was developed and is being used extensively for ionospheric research. Given its extensive worldwide reach, it is considered to be one of the best technique to study the ionosphere. Chapter 3 deals with GPS concepts that are used to study the ionosphere.

Chapter 3

Global Positioning System

3.1 Introduction

The Global Positioning System (GPS) is a constellation of satellites around the Earth which transmit radio waves continuously towards the Earth. This system was initiated in 1973 as a space-based satellite positioning and navigation system and was fully operational by 1994. It is maintained and run by the United States Department of Defense. At any given time, there are atmost 32 GPS satellites orbiting around the Earth at a height of ≈20200 km with an orbital period of 12 sidereal hours. They complete two revolutions in one sidereal day. GPS satellites are distributed into six almost circular orbital planes at a 55^0 inclination relative to the plane of Earth's geographic equator which means that receivers at high latitudes, above 55^0 N/S, can never observe a satellite at 90 degree elevation. These satellites transmit

information on "carrier" signals. Two main "carrier" signals that are being transmitted by GPS for civilian usage are L1 (1.575 GHz) and L2 (1.228 GHz). Another new civilian carrier signal L5 (1.176 GHz) was introduced in 2010, however this signal is not studied in the this dissertation. L1, L2 carrier signals are modulated with pseudorandom noise codes and information before being transmitted from the satellite.

3.1.1 GPS Signal Structure

Two basic types of codes that are modulated on to the "carrier" signals are 1) ranging codes and (2) navigation messages [40, 28]. Ranging codes are of two kinds : 1) Coarse/Acquisition (C/A) code and (2) Precision (P) code. C/A code is a 1,023 bit sequence called a pseudo-random binary sequence (PRN) which is transmitted at 1.023 MBits/sec, which means, the C/A code is repeated every one millisecond. Each satellite transmits a unique PRN code which correlates well only with itself and not any other satellite's PRN code. This allows the receiver to know the identity of the satellite from which it is receiving the signal and thus each satellite is identified with its unique PRN code. P-code is also a PRN code but the length of the code is 6.1871×10^{12} bits long and is transmitted at 10.23 Mbits/sec which is equivalent to transmitting the signal once a week. Owing to its high frequency, the P-code is much more precise than the C/A code. The C/A code is modulated only on the L1 signal while the P-code is modulated on to both L1 and L2 signals.

Along with the ranging codes, every satellite transmits a navigation message containing information about the satellite's position and health. This navigation message is transmitted at a rate of 50 bits/sec for 12.5 minutes. The navigation message has three main parts:

1) GPS date and time and information about the satellite's health.

2) Ephemeris data including satellite clock data; these data can be used to calculate the exact position of the satellite.

3) An almanac containing information about the locations of all satellites, PRN codes, etc.

3.1.2 Positioning Technique

As already indicated, GPS was designed for positioning and navigation purposes. The basic technique used to find an accurate position of a receiver is to have at least four satellites in sight. Three satellites are needed to obtain the three-dimensional location (latitude, longitude, height) of the receiver. The fourth satellite is used to estimate the offset between the receiver clock and the GPS time. The basic principle used in finding the three-dimensional location is through transliteration, i.e., by finding the distance between the receiver and three different satellites. This would give three equations with three unknowns (latitude, longitude and height). Thus these equations can be solved to determine the three unknowns. To obtain the distance between the receiver and the satellites, one can use either ranging codes or relative phase of the carrier signals [40, 28].

Pseudorange: The distance obtained using the ranging codes is called the pseudo range. This pseudorange is obtained by first calculating the lag between the receiver generated P or C/A code on the Earth and the received P or C/A code from the satellite. This lag represents the time taken by the signal to travel from the satellite to the receiver. This lag is then multiplied with the speed of light to obtain the distance between the satellite and the receiver. For this method to work perfectly, the receiver clock and the satellite clocks should be synchronized. This range is called the pseudorange because it's not the real range but an "apparent" range as there is delay due to the ionosphere, atmosphere, clock errors, instrumental delays and other errors.

An important error that occurs in GPS measurements is multipath. This happens when the signal from the satellite reflects from surrounding objects and this reflected signal interferes with the direct signal coming from the satellite. This interference causes the signal to fluctuate quasi-randomly and hence multipath errors cannot be modeled easily. The effect of multipath, however, can be reduced by techniques that will be discussed in Section 3.3.

The following two equations represent the pseudo ranges using P code on L1 and L2 signals, respectively [40, 28]:

$$P_1 = \rho + c.(dT - dt) + d_{ion,L1} + d_{trop} + b^{s_i,L_1} + b_{r_j,L_1} + mp_{p_1} + \epsilon_{p_1} \quad (3.1)$$

$$P_2 = \rho + c.(dT - dt) + d_{ion,L2} + d_{trop} + b^{s_i,L_2} + b_{r_j,L_2} + mp_{p_2} + \epsilon_{p_2} \quad (3.2)$$

where:

P_1, P_2 = Pseudo range measurements on L1 and L2 signals respectively, given in distance units

ρ = Geometrical distance between the receiver and the satellite

c = Vacuum speed of light

dT, dt = Offsets of the satellite and receiver with GPS time, respectively

$d_{ion,L1}$, $d_{ion,L2}$ = Ionospheric delays on L1, L2, respectively in distance units

d_{trop}= Tropospheric delay

b^{s_i,L_1}, b^{s_i,L_2} = Satellite instrumental delays for a particular satellite s_i on L1, L2, respectively

b_{r_j,L_1}, b_{r_j,L_2} = Receiver instrumental delays for a particular receiver r_j on L1, L2, respectively

mp_{p_1}, mp_{p_2} = Multipath on L1, L2, respectively

ϵ_{p_1}, ϵp_2 = Receiver noise on L1, L2, respectively

Phase distance : The distance between the receiver and the satellite can also be measured by finding the relative phase difference between the receiver-generated carrier signal and the received carrier signal from the satellite. This

phase difference can be obtained by differencing the squared receiver generated signal with the squared received satellite signal. Squaring the signals would eliminate the phase modulated P and C/A codes. This differenced signal is nothing but the beat pattern between these two signals.The phase of this beat pattern gives the phase difference between the received and the generated signal that can then be used to calculate the path difference or the range between the receiver and satellite given their clocks are well synchronized. One thing to note here is that this range is an ambiguous measure as only the relative phase difference is known; the total number of cycles completed between the receiver and satellites is not known. The following two equations represent the range calculated using the relative phase [40, 28]:

$$\Phi_1 = \rho + c.(dT - dt) + \lambda_1 N_1 - d_{ion,L1} + d_{trop} + b^{\Phi,s_i,L_1} + b_{\Phi,r_j,L_1} + mp_{p_1} + \epsilon_{\Phi,p_1} \tag{3.3}$$

$$\Phi_2 = \rho + c.(dT - dt) + + \lambda_2 N_2 - d_{ion,L2} + d_{trop} + b^{\Phi,s_i,L_2} + b_{\Phi,r_j,L_2} + mp_{p_2} + \epsilon_{\Phi,p_2} \tag{3.4}$$

where:

Φ_1, Φ_2 = Phase range measurements on L1 and L2 signals, respectively given in distance units

ρ = Geometrical distance between the receiver and the satellite

c = Vacuum speed of light

dT, dt = Offsets of the satellite and receiver with GPS time, respectively

λ_1, λ_2= Wavelengths of L1 and L2 signals, respectively

N_1, N_2 = Unknown L1, L2 carrier phase ambiguities

$d_{ion,L1}$, $d_{ion,L2}$ = These are the ionospheric delays on L1, L2, respectively in distance units

d_{trop}= Tropospheric delay

b^{Φ,s_i,L_1}, b^{Φ,s_i,L_2} = Satellite instrumental delays on phase for a particular satellite s_i on L1, L2, respectively

b_{Φ,r_j,L_1}, b_{Φ,r_j,L_2} = Receiver instrumental delays on phase for a particular receiver r_j on L1, L2, respectively

mp_{p_1}, mp_{p_2} = Multipath on L1, L2 carrier phase, respectively

ϵ_{p_1}, ϵ_{p_2} = Receiver noise on L1, L2 phase, respectively

Using equations (3.1) to (3.4), one can find the distance between the receiver and satellite and thus the position of the receiver. It is to be noted that there is a change of sign for d_{ion} in the phase range equations when compared to pseudorange equations. This change in sign is to take into account the phase advance and group delay of the signal. Even though one can obtain these approximate satellite and receiver instrumental delays using models, as already mentioned, errors such as the receiver noise and multipath cannot be modeled easily. Various differencing techniques can be obtained by manipulating equations (3.1) to (3.4) in an attempt to minimize most of the errors [40, 28]. An accuracy of one metre for positioning can be obtained using pseudorange while an accuracy down to centimetres can be achieved using carrier phase

techniques under certain conditions. [40]

In this dissertation, we are interested in how we can use this information to quantify the ionospheric effect. The most commonly used quantitative index for measuring the ionosphere using GPS is the total electron content (TEC).

3.2 Total Electron Content

Total electron content (TEC) can be defined as the number of electrons within a 1m radius along the ray path starting from the satellite to the receiver. It is usually represented in TEC units (TECU) where 1 TECU = 1×10^{16} electrons/m^2. To calculate TEC of the ionosphere using GPS, one needs to use equations (3.1) to (3.4) along with the Appleton Hartrees' equation (equation (2.2)) [35, 40]. The first step in this analysis is to convert the term d_{ion} in equations (3.1) to (3.4) in terms of TEC. By integrating equation (2.5) along the ray path, it can be easily shown that :

$$d_{ion} = const.\frac{TECU}{f^2} \tag{3.5}$$

where

TECU = Total Electron Content in TEC units (1TECU = 10^{16}electrons/m^2)

and from this, the relation between ionospheric path delay at two different

frequencies is:

$$d_{ion,L2} = \frac{f_1^2}{f_2^2} d_{ion,L1} \tag{3.6}$$

Using this relation and equation (3.1) to (3.4), it is easy to show that [40, 28] :

$$TEC_P = 9.52(P_2 - P_1)TECU \tag{3.7}$$

$$TEC_\Phi = 9.52(\Phi_1 - \Phi_2)TECU \tag{3.8}$$

The TEC obtained using pseudo-range values (TEC_P) are absolute but very noisy in nature, while the TEC obtained using phase range values (TEC_Φ) are very precise but ambiguous in nature. In order to get an unambiguous and precise TEC, TEC_Φ, and TEC_P can be combined in a method called "phase leveling". The basic idea behind phase leveling is to bring the phase derived TEC (TEC_Φ) to the level of the pseudo-range derived TEC (TEC_P). The most commonly used method is finding the difference between TEC_P and TEC_Φ for every satellite path and adding this difference to TEC_Φ as shown in equation (3.9) [40, 28]:

$$TEC_{phaseleveledarc} = TEC_{\Phi,arc} + |TEC_P - TEC_\Phi|_{arc} \tag{3.9}$$

It should be noted that these TEC are along the ray-path and usually at mid latitudes, they have an elevation angle between 0-90 degrees and while receivers at high latitudes can never see a satellite near 90 degrees elevation.

Therefore the TEC obtained along the ray-path with less than 90^o elevation angle is called slant TEC. This slant TEC is then mapped to the vertical to obtain vertical-TEC, which can be considered an equivalent of TEC directly overhead of the receiver.

3.2.1 Vertical TEC

Assuming that there are no horizontal gradients in the ionosphere, slant-TEC is usually mapped to the vertical so that the TEC does not depend on the relative locations of the satellite and the receiver. This is done by assuming the ionosphere to be a thin shell at a height called the "shell-height". This shell-height by definition is the height at which the electrons are distributed equally below and above it and this height is close to the peak height of the F-layer in the ionosphere which is assumed to be around 350 km. The point at which the ray path intersects this thin shell is called the ionospheric pierce point (IPP) as shown in the Figure 3.1. This is the point where the whole TEC of that particular ray path is considered to be concentrated [40, 28]. This slant TEC at the IPP is then mapped to the vertical using a mapping function. The mapping function (M(e)) used in this thesis is [40] :

$$M(e) = cos[arcsin(cos(e)\frac{R_e}{R_e + h})] \tag{3.10}$$

where

e = Elevation angle

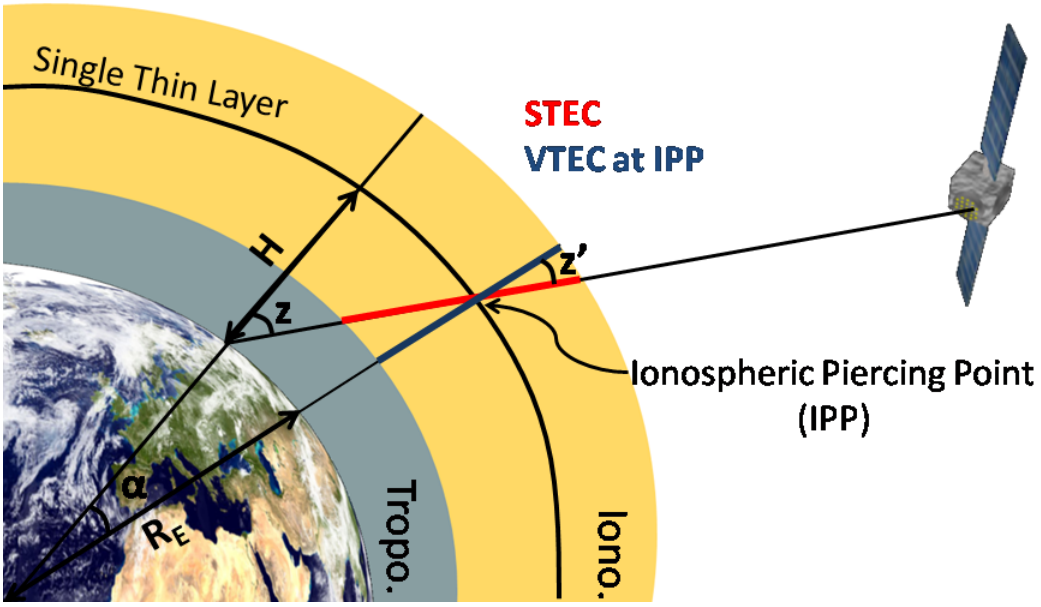

Figure 3.1: Diagram representing the thin shell assumption and also the ionospheric pierce point (IPP), slant-TEC (STEC), vertical-TEC (VTEC) are shown. Courtesy: Royal Observatory of Belgium.

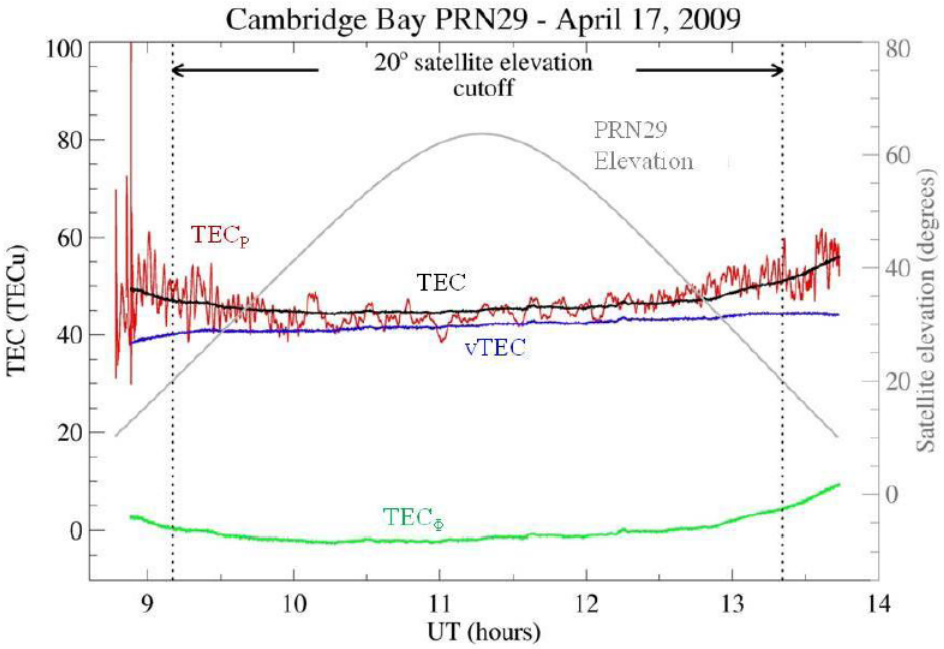

Figure 3.2: Color coded examples of phase and code derived TEC, phase leveled TEC, vertical TEC, and satellite elevation. A satellite elevation cutoff of 20^o is indicated by vertical dotted lines [70].

R_e= Radius of Earth

h= Shell height

The vertical TEC (vTEC) is obtained by using the slant TEC (sTEC) and the mapping function in the following way:

$$vTEC = sTEC * M(e) \tag{3.11}$$

An example of slant TEC observed on a particular satellite PRN 29 on 17 April 2009 at Cambridge Bay is shown in Figure 3.2. The vertical TEC and

phase-leveled TEC are are shown in this example.

Other mapping functions have been developed or described in literature. However, studies have shown that the mapping function used in this dissertation yields better results [40]. Another assumption that needs to be flagged is the use of 350 km as the fixed shell height. It is known that the shell height changes with time and location. This assumption can lead to errors in precise-positioning applications of GPS. This is discussed more in the following section.

3.2.2 Combined TEC Analysis using ionosonde and GPS

As mentioned in Section 3.2.1, the shell height can be approximated as the peak height of the F layer in the ionosphere and this F layer peak height can be obtained using an ionosonde. Since the ionosphere at high latitudes is very active, the F-layer height changes continuously [30]. To check the variability of shell height, ionosonde data obtained from Resolute Bay for the 11, 12 and 15 November 2006 are analyzed. Figure 3.3 shows this distribution of shell/peak heights.

It can be clearly seen that the shell height is not constant but can vary from 200 km to 400 km in the example. Thus using a fixed-shell height (350 km)

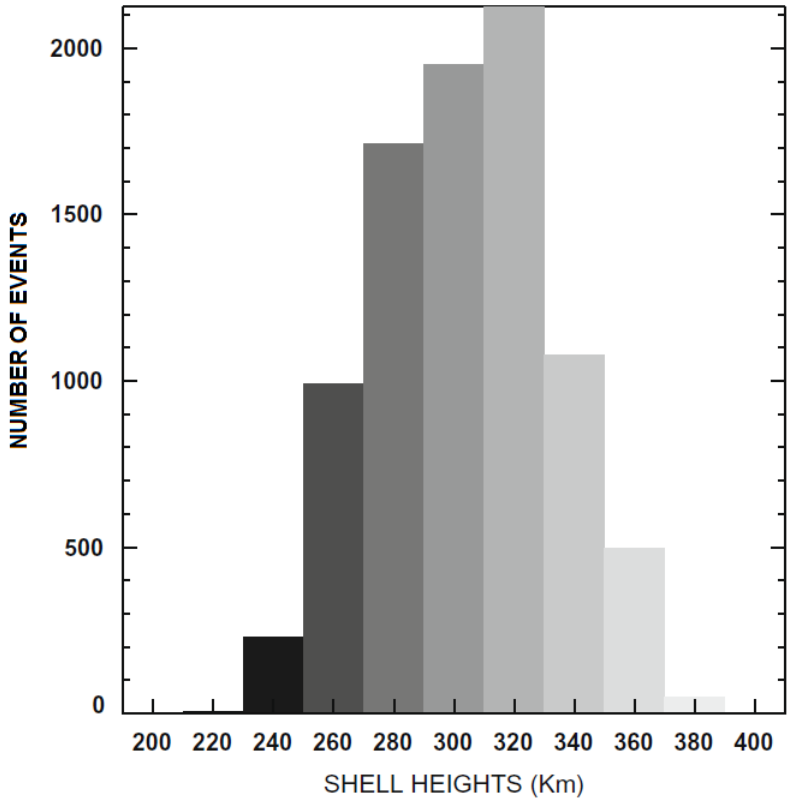

Figure 3.3: Distribution of shell heights derived from the ionosonde at Resolute Bay on 11, 12 and 15 November 2006. It was observed that the shell heights varied from about 200 km to 400 km. Most shell heights were observed in the range of 280-320 km. A bin value of 20 km was used in the figure.

could obviously lead to errors in TEC calculations, which in turn may cause errors in precise-positioning applications. In an attempt to overcome this, a new method was introduced in this thesis, where ionosonde-derived shell heights were used as inputs to the mapping function. Figure 3.4 shows the difference between TEC derived from GPS using a fixed shell height at 350 km and using varying shell heights from an ionosonde plotted with respect to shell heights and peak frequency. It should be noted that satellite biases and the receiver biases for this work are obtained from the University of Bern ((http://www.aiub-download.unibe.ch/CODE/).

It can be observed that in Figure 3.4(a), there is a difference of up to 0.3 TECU when using a fixed-shell approach and also as shown in Figure 3.4(b) this difference increases as the peak frequency increases. This peak frequency is the plasma frequency of the electron density layer at the peak layer and it is directly proportional to the electron density. Thus, if the ionosphere is active, while using a fixed-shell approach, the difference would be much larger and thus introducing a larger error in precise positioning and navigation applications. Using a fixed-shell approach is a good approximation for quiet day studies but as the ionosphere becomes active, this method will not give precise results. Therefore, to obtain better precision results one has to take the varying shell heights into account.

In this dissertation, TEC obtained using ionosonde and GPS were also com-

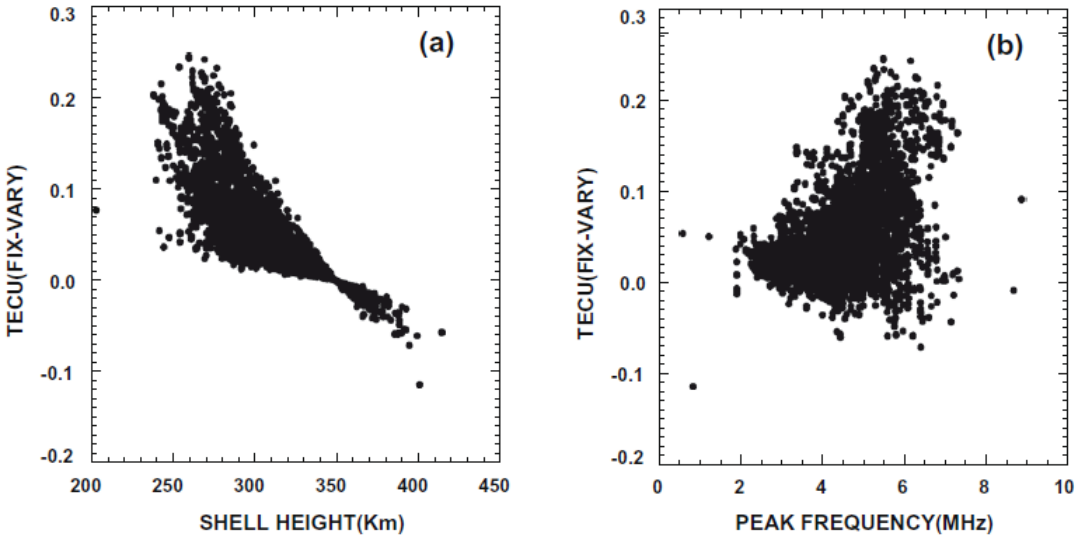

Figure 3.4: The difference between the total electron content derived from GPS using a fixed shell height analysis with shell height at 350 km and using varying shell heights analysis is plotted against (a) shell height and (b) peak frequency. Data were obtained at Resolute Bay on 11, 12, 15 November 2006. The varying shell heights were obtained from ionosonde at Resolute Bay. The difference is observed to increase with the electron content in the ionosphere.

pared. Since an ionosonde provides information only of the bottomside (upto the peak of the F layer), the topside of the ionosphere should be modeled. Two topside models, the Chapman model and exponential model, were compared. Mathematically, the Chapman model is given by [13] :

$$N = N_o exp\frac{1}{2}[1 - z - exp(-z)] \tag{3.12}$$

where

z=((h-h$_o$)/H)

N= Electron density at h.

N$_o$=Peak electron density at peak height h$_o$.

H = Scale height of the ionosphere.

while the equation for the exponential model is given by [35] :

$$N = N_R exp[(h - h_R)/H] \tag{3.13}$$

where

N$_R$= Electron density at a reference height h$_R$.

H= Scale height of the ionosphere.

It should be noted that the input to these models, like the scale height, which is the height for which the scale height declines by a factor of e, the peak frequency, and the peak height are obtained from POLAN [66]. Once the

topside models are incorporated with the bottomside profile, the whole profile is integrated along the height (h) to obtain the ionosonde derived TEC. Figure 3.5 shows vertical TEC obtained by GPS (average of all satellites) compared with TEC obtained from ionosonde using the exponential top-side model and the Chapman top-side model, respectively. The data for this plot are obtained from Resolute Bay (74.750^{o}N, 265.00^{o}E, geog.) for 11 November 2006.

It can be clearly observed from Figure 3.5 that the TEC derived from the ionosonde using the Chapman model clearly follows the GPS derived TEC at most times, unlike the TEC derived using the exponential model. In an attempt to ascertain which top-side model (exponential or Chapman) gives a better result with the GPS-derived TEC, both the exponential-derived TEC and the Chapman-derived TEC for 11, 12 and 15 November 2006 at Resolute Bay (74.750^{o}N, 265.00^{o}E, geog.) were correlated with GPS TEC obtained for the same place and time. Figures 3.6 (a) and (b) show the scatter plots of the ionosonde-derived TEC (Chapman and exponential, respectively) and the GPS vTEC (using ionosonde-derived shell heights) for the three days chosen.

Agreement between TEC estimates from GPS and ionosonde (Chapman) is evident in Figure 3.6(a) (0.87 correlation coefficient and 0.89 as slope of the best fit line). From Figure 3.6(b), it is seen that the exponential function-derived TEC have much smaller values than those of the GPS-derived TEC

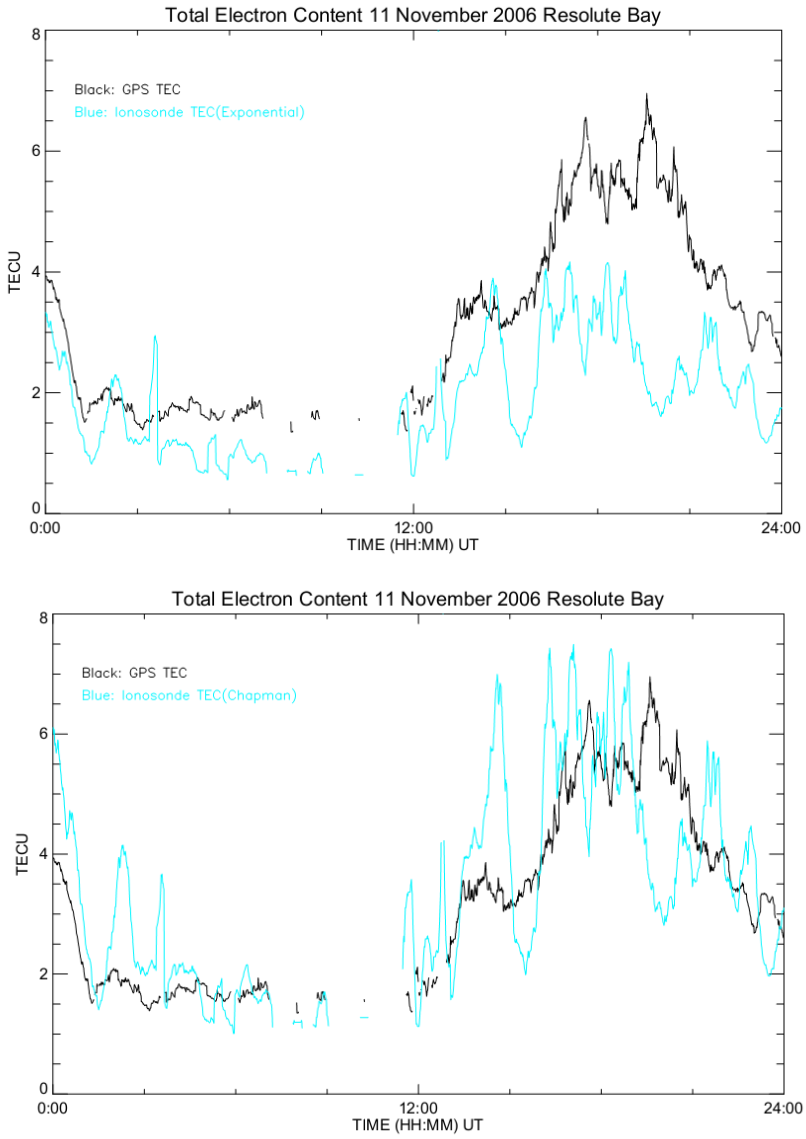

Figure 3.5: Comparison of TEC derived using ionosonde plus exponential topside model with GPS-derived vertical TEC and TEC derived using ionosonde plus Chapman topside model with GPS-derived vertical TEC. The data used were obtained from Resolute Bay (74.750^{o}N, 265.00^{o}E, geog.) on 11 November 2006.

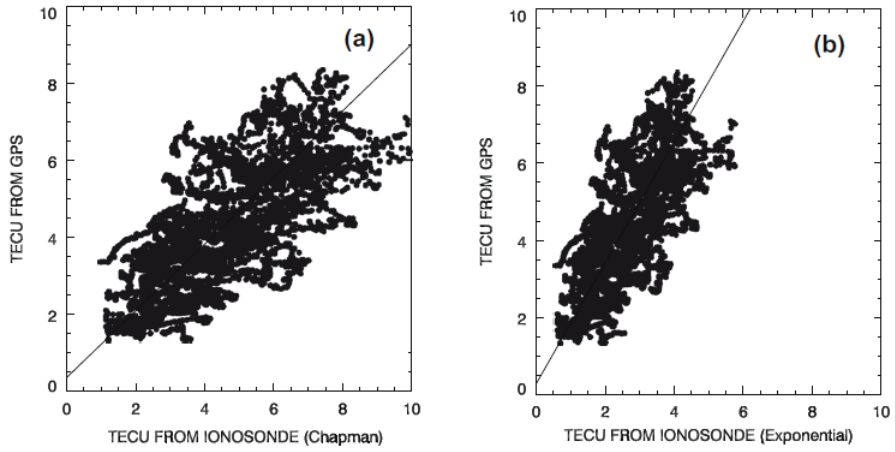

Figure 3.6: The correlation between the GPS derived TEC using varying shell heights and the total electron content obtained using ionosonde for (a) bottomside+Chapman topside model, (b) bottomside+exponential topside model. The straight line going through the plot shows the best fit line for that data set.

(0.87 correlation coefficient and 1.5 as slope of the best fit line). So the Chapman function (slope of the best fit line for the Chapman model-derived TEC = 0.89) seems to be a better function to model the polar topside ionosphere compared to the exponential function (slope of the best fit line for the exponential derived TEC = 1.5).

More elaborate studies are to be done on the validity of different topside models for the polar region. From the scatter plots (Figure 3.6(a) and Figure 3.6(b)) between the total electron content derived from GPS and total electron content from the ionosonde for all 3 days, it is also observed that the electron content derived from the ionosonde using a Chapman function

modeled topside profiles had a shift/bias of 0.36 TECU with the GPS-derived electron content, while that of the exponential function had a shift/bias of 0.28 TECU. At mid latitudes such a shift or bias in the scatter plot is usually attributed to plasmasphere electron content in ionospheric studies [45]. But since Resolute Bay station is in the polar region, the plasmasphere's contribution is negligible [30]. More study is required to explore these features in detail.

A maximum of 5 percent error can be attributed to the ionosonde-derived bottomside TEC due to manual scaling [29]. Hence most of this shift or bias observed in these results was mainly due to the following reasons. The first reason is the receiver bias. It has to be noted that receiver biases used were monthly averages. Recent studies also show that for higher latitudes above 60^oN/S, there is no proven method to calculate an accurate receiver bias [53]. The second reason that may affect the bias is the mapping function. The general mapping function that was used was optimized for mid- and low-latitudes, where the highest elevation angle of the GPS satellites can be 90^o [40]. For higher latitudes this is not true since the satellite elevation angle is never 90^o. This indicates that more studies are required to design a mapping function for higher polar latitudes and for receiver bias calculations for GPS receivers at high latitudes given the activity in the higher latitude ionosphere. Precise ionospheric studies should also include varying shell heights since the ionosphere is not constant in time. The third reason

can be due to the topside model used for ionosonde analysis. The Chapman function seems to be a better function compared to the exponential function to model the topside ionosphere for polar latitudes. One still has to study different topside models to find a model that would give a better result for the polar ionosphere given its variability. Along with these studies, one has to take into account the errors like satellite biases, and multipath to obtain much more precise positioning results.

3.3 Multipath

As shown in Figure 3.7, multipath occurs due to the interference between a direct signal from the satellite and the signal reflected off a nearby obstacle. This interference cause fluctuations in the signal which in turn can introduce error into the GPS measurements. A common technique to mitigate multipath is to use an elevation cutoff so that signals from lower elevations which are thought to be more prone to multipath are removed. Even though this technique works for most cases, there are multipath events observed at higher elevations also. Another technique that is used to remove multipath is by observing the signal for consecutive days. Assuming the obstacle has not changed its position, one should observe multipath signature in the signal every day but with a ≈4.0 minute delay as shown in Figure 3.8. This ≈4 minute delay is because the GPS satellites arrive approximately at the same point in space with respect to the receiver every ≈23 hr 56 min (one sidereal

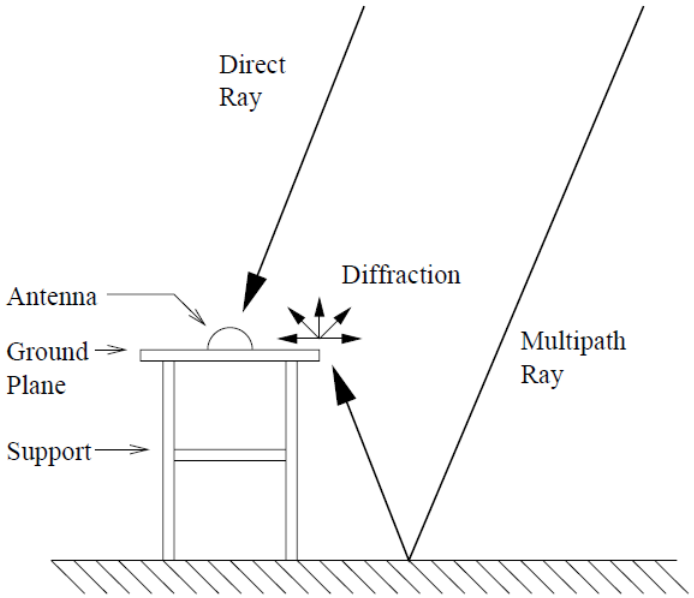

Figure 3.7: Sketch of hypothesized diffraction of multipath ray around the ground plane for a high elevation satellite and an elevated GPS antenna. [9]

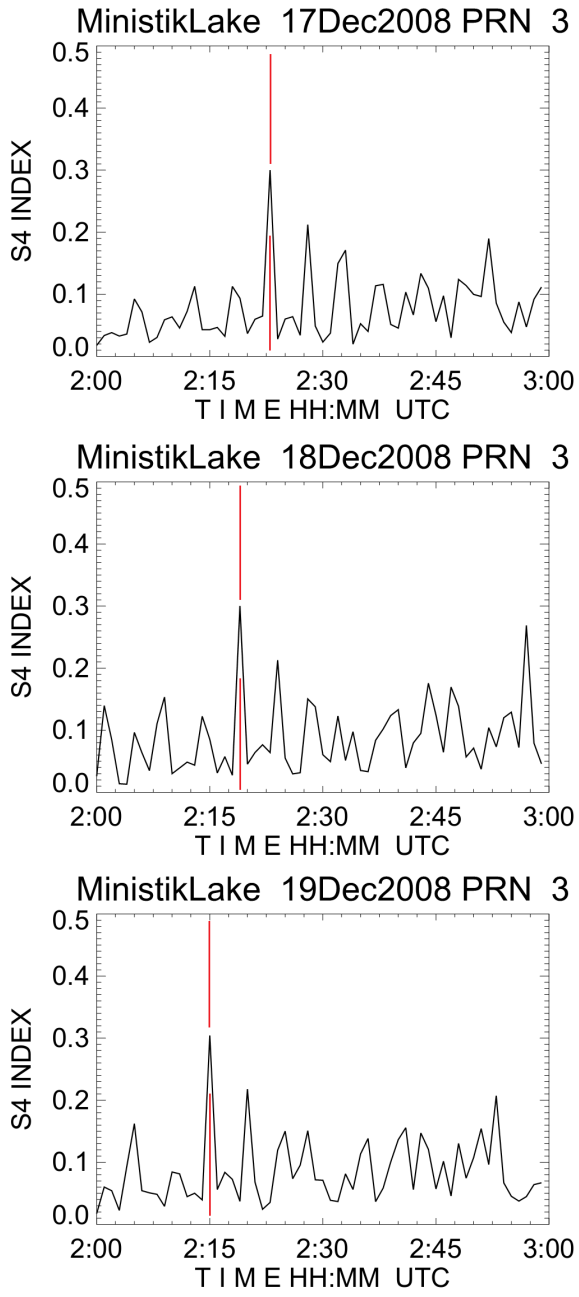

Figure 3.8: S_4 observed at Ministik Lake (53.5^0 N, 247.03^0E) on 17, 18 and 19 December 2008 respectively is shown here. It can be seen that a peak in S_4 (denoted by red line) is observed with a ≈4 minute delay the next day. This is a typical multipath signature which can be used to remove multipath signals from the analysis.

day). This approach can be very useful in eliminating signals with multipath signatures [40, 9].

In this study, these multipath elimination techniques were implemented to remove all possible multipath-corrupted signals before further signal analysis was carried on. Things get more complicated when there is scintillation. Scintillation occurs when the GPS signal is diffracted due to the ionospheric irregularities. This causes an interference pattern similar to multipath in the signal [40, 9]. The gist of this discussion is that both scintillation and multipath can have similar signatures. Hence to study scintillation, multipath should be mitigated using all the above mentioned techniques. Chapter 4 will discuss scintillation in more detail and the importance of studying scintillation.

Chapter 4

Scintillation

4.1 Introduction

In 1946, a group of radio astronomers observed fast fluctuations in the signal for short intervals of time while analyzing data from radio source Cygnus A [27]. It was initially believed that these fluctuations were an inherent property of the source. Later studies [62, 25] have found that there was no correlation between observations recorded at two stations some distance apart even though both receivers were observing the same source. This led to the suggestion that this was more a local phenomenon. Later it was proven that these are due to the radio signal being affected by the electron density irregularities present in the ionosphere as the signal traverses through them. Henceforth these fluctuations in the signal were called ionospheric scintillation [62, 25]. Scintillation research has a two-fold interest [75]. On

one hand, scintillation has a significant impact on satellite communications and navigation systems as the receivers have trouble keeping lock with the fluctuating signal, which in turn will introduce errors [11, 72]. Sometimes scintillation can be intense enough to make the receiver lose lock completely with the signal thus creating a signal outage. Thus scintillation becomes a very important phenomenon to be considered when designing communication and navigation systems [11, 72]. On the other hand, scintillation also has an important place in ionospheric research since information about the electron density structures present in the ionosphere can be deduced by studying the scintillation signal that has traversed it. This information will then help to understand the physical processes that take place in the ionosphere [7, 72].

After the launch of the first artificial radio satellite in 1957, the interest in radio scintillations increased [36, 76]. During the early 1970s, satellite beacon experiments like those of the Wide-band satellite, and the HiLAT satellite were specifically created to study scintillation [21]. These satellite systems mainly used UHF/VHF frequencies, which made it possible to build a world-wide climatology of scintillation. These studies were also one of the first to show that scintillation-producing irregularities follow a power-law structure. These results enhanced the understanding of scintillation especially in the UHF/VHF range. Scintillation can occur in many frequency bands but the main interest of this work lies in the scintillation that occurs in the L-band (1-2 GHz). This band is very important as most tele-communication sys-

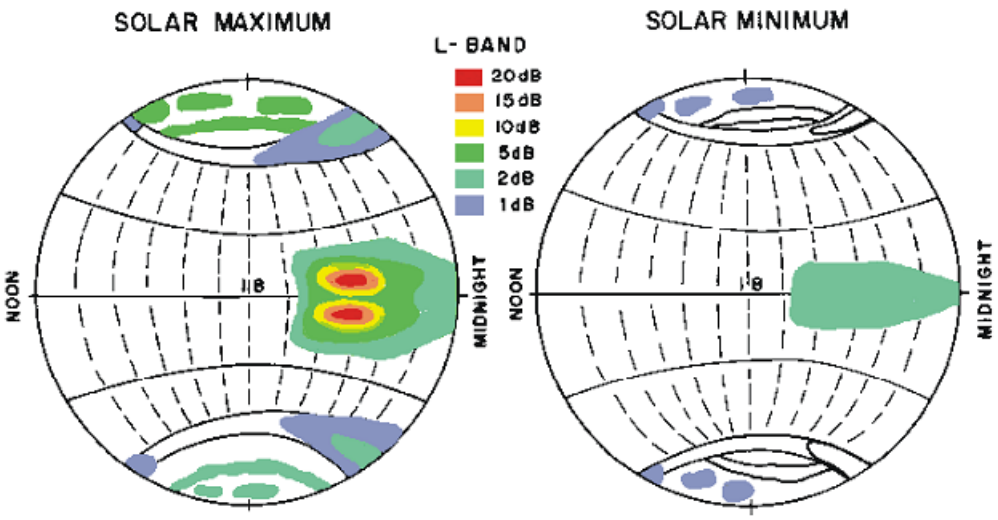

Figure 4.1: Global variations of scintillation fades observed during solar maximum and solar minimum. [7]

tems, like the Iridium satellite system, use this band (1.6 GHz). In addition, navigation systems like GPS have their carrier signals in this band (1.1-1.3 GHz) [7]. Before the advent of GPS, information about scintillation at L-band frequencies was usually obtained by extrapolating results from radars and satellites that used UHF/VHF ranges [21, 7]. Figure 4.1 shows the global distribution of ionospheric scintillation at L-band frequencies obtained from both solar minimum and solar maximum conditions. Note that in Figure 4.1, the activity levels that are expressed in the L-band are derived from actual L-band observations for equatorial and mid-latitudes, while for higher latitudes they are derived from extrapolations from 250 MHz [7].

A basic question that arises when studying scintillation is how rapid fluctuations in a radio signal's amplitude and phase that were received at the ground can reveal information about irregularity structures in the ionosphere which are some 350 km from the Earth's surface. Answering this question requires the development of scintillation theories/models. These models [58, 59] try to connect the observations on the ground to the irregularities in the ionosphere by studying how a radio signal is affected by these irregularities. Before delving into these theories, a good starting point is Maxwell's equations, as these can be used to explain how an electromagnetic wave is generated, propagated, and the effects of the medium of propagation on this wave.

4.2 Maxwell's Equations and Electric Field Vector Equations

Maxwell's equations are a set of partial differential equations that form the basics of classical electrodynamics, circuit theory, and classical optics [73]:

$$\nabla.\vec{D} = \rho_e \tag{4.1}$$

$$\nabla.\vec{B} = 0 \tag{4.2}$$

$$\nabla \times \vec{H} = \frac{\partial \vec{D}}{\partial t} + \vec{J} \tag{4.3}$$

$$\nabla \times \vec{E} = -\frac{\partial \vec{B}}{\partial t} \tag{4.4}$$

Here $\vec{J}$ is the current density and ρ_e is the net charge density, $\vec{E}$ is the Electric Field and $\vec{B}$ is the magnetic field, $\vec{D}$ is the displacement field and $\vec{H}$ is the induction field. The induction field ($\vec{H}$) is related to the magnetic field ($\vec{B}$) through the relation:

$$\vec{B} = \mu\vec{H} \tag{4.5}$$

where μ is the magnetic permeability and $\mu = \mu_0\mu_r$, where μ_0 is the permeability of free space and μ_r is the relative permeability of the medium and $\mu_r \cong 1$ for the ionosphere. Similarly, the electric field in the medium ($\vec{E}$) is related to the displacement field ($\vec{D}$) through the dielectric constant of the medium (ϵ) in the following way:

$$\vec{D} = \epsilon\vec{E} \tag{4.6}$$

ϵ can also be denoted as $\epsilon = \epsilon_r\epsilon_0$. Here ϵ_0 is the permittivity of free space and ϵ_r is the relative permittivity of the medium.

Equations (4.1) and (4.2) are known as Gauss's law and Gauss's law for magnetism, respectively. Equation (4.3) is known as Ampere's law with Maxwell's correction. Ampere described how a magnetic field is created when there is current density and Maxwell added that the magnetic field can also be formed by changing the electric field and thus the name Ampere's law with Maxwell's correction. The last equation (4.4), is known as Faraday's law

of induction. It states how a time-varying magnetic field creates an electric field. Maxwell's equations, when combined, can describe the generation and propagation of electromagnetic waves in a medium. In order to do that first one needs to characterize the propagation medium. This can be achieved by using the dielectric constant, ϵ, as it contains all the information that is required to describe the medium of propagation. For that we need to further decompose ϵ_r into its average value and another component, which is a stochastic function that describes the fast changes in the medium:

$$\epsilon_r(\vec{r}, t) = \langle \epsilon \rangle \left[1 + \epsilon_1(\vec{r}, t)\right] \tag{4.7}$$

Here, $\langle \epsilon \rangle$ represents the average value, while $\epsilon_1(\vec{r}, t)$ represents the fluctuating part of the medium. These variables can then be used to obtain the electromagnetic wave equation in that particular medium. In order to obtain the electromagnetic wave equation, it is first assumed that region has no current sources ($\vec{J}$=0) and then combine the Maxwell equations, (4.3) and (4.4), in the following way [73]:

$$\begin{aligned}
\nabla \times \nabla \times \vec{E} &= -\nabla \times \frac{\partial \vec{B}}{\partial t} \\
&= -\frac{\partial}{\partial t}\left(\nabla \times \mu \vec{H}\right) \\
&= -\frac{\partial}{\partial t}\left(\frac{\partial \mu \vec{D}}{\partial t}\right) \\
&= -\frac{\partial^2}{\partial t^2}\left(\epsilon \mu \vec{E}\right) \\
&= -\frac{\partial^2}{\partial t^2}\left(\epsilon_0 \mu_0 \epsilon_r \mu_r \vec{E}\right) \\
&= -\frac{\partial^2}{\partial t^2}\left(\frac{1}{c^2}\epsilon_r \vec{E}\right) \qquad (4.8)
\end{aligned}$$

The double curl operator can be further simplified using :

$$\nabla \times \nabla \times \vec{E} = -\nabla^2 \vec{E} + \nabla\left(\nabla . \vec{E}\right)$$

From equation (4.6) and assuming $\nabla . \vec{D} = 0$ we get,

$$\nabla . \vec{D} = \nabla . \left(\epsilon \vec{E}\right) = \vec{E} . \nabla \epsilon + \epsilon \nabla . \vec{E} = 0$$

and therefore,

$$\nabla . \vec{E} = -\vec{E} . \nabla \left(log \epsilon\right)$$

Combining these equations we can obtain the following:

$$\nabla^2\vec{E} - \frac{1}{c^2}\frac{\partial^2}{\partial t^2}\epsilon_r\vec{E} = \nabla\left(-\vec{E}.\nabla\left(log\epsilon\right)\right) \tag{4.9}$$

Approximating the term $\nabla\left(-\vec{E}.\nabla\left(log\epsilon\right)\right) = 0$ by assuming an isotropic medium and substituting the value of ϵ_r, the electromagnetic wave vector equation is in the form:

$$\nabla^2\vec{E} - \frac{1}{c^2}\frac{\partial^2}{\partial t^2}\left\langle\epsilon\right\rangle\left[1+\Delta\epsilon\right]\vec{E} = 0 \tag{4.10}$$

We Substitute $E(\vec{r},t) = E(r)e^{-j\omega t}$ in equation (4.10), and take into account the following assumptions [75]:

1) A region of random irregular electron density structures is assumed to be located at a certain height above the ground with a thickness of "L".

2) The temporal variations in the irregularities are much smaller than the wave period.

3) The characteristic size of the irregularities is much greater than the wavelength.

Using the above approximations, the electric vector field equation, equation (4.10), can be written as a scalar equation inside the slab as :

$$\nabla^2 E(r) + k^2[1+\epsilon_1(r,t)]E(r) = 0, 0 < z < L \tag{4.11}$$

Here $k^2 = k_0^2 \langle \epsilon \rangle$ and $k_0 = \frac{2\pi}{\lambda}$ where k_0 is the wave number of the wave.
The solution of this equation forms the basis of scintillation theory but unfortunately this equation cannot be solved directly because of the stochastic nature of ϵ_1 and thus approximate solutions that agree with experimental results need to be derived. To do that one has to first understand and characterize the stochastic nature of ϵ_1.

4.3 Stochastic Nature of Scintillation

The study of wave propagation deals with space-time fields that are moving from one part of the medium to another part at a certain velocity. As the field propagates there may be a change in its shape, magnitude or its propagating velocity. To mathematically solve such a complex system, approximations are needed that can facilitate obtaining an answer. The task of understanding the problem of ionospheric scintillation is no exception as it also deals with complex fields changing in time and space. Thus it is better to describe the problem stochastically [75]. In describing scintillation, the variable that is of most importance is the electron density fluctuations, ΔN, which in turn causes the fluctuations in ϵ_1 described in Section 4.2. There have been a number of experimental results that have shown that the electron densities in the ionosphere are highly complex and irregular [14, 56, 8]. Owing to this, the medium of propagation should be described by its statistical properties. Let $\Delta N(\vec{r})$ be the electron density fluctuations and N_0 be the background

electron density. Usually a homogeneous random field, ς, with zero mean and with a standard deviation, σ_ς is defined with ς typically defined as $\frac{\Delta N(\vec{r})}{N_0}$ [75]. The auto-correlation function, B_ς of this field is defined as :

$$B_\varsigma(\vec{r_1} - \vec{r_2}) = \langle \varsigma(r_1)\varsigma(r_2) \rangle \tag{4.12}$$

here the angular brackets are used to denote an ensemble average. Considering the Wiener-Khinchin theorem, the auto-correlation, B_ς, and the power spectrum, Φ_ς, form a Fourier transform pair [75, 73]:

$$\Phi_\varsigma(\vec{k}) = (2\pi)^{-3} \int\int\int_{-\infty}^{\infty} B_\varsigma(\vec{r}) e^{-j\vec{k}.\vec{r}} d^3r \tag{4.13}$$

$$B_\varsigma(\vec{r}) = \int\int\int_{-\infty}^{\infty} \Phi_\varsigma(\vec{k}) e^{j\vec{k}.\vec{r}} d^3k \tag{4.14}$$

These relations are very important as they can be used to relate the deviations in the field that are observed at ground level to the irregularity structures present in the ionosphere. In order to achieve this, the electron density fluctuations ΔN need to characterized. To proceed with the analysis, a ray path pointed along the z-axis and traversing through the medium is assumed [75]. The phase fluctuations ($\Delta\phi$) along this ray path due to the electron density fluctuations are expressed as:

$$\Delta\phi(\vec{\rho}) = \int \Delta n(\vec{\rho}, z) dz \tag{4.15}$$

Here $\vec{\rho} = (x, y)$ is the transverse coordinate, Δn represents the fluctuations in the refractive index which are in turn caused by the electron density fluctuations, ΔN. From Chapter 2, the relation between the refractive index (n) and the electron density (N) is given to the first order by :

$$n = 1 - \frac{Ne^2}{2\omega^2 m_e \epsilon_0} \tag{4.16}$$

Therefore the relation between the change in refractive index (Δn) and the fluctuation in the electron density (ΔN) can be obtained by taking the derivative of equation (4.16) :

$$\Delta n = -\frac{\Delta N e^2}{2\omega^2 m_e \epsilon_0} \tag{4.17}$$

Substituting equation (4.17) into equation (4.15):

$$\Delta\phi(\vec{\rho}) = -\frac{\Delta N_T(\vec{\rho}) e^2}{2\omega^2 m_e \epsilon_0} \tag{4.18}$$

This variable ΔN_T is the deviation in the total electron content given by :

$$\Delta N_T = \int \Delta N(\vec{\rho}, z) dz \tag{4.19}$$

This relation, along with equation (4.12) can then be used to relate the correlation function of deviation of the total electron content (ΔN_T) to the correlation function of the deviations in the electron density (ΔN) by

$$B_{\Delta N_T}(\vec{\rho}) = z \int_{-\infty}^{\infty} B_{\Delta N}(\vec{\rho}, z) dz \tag{4.20}$$

Now using the Wiener-Khinchin theorem relating the correlation function to the power spectrum and using equation (4.20), the relation between the correlation function of deviation of total electron content (ΔN_T) and the spectrum of the ionospheric irregularities can be derived as :

$$B_{\Delta N_T}(\vec{\rho}) = 2\pi z \int\int_{-\infty}^{\infty} \Phi_{\Delta N}(\vec{k}_\perp, 0) e^{j\vec{k}_\perp \cdot \rho} d^2\vec{k}_\perp \tag{4.21}$$

where, $\vec{k}_\perp = (k_x, k_y)$. Using equation (4.18) and equation (4.12), a relation between the correlation function of the fluctuations in the path ($\Delta\phi$) and the correlation function of the deviations in the total electron content (ΔN_T) can also be obtained as:

$$B_{\Delta\phi}(\vec{\rho}) = (\frac{e^2}{2m\epsilon_0\omega^2})^2 B_{\Delta N_T}(\vec{\rho}) \tag{4.22}$$

Hence, by substituting equation (4.22) in equation (4.21), a relation between the correlation function of the path fluctuations to the spectrum of the ionospheric irregularities is obtained. This is a very useful relation as it helps characterize the irregularities just by observing the fluctuations in the phase of the signal. A point to remember in this analysis is that electron density fields are assumed to be frozen, i.e., all scattering irregularities are convected along with the same velocity and the changes in the irregularity are too slow compared to the time period of the signal. These statistical characterizations can be used in scintillation models to better understand scintillation phenomenon [75].

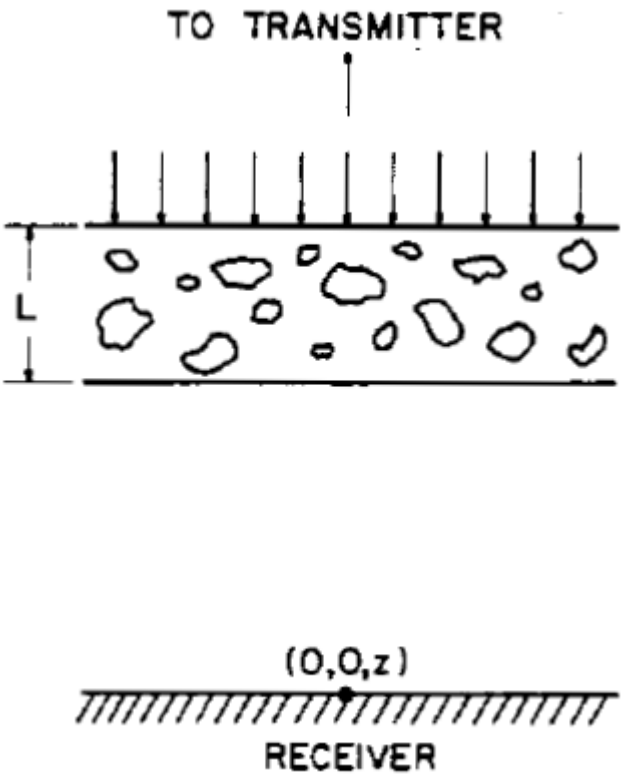

Figure 4.2: Geometry of scintillation problem analysis [75].

4.4 Scintillation Model

As a starting point in developing a scintillation model, a region of random irregular electron density structures is assumed to be located at a certain height above the ground with a thickness of "L", i.e., z = 0 to L, as shown in Figure 4.2.

It will be assumed that the irregular slab has a relative dielectric permittivity

of the form:

$$\epsilon(\vec{r},t) = \langle\epsilon\rangle\,[1+\epsilon_1(\vec{r},t)] \tag{4.23}$$

where $\langle\epsilon\rangle$ is the background average dielectric permittivity and $\epsilon_1(\vec{r},t)$ is the fluctuating part that characterizes the random variations due to the irregularities.

As discussed in Chapter 2, the dielectric permittivity of the ionosphere is given by :

$$\epsilon = \epsilon_0(1-\frac{e^2N}{m_e\omega^2\epsilon_0}) \tag{4.24}$$

and the change in dielectric permittivity of the ionosphere is given by :

$$\Delta\epsilon = -\frac{e^2\Delta N}{m_e\omega^2} \tag{4.25}$$

By using equations (4.23), (4.24) and (4.25), the average value of the dielectric permittivity ($\langle\epsilon\rangle$) and the fluctuating part of the dielectric permittivity (ϵ_1) can be obtained as :

$$\langle\epsilon\rangle = \epsilon_0(1-\frac{e^2N}{m_e\omega^2\epsilon_0}) \tag{4.26}$$

and $\epsilon_1(\vec{r},t)$ which is the fluctuating part that characterizes the random variations due to the irregularities is given by :

$$\epsilon_1(\vec{r},t) = \frac{(-\frac{e^2N}{m_e\omega^2\epsilon_0})[\frac{\Delta N}{N}]}{(1-\frac{e^2N}{m_e\omega^2\epsilon_0})} \tag{4.27}$$

Here, $\frac{e^2N}{m_e\omega^2\epsilon_0}$ can also be written as $\frac{f_p}{f}^2$ where f_p is the plasma frequency, f is the frequency of the propagating wave.N and ΔN are the background electron density and electron density fluctuations respectively. This shows that the fluctuations in dielectric permittivity that cause scintillation are directly proportional to the ratio of electron density fluctuations and the background electron density.

In order to understand scintillation in a qualitative way, it is assumed that as the wave traverses through the irregularity slab/layer, only the phase of the signal is affected by the random fluctuations in the refractive index. As this distorted wave front propagates to the receiver, it undergoes constructive and destructive interference resulting in amplitude and phase scintillation. This diffraction process depends on the size and strength of the irregularities. There may also be cases where the strength of the irregularities is so strong that the fluctuations in phase are so large that it can lead to saturation of amplitude scintillation. There may be cases where the irregularity slab is very thick and this in turn causes the amplitude of the wave to be distorted along with the phase. Hence the scintillation observed at the ground would be a combination of both these distortions.

To comprehend scintillation quantitatively, one has to invoke scintillation theories or models. To do this we need to start again with equation (4.11) that describes the wave equation in an irregular slab of thickness "L". As mentioned before, this equation cannot be solved generally and one has to use different approximations for different applications. The simplest case is when the normal incidence is assumed. Usually a complex amplitude is assumed for the wave field, such as:

$$\vec{E} = u(\vec{r})exp(-jkz) \tag{4.28}$$

Substituting equation (4.28) in equation (4.11) yields :

$$-2jk\frac{\partial u}{\partial z} + \nabla^2 u = -k^2\epsilon_1(\vec{r})u \tag{4.29}$$

To solve this equation another assumption that z>>L>> λ is made [75, 74], where "z" is the height of irregularity, "L" is the characteristic scale size of the irregularity, and "λ" is the wavelength of the signal. This assumption indicates that $2k\left|\frac{\partial u}{\partial z}\right| >> \left|\frac{\partial u}{\partial z}\right|^2$ which results in the following equation:

$$-2jk\frac{\partial u}{\partial z} + \nabla_\perp^2 u = -k^2\epsilon_1(\vec{r})u, 0 < z < L \tag{4.30}$$

Here, $\nabla_\perp^2 = \partial^2/\partial^2 x + \partial^2/\partial^2 y$ so that this a parabolic type of equation whose solution is uniquely determined by taking the initial condition z=0, which indicates the point at which the wave enters the irregularity slab. Below the

irregularity slab, the complex amplitude satisfies the following equation:

$$-2jk\frac{\partial u}{\partial z} + \nabla_{\perp}^{2} u = 0, z > L \tag{4.31}$$

It should be noted that the initial condition for equation (4.31) is the solution from equation (4.30). These equations (4.30) and (4.31) are at the heart of all scintillation theories. Scintillation with a standard deviation of phase flucations less than one radian is defined as weak scintillation.

One of the most commonly used scintillation theories for weak scintillation is called Phase Screen Theory [74, 55, 75, 64]. This theory is quite well established and the predictions of this theory have been verified experimentally many times. In this dissertation, we are mainly interested in the Phase Screen Theory and its implications.

4.4.1 Phase Screen Theory

This theory is one of the first theories used to describe scintillation [55, 75]. It is based on the assumption that the ionosphere is a very thin screen which only changes the phase of the signal as the signal passes through it. As described earlier, this phase-distorted wave front undergoes constructive and destructive interference which results in scintillation.

To understand this phenomenon quantitatively, an incident wave with con-

stant amplitude A_0 is considered. This wave of constant amplitude A_0 passes through the screen/slab that is located at z=0. Upon emerging out of the slab, the wave takes the form:

$$u_0(\vec{\rho}) = A_0 exp[-j\phi(\vec{\rho})] \tag{4.32}$$

where, $\phi(\vec{\rho})$ is the phase of the signal and $\vec{\rho}$ is the transverse coordinate(x,y). The term $\phi(\vec{\rho})$ denotes the change of phase of the signal as it traverses through the screen. The change of phase can be obtained in terms of deviation of total electron content (N_T) using equation (4.18) :

$$\phi(\vec{\rho}) = k_0(\Delta\phi) = -\frac{e^2 k_0 \Delta N_T(\vec{\rho})}{2m_e\epsilon_0\omega^2} = -\frac{\lambda^2}{2\pi} r_e \Delta N_T(\vec{\rho}) \tag{4.33}$$

Here, r_e is the classical electron radius, and λ is the wavelength used. This phase-distorted wave, after emerging from the slab propagates towards the receiver on the ground. As a result of the phase differences, this wave will set up an interference pattern on the ground resulting in an amplitude fluctuation/scintillation. This field can be computed using Kirchhoff's diffraction formula under the forward scattering assumption which is given as :

$$u(\vec{\rho}, z) = \frac{jkA_0}{2\pi z} \int\int e^{-j[\phi(\vec{\rho}') + (k/z2)|\vec{\rho} - \vec{\rho}'|^2]} d^2\rho' \tag{4.34}$$

Equation (4.34) satisfies equation (4.31) which governs the wave propagating below the irregularity slab. To make it easy to relate theory and experimental

results, it would be better to find formulas to represent the experimentally observed values. To do this, the wave u($\vec{\rho}, z$) can be represented as :

$$u(\vec{\rho}, z) = A_0 exp[\chi(\vec{\rho}, z) - jS_1(\vec{\rho}, z)] = A_0 exp[\psi(\vec{\rho}, z)] \tag{4.35}$$

where $\chi(\rho, z)$ is referred to as the log-amplitude and $S_1(\vec{\rho}$,z) as the phase departure of the wave.

For weak scintillation, i.e., for $\phi_o^2 << 1$, using equation (4.34) and equation (4.35), $\chi(\rho, z)$ and $S_1(\rho, z)$ can be written as :

$$\chi(\vec{\rho}, z) = \frac{k}{2\pi z} \int \int_{-\infty}^{\infty} \phi(\vec{\rho}') cos[k|\vec{\rho} - \vec{\rho}'|^2/2z] d^2\rho' \tag{4.36}$$

$$S_1(\vec{\rho}, z) = \frac{k}{2\pi z} \int \int_{-\infty}^{\infty} \phi(\vec{\rho}') sin[k|\vec{\rho} - \vec{\rho}'|^2/2z] d^2\rho' \tag{4.37}$$

and from equations (4.36) and (4.37), the power spectra of the log-amplitude and the phase departure respectively are :

$$\Phi_\chi(\vec{k}_\perp) = 2\pi L \lambda^2 r_e^2 sin^2(k_\perp^2 z/2k) \Phi_{\Delta N}(\vec{k}_\perp, 0) \tag{4.38}$$

$$\Phi_S(\vec{k}_\perp) = 2\pi L \lambda^2 r_e^2 cos^2(k_\perp^2 z/2k) \Phi_{\Delta N}(\vec{k}_\perp, 0) \tag{4.39}$$

From observations reported in previous studies [41, 72], the ionospheric irregularity spectrum, $\Phi_{\Delta N}$, was observed to be of a power-law type which decays as wavenumber "k" increases. This indicates that, rather than one scale, a

range of different scales of irregularity contribute to scintillation. Note that the first maximum of equation (4.38) occurs when k$\cong \frac{2\pi}{d_F}$ where d_F is the Fresnel distance given by $\sqrt{2\lambda z}$. "z" is the distance between the screen and the receiver. This result indicates that for amplitude scintillation most of the contribution comes from irregularities that are about the Fresnel distance in size and any contribution from irregularities larger than the Fresnel size are filtered out. That is, for a signal with wavelength of ≈19 cm (GPS L1 signal), when the ionosphere is assumed to be about ≈350 km, the Fresnel length for L1 signal is about ≈350 m. This means that for the GPS L1 signal, only irregularities smaller than about 350m contribute to amplitude scintillation, while on the other hand irregularities, both smaller and larger than 350 m, contribute to phase fluctuations. The following schematic Figure 4.3 shows the expected power and phase spectra for a scintillating radio signal. It can be clearly seen that most of the contributions to the amplitude spectra come from frequencies above a certain frequency called the Fresnel frequency denoted by V_F. Furthermore amplitude spectra are filtered for frequencies below the Fresnel frequency unlike phase spectra, which have contributions from all sizes.

By definition, fluctuations that have frequencies higher than this Fresnel frequency are considered scintillation and so frequencies below the Fresnel frequency are removed/detrended before the data are used for scintillation studies. This Fresnel frequency is defined as [75, 19]:

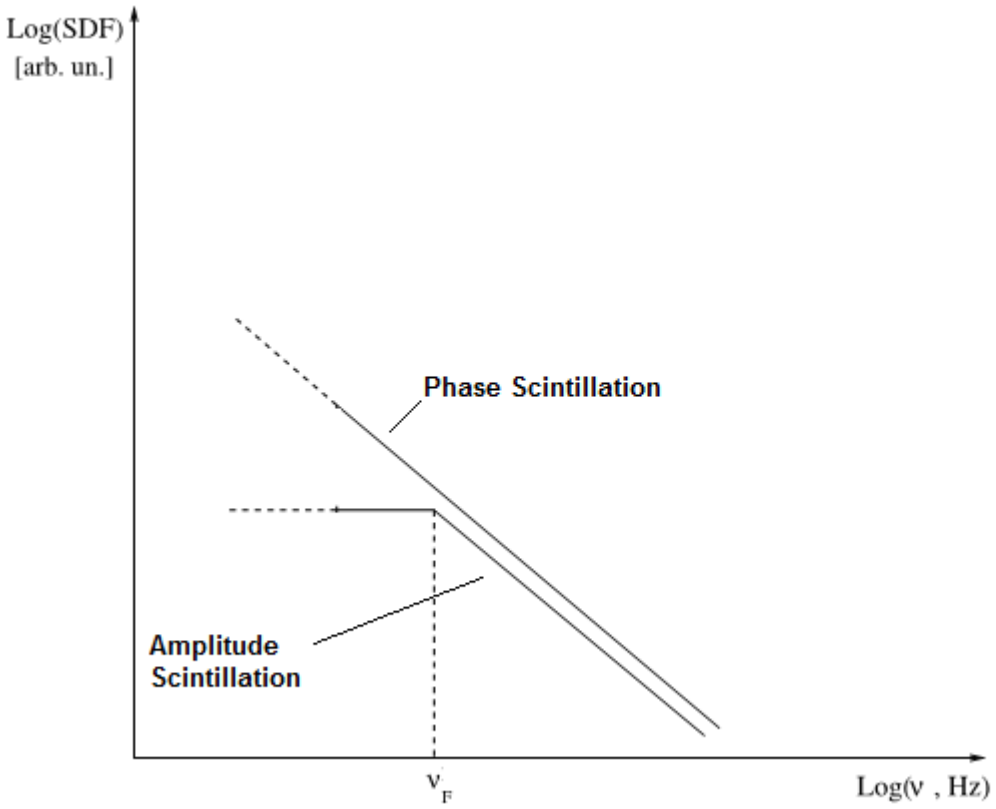

Figure 4.3: Illustrative representation of phase and amplitude power spectra asymptotic behavior in double lograthmic scale. V_F represents the Fresnel frequency [19].

$$V_F = \frac{V_{relative}}{\sqrt{2\lambda z}} \tag{4.40}$$

where $V_{relative}$ is the relative velocity between the ionosphere and the satellite, "λ" is the wavelength of the signal used, and "z" is the distance between the screen and the receiver. Thus it can be seen that scintillation is dependent on the ionospheric drift and the satellite trajectory and hence scintillation can vary with place and the satellite system that is being used to study scintillation. This should be taken into account while analyzing the scintillation data because the default methods used to analyze a particular data set from a particular satellite system should not be used to analyze scintillation data from a different satellite system or at a different place where the ionosphere can be totally different.

In conclusion, it should be noted that phase screen theory is one of the most commonly used theories to explain scintillation. This theory works only for weak scintillation. One has to invoke other scintillation theories if the scintillation is not in the weak scintillation regime.

4.4.2 Other Scintillation Theories

Phase screen theory assumes that only the phase of the signal is distorted as the signal passes through the ionosphere. This assumption holds for weak scintillation and can be considered as a very basic theory. To understand

the more complex nature of scintillation, there are other theories which have been developed. Examples of such theories are the weak scintillation theory using the Rytov approximation and the Parabolic Equation Method. In the Rytov approximation, along with the phase, the amplitude of the signal is assumed to be distorted as the signal passes through the irregularity slab. To include the effects of scattering into the scintillation theory, equation (4.35) should be substituted into equation (4.30) resulting in:

$$-2jk\frac{\partial\psi}{\partial z} + \nabla_{\perp}^{2}\psi + (\nabla_{\perp}\psi)^{2} = -k^{2}\epsilon_{1}(\vec{r}) \tag{4.41}$$

Assuming a weak scintillation regime $(\nabla_{\perp}\psi)^2$ can be assumed to be zero. This would lead to the equation for the Rytov solution [75] :

$$-2jk\frac{\partial\psi}{\partial z} + \nabla_{\perp}^{2}\psi = -k^{2}\epsilon_{1}(\vec{r}) \tag{4.42}$$

The Rytov solution for this equation (4.42) is :

$$\psi(\vec{\rho},z) = \frac{jk}{2\rho z}\int\int \psi_0(\vec{\rho'})exp[\frac{-jk\left|\vec{\rho}-\vec{\rho'}\right|^2}{2z}]d^2\rho' + \tag{4.43}$$
$$\frac{k^2}{4\pi}\int_0^z \frac{d\xi}{z-\xi}\int\int \epsilon_1(\vec{\rho'},\xi).exp[\frac{-jk\left|\vec{\rho}-\vec{\rho'}\right|^2}{2(z-\xi)}]d^2\rho'$$

This equation includes fluctuations of both amplitude and phase and can be used to obtain the field equation as soon as the wave leaves the irregularity

layer. This field equation can then be used as the initial condition for equation (4.31), and would give information about the field at the ground. More details about these derivations can be found at [75].

If the ionospheric irregularity spectrum is of the form $k_{\perp}^{p}$ then the general behavior of the spectral slopes of amplitude and phase scintillation can be estimated using the Weak scintillation theory-Rytov approximation. That is, in this approximation of the scintillation theory, it is speculated that the resultant slope for the scintillation signal's amplitude is (1-p) for frequencies above the Fresnel frequency and flattens out below the Fresnel frequency. In contrast, the spectral slope for the phase does not flatten out after the Fresnel frequency but has a constant value of (1-p). Hence, even in Rytov approximation, the spectra of the amplitude and phase follow the same form as the spectra obtained using phase screen theory where amplitude spectra is Fresnel-filtered and most of the contribution to the amplitude scintillation comes from spatial frequncies in the vicinity of the Fresnel scales, whereas the phase spectra has contributions from all scales. Another important result from the Rytov approximation is that it gives the relation between the irregularity spectrum and the spectrum of phase and amplitude of the signal. In cases where ϵ_1 is assumed to be very high, multiple scattering of the wave occurs inside the irregularity slab. This results in fluctuations in the phase which are much greater than 1 rad. This type of scintillation is severe and it is not in the weak scintillation regime as $S_4 < 0.4$ for all observed events in

this dissertation. In this case, weak scintillation theories do not work and so strong scintillation theories, like the parabolic equation method, should be invoked. The scintillation events encountered in this study are all under the weak scintillation regime as $S_4 < 0.4$ and $\sigma_\phi < 1$, hence only phase screen theory was considered. A good description of the other theories can be found at [74, 54, 75].

4.5 GPS Scintillation

The Global Positioning System uses L-band frequencies as its main carrier signals [72]. These legacy carrier signals (L1= 1575 MHz, L2= 1227 MHz) are prone to scintillation and hence can be used to study scintillation effects. L1 is usually preferred over L2 for scintillation studies mainly because the L2 signal has less power and a lower frequency than L1. Hence the probability of L2 getting attenuated before L1 is greater. Given GPS's extensive spatial and temporal availability compared to other conventional methods, the study of scintillation using GPS has given a new impetus to scintillation research. Given the importance of GPS in scientific, industrial and defence applications, one needs to understand the error introduced in the signal due to scintillation and try to predict and mitigate it [24].

Until recently, most of the GPS scintillation studies were confined to the mid and low latitudes. In the last few years, there has been an increased interest

in high latitude GPS scintillations with the increase in GPS receiver networks such as the Canadian High Arctic Ionospheric Network (CHAIN) [31]. It should be noted that normal GPS receivers used for navigation cannot be used to study scintillation. Instead one needs custom-made GPS receivers with low receiver noise so that the phase scintillation signal is not flooded out by noise. This low receiver noise can be achieved through the use of custom-made low phase noise oscillators in the receivers [15].

In order to analyze scintillation, one has to quantify it using scintillation indices. The most commonly used scintillation indices employed in GPS scintillation research are S_4 and σ_ϕ [55, 19, 17]. S_4 is defined as the normalized standard deviation of the detrended power (P) of the signal :

$$S_4 = \sqrt{\frac{\langle P^2 \rangle - (\langle P \rangle)^2}{\langle P^2 \rangle}} \tag{4.44}$$

while σ_ϕ is defined as the standard deviation of the detrended phase (ϕ) of the received signal :

$$\sigma_\phi = \sqrt{\langle \phi^2 \rangle - \langle \phi \rangle^2} \tag{4.45}$$

Here $\langle\rangle$ indicate a one-minute average of the detrended amplitude/phase. It should be noted that there is no steadfast rule that one has to use a one-minute average to calculate these indices. A one-minute average is generally used because it is usually assumed that scintillation signals are sta-

tionary (i.e., the statistical properties of the signal do not change) during one minute [15]. Some receivers provide indices, usually σ_ϕ, for averages over less than one-minute averages. Scintillation indices are very important because of their use in modeling and predicting scintillation [65]. Thus their accuracy is of utmost importance.

From previous scintillation studies involving the Wide-Band Satellite system, it was observed that 0.1 Hz would be the best most suitable cut-off frequency to detrend the Wide-Band Satellite system signals at mid- and low-latitudes [21, 19]. This default 0.1 Hz cut-off frequency was also used to detrend GPS signals since most of the initial work that was done in the field of GPS scintillation was mainly from mid- and low-latitude regions [72]. 0.1 Hz is a good approximation of the Fresnel frequency at mid- and low-latitudes. Recent studies [19, 17, 72, 64] have shown that at high latitudes the scenario is totally different since the ionosphere is more active. As shown in Figure 4.4 the Fresnel frequency at high latitudes (V_F^{HIGH}) is much higher than the Fresnel frequency at low latitudes (V_F^{LOW}) which is approximately 0.1 Hz [19].

Using the default 0.1 Hz cutoff frequency introduces unwanted contributions into the phase and power measurements for high latitude analysis. As shown in Figure 4.4, with red color, the unwanted contribution would be more in the phase measurements than in the amplitude measurements. This can lead to inaccurate results known as "phase without amplitude scintillation".

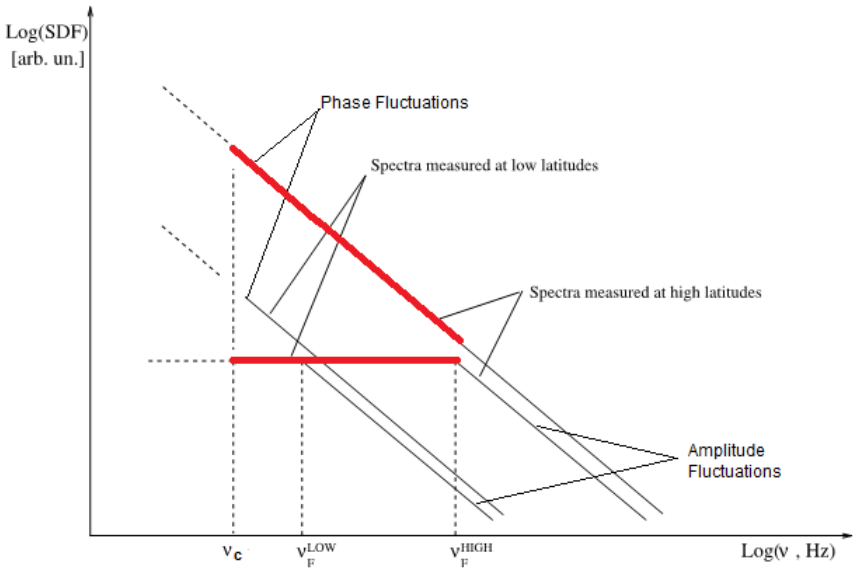

Figure 4.4: Illustrative representation of phase and amplitude power spectra asymptotical behavior at high latitudes. V_C, V_F^{LOW}, V_F^{HIGH} are the default cut-off frequency, Fresnel frequencies at low and high latitudes respectively. [19].

That is, as the name suggests, high phase scintillations can be observed for corresponding low amplitude scintillation at high latitudes. These artifacts may lead to errors when the scintillation indices are used in implementing scintillation models or when trying to use these indices to study the ionospheric irregularities [19]. Recent studies [19, 10] have also questioned the validity of σ_ϕ as the phase scintillation index for GPS scintillation studies mainly because of "the dominance of low frequency component of the phase power spectrum in its makeup" [10]. All this points to the fact that a better detrending filter should be designed that can mitigate these errors.

Another important source of error is the use of the time-invariant Butterworth filter in detrending the GPS signals [72]. Since GPS signals are Doppler shifted, the frequency of the received signals is changing in time, i.e., they are non-stationary signals. Time-invariant Butterworth filters are not designed for non-stationary signals and cannot filter these signals accurately. Thus, there is a need for a better detrending filter that would provide more accurate results. In recent years a new method of using wavelet transforms to study non-stationary signals is gaining acceptance [44, 47]. The main advantage of using this method is it gives information on both the frequency and time of a signal. Chapter 5 will introduce this technique and, explain how this technique was used in this study.

Chapter 5

Wavelet Analysis

5.1 Introduction

The data obtained from scintillation receivers are usually saved as a time series of the signal. To better understand the GPS scintillation signal features as well as to develop detrending filters, information regarding the frequencies involved in the signal is necessary [15]. A common technique used to obtain frequency information of the signal, is to convert the time series into the frequency domain by using the Fourier transform. The following section briefly introduces the Fourier transform and reveals its disadvantages when dealing with signals like those of GPS [72].

5.2 Fourier Transform

The Fourier transform is perhaps the best known method to obtain the frequency information of a signal. It is named after the French physicist and mathematician, Joseph Fourier, who pioneered the work of the Fourier series, which formed the framework for the Fourier transform [34]. The Fourier transform of a time series, G(t), is given by

$$G(f) = \int_{-\infty}^{\infty} G(t) e^{-2j\pi ft}\, dt \tag{5.1}$$

Here, G(f) represents the frequency information of the time series G(t). The main concept of the Fourier transform is derived from the concepts of the Fourier series where a time series signal can be represented by the sum of sines and cosines with different frequencies as shown in Figure 5.1 [46]. Sines and cosines are considered to be the basis functions in the Fourier transforms. Equation (5.1) represents the Fourier transform of a continuous signal with infinite duration. In practice, signals used in digital signal processing are discrete signals or signals that are sampled at a given frequency. These sampled signals usually represent a continuous signal within a finite interval.Let x_0, x_1,...,x_N represents such a signal x(t) which is sampled "n" times and let X be its Fourier transform. In order to compute the Fourier transform of such a signal, a discrete Fourier transform, equation (5.2), should be used.

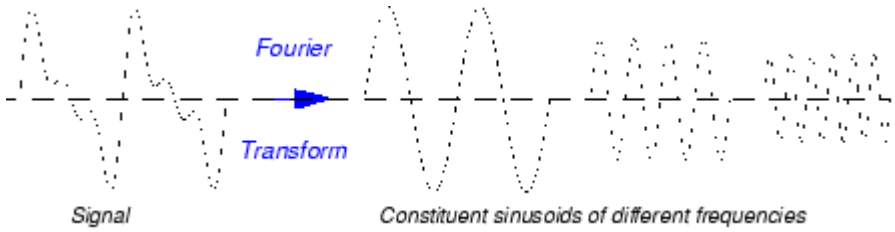

Figure 5.1: Example illustrating how a signal can be decomposed into sum of sines/cosines using Fourier transforms [46].

$$X_k = \sum_{n=0}^{N-1} x_n . e^{-j2\pi kn/N} \tag{5.2}$$

For the discrete Fourier transform to work properly, the finite time segment that is being analyzed should be at least one significant period in the infinite extended periodic signal. If this is not true, spectral leakage will arise due to the finite resolution of the discrete Fourier transform. Spectral leakage can be defined as an effect in the frequency analysis of finite length signals where it appears as if some energy were "leaked" out of the original spectrum into other nearby frequencies. This effect can be reduced by using a "window" function. The "window" function is defined as a mathematical function that is zero-valued outside a chosen interval. When a signal is multiplied with a window function, the product is zero valued outside the window interval and all that remains is where the signal and the window overlap. This is analogous to viewing the signal "through a window"and thus the name [34, 46].

Windowing also helps in obtaining time information on the frequencies in-

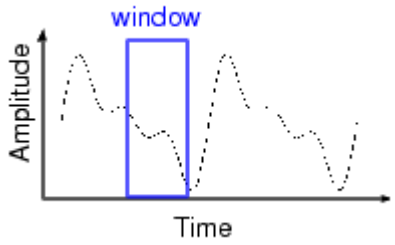

Figure 5.2: Illustration of windowing of a signal using a window of constant size [46].

volved in the signal. If a signal is Fourier transformed, information about all the frequencies that are in the signal is known but the time when of when particular frequency occurred is never known. Now consider using a window with a fixed temporal width and moving this window along the signal and calculating the Fourier transform along the way as shown in Figure 5.2. This would give us information on the temporal and frequency aspects of the signal. This method of analyzing the signal using a window is also called Short-Time Fourier Transform (STFT) [34, 46]. Although this concept of windowing is useful, it has some inherent disadvantages due to the constant size of the window. As a result of this, there is a lack of time resolution at low frequencies and lack of frequency resolution at higher frequencies. Thus there is a need for implementing a window that changes its width with frequency. Wavelets are exactly such an analysis tool: they use windows that change their width with frequency. Wavelet analysis also helps in obtaining information about localized features in frequency and time.

5.3 Wavelet Transform

In recent years, the wavelet transform has gained in popularity and become one of the important signal analysis tools, especially for analyzing localized variations in power within a time series. The main advantage of this transform as compared to the Fourier transform is its capability to give precise information both in time and frequency. This enables one to determine the dominant frequencies in the time series as well as how these frequencies vary in time. Fourier transforms, when used to analyze non-stationary signals (signals whose frequency content changes with time), cannot give precise information about these signals as the Fourier basis functions are not localized and so temporal variations in the frequency content of a time series cannot be identified. In contrast, wavelets are best suited to analyze non-stationary signals given their localization in time and frequency. It should be noted that GPS signals are non-stationary signals as these signals are affected by the Doppler shift between the satellite, ionosphere and receiver. Thus wavelets are a good tools to analyze these signals [16, 34, 46, 44].

The following sections give a brief introduction to wavelet transforms, their advantages and wavelet techniques that can be used to analyze GPS scintillation signals. Only the relevant wavelet properties and wavelet techniques used in this thesis are discussed. Describing all the wavelets and their properties as well as other popular wavelet techniques, like discrete wavelet trans-

forms is not within the scope of this dissertation.

5.3.1 Wavelets

Wavelets can be defined as mathematical functions that satisfy certain requirements. If ψ is a function, then the main requirement for ψ to be a wavelet function is that it has to satisfy: [16, 44]

$$\int_{-\infty}^{\infty} \psi(t)\, dt = 0 \tag{5.3}$$

This condition, equation (5.3), states that the mean of the signal should be zero or, in other words, the function should be "waving" on either side of the x axis and suggesting the name wavelets. Wavelets should be localized in frequency as well as in time. One important requirement for a function to be a wavelet is that it should have at least one reconstruction formula. There are many kinds of wavelets and the best wavelet to use depends on the application. The chosen wavelet is called the "mother" wavelet. In a continuous wavelet transform, the shifted and stretched/compressed wavelet is compared with the signal. This stretching or compressing of a wavelet function is collectively called scaling and corresponds to a physical variable called scale. This scale decomposition should be obtained only by shifting and stretching/compressing the "mother" wavelet. Therefore all "child" wavelets should be mutually similar. The concept of scales is essential in order to understand wavelets [34, 46].

As indicated, the output from the wavelet transform is represented in scales and time. These scales can be considered as a pseudo-frequency. With respect to Fourier frequencies, there is a general relation between wavelet scales and Fourier frequencies. Since wavelets with large scales are stretched out wavelets, they would give information about coarser signal features, while wavelets with smaller scales give information about the finer details of the signal. In general, it can be said that larger scales represent lower frequencies and smaller scales represent higher frequencies. Although there is a general relation, there is no precise relation between Fourier frequencies and wavelet scales. Empirical formulas have been derived for different mother wavelets in order to relate the scales to Fourier frequencies [34, 46, 44].

Time-scale representation of data is a natural way to view data from many natural phenomena including GPS scintillation. To better understand the concept of scaling and shifting, consider a "mother" wavelet as shown in Figure 5.3. This wavelet is called Daubechies 8 mother "wavelet". Now as shown in Figure 5.4, the mother wavelet is compared and correlated with the input signal by shifting the "mother" wavelet with a certain scale along the signal and then this process is repeated for other scales.

Mathematically, for a mother wavelet $\psi(t)$, this stretching/compressing and

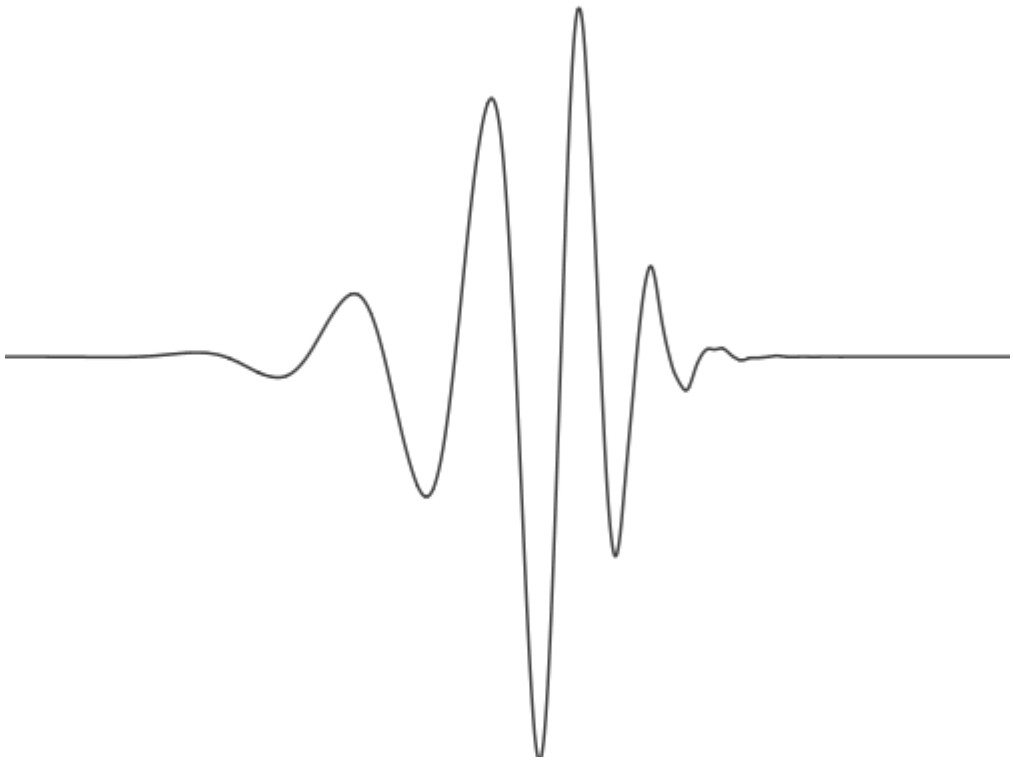

Figure 5.3: Figure depicting the shape of Daubechies 8, which is an example of a mother wavelet [46].

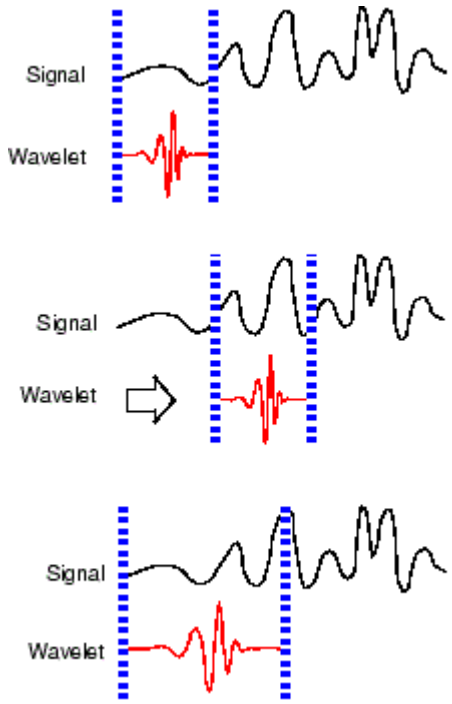

Figure 5.4: An illustration of shifting and scaling a mother wavelet in order to calculate the wavelet transform [46].

shifting can be represented as :

$$\psi_{a,b}(t) = \frac{1}{\sqrt{a}}\psi(\frac{t-b}{a}) \tag{5.4}$$

where "a" represents how much a mother wavelet is scaled while "b" represents the factor by which the mother wavelet is shifted. This scaled and shifted wavelet is then correlated with the signal (f(t)) to obtain the wavelet transform :

$$F(a,b) = \int_{-\infty}^{\infty} f(t)\frac{1}{\sqrt{a}}\psi^*(\frac{t-b}{a}) \tag{5.5}$$

Here F(a,b) represents the wavelet transform coefficients for a certain scale "a" for the whole signal, which is continuous. Typically however, the signals that are dealt with in signal analysis are not continuous but discrete. For practical applications, an understanding of how to treat a discrete signal using the continuous wavelet transform must be developed.

5.3.2 Continuous Wavelet Transform of a Discrete Signal

Any signal that is processed on a computer would be discrete. Let x_0,x_1,..,x_n,..,x_N be such a discrete signal with N elements with equal time spacing δt. The continuous wavelet transform of that series is

$$W(s) = \sum_{n'=0}^{N-1} x_{n'} \psi^* \left[\frac{(n' - n)\delta t}{s} \right] \tag{5.6}$$

Here ψ^* indicates the complex conjugate of ψ. In order to implement equation (5.6), "N" convolutions are required for every scale. This would take extensive computer resources as well as time if the signal is of high resolution in time. In order to make this operation much more efficient, these convolutions are usually computed in Fourier space using discrete Fourier transforms. This can be achieved because of the fact that the convolution of two sequences that are is the product of the Fourier transforms of those two sequences. Using this, the continuous wavelet transform of a discrete signal x_n is

$$W(s) = \sum_{k=0}^{N-1} \hat{X}_k \hat{\psi}^*(s\omega_k) e^{j\omega_k n \delta t} \tag{5.7}$$

Where $\hat{X}_k$ is the discrete Fourier transform of the discrete signal x_n, and the Fourier transform of the function $\psi(\mathrm{t/s})$ is given by $\hat{\psi}^*$, and the angular frequency ω_k is defined as

$$\omega_k = \frac{2\pi k}{N\delta t} : k \leq \frac{N}{2}$$
$$\omega_k = -\frac{2\pi k}{N\delta t} : k > \frac{N}{2}$$

Now the question arises about what exactly is "continuous" in this continuous wavelet transform of a discrete signal. The two things that are continuous in

this transform are scales and shifting. Depending on the computer's capabilities, one can use any number of scales up to a maximum user-defined scale. In addition, wavelets can be shifted continuously over the whole domain of the signal. In this work, scales as fractional powers of two were used:

$$s_q = s_0 \times 2^{q\delta q} \tag{5.8}$$

$$Q = \delta q^{-1} log_2(N\delta t/s_0) \tag{5.9}$$

Here, s_0 is the smallest resolvable scale, while Q determines the largest scale. s_0 was chosen to be 2δt, where δt is 0.02 sec (50 Hz signal) and δq, which represents the resolution in scale, was taken to be 0.125. It should be noted here that scales can be fractional powers of numbers other than "2", but "2" is usually the preferred value for computer programming [44].

5.4 Mother Wavelet

In the previous sections, the tools required to calculate the wavelet transform for a given discrete signal are formulated. The next step is to choose the right "mother" wavelet to do the analysis. Examples of such mother wavelets are shown in Figure 5.5.

Morlet and Paul wavelets (Figure 5.5a and Figure 5.5b) are examples of com-

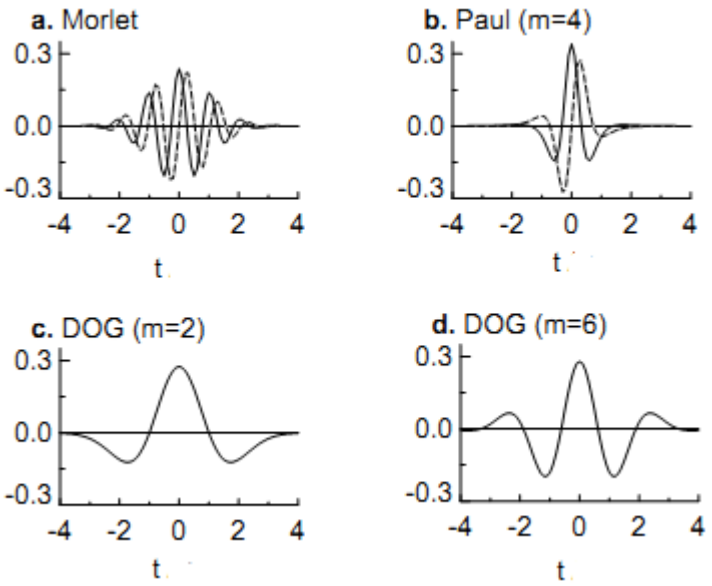

Figure 5.5: Depiction of four different mother wavelets namely (a) Morlet, (b) Paul, (c) Mexican hat, and (d) DOG. Here m represents the number of vanishing moments and the solid line shows the real part while the dashed line shows the imaginary part of the signal [67].

plex valued wavelets. The dashed line shows the imaginary part, while the solid line represents the real part. There is a $\pi/2$ phase shift between the real and imaginary part. The other two wavelets (Figure 5.5c and Figure 5.5d), which are derivatives of Gaussian (DOG) wavelets, are real valued wavelets. DOG (m=2) is also called the Mexican hat wavelet. Here "m" represents the number of vanishing moments or the number of times the signal value becomes zero. Many other "mother" wavelets that are available are Haar, Daubechies etc.

To get the optimum result one has to choose the best analyzing "mother wavelet" for the particular type of signal being worked on. The choice of the "mother" wavelet depends on many things. If the aim of the study is to analyze the oscillatory behavior of the signal, a complex wavelet should be used as it gives information of both amplitude and phase. Real valued wavelets are usually used to study discontinuities or to isolate peaks in the signal.

The width of the "mother" wavelet is also important as there should be a balance between the width in real space and the width in frequency space. A narrower width in time corresponds to a wider width in frequency, so this wavelet would result in a better time resolution but a poorer frequency resolution and vice versa. The shape of the "mother" wavelet is also important as the chosen shape should reflect the shape of the signal that is being

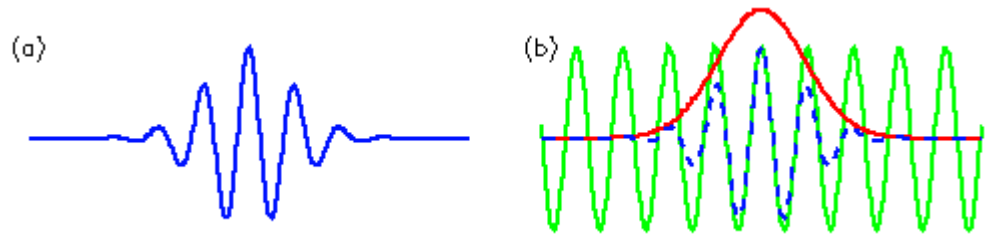

Figure 5.6: Construction of a Morlet wavelet is depicted here. (a) Figure representing a Morlet wavelet and (b) construction of a Morlet wavelet by combining a Gaussian curve and a sine wave [46].

analyzed [16, 34, 67].

5.4.1 Morlet Wavelet

The Morlet wavelet was named after Jean Morlet, a French geo-physicist, who originally formulated it in collaborations with Pierre Goupillaud and A. Grossmann [16]. The Morlet wavelet is shown in Figure 5.6a. This wavelet, Figure 5.6a, can be regarded as a sine wave with a certain frequency multiplied by a Gaussian envelope, as shown in Figure 5.6b.

This wavelet has the advantage of having a wave with a certain frequency but also being finite in its extent. This wavelet, because of its small time-bandwidth product, gives the best time and frequency resolution compared to other wavelets. Mathematically, the Morlet wavelet, ψ_0(t), is shown as [16]

$$\psi_0(t) = \pi^{0.25} e^{i\omega_0 t - \frac{1}{2}t^2} \tag{5.10}$$

where ω_0 is a non-dimensional frequency. An interesting fact about the Morlet wavelet is that it is only partially admissible as a wavelet as its mean is non-zero unless very small correction terms are added. In practice the value of ω_0 is taken to be 6. The need for correction terms does not exist for this value as these correction terms become very small and are usually on the order of typical computer round-off errors. The empirical formula which relates the Fourier wavelength and wavelets scale also depends on ω_0. It is given by

$$\lambda_{Fourier} = \frac{4\pi s}{\omega_0 + \sqrt{2 + \omega_0^2}} \tag{5.11}$$

Another important aspect regarding the Morlet wavelet function is that if it is considered to be a wave function, it denotes the minimum value of the product between time indetermination and scale indetermination. This indetermination is denoted by

$$\Delta t = \frac{l}{\sqrt{2}}, \Delta l = \frac{l}{\sqrt{2\omega_0}} \tag{5.12}$$

which means that for a scale of 1 sec there is an uncertainty of 0.7 sec in time and an uncertainty of 0.28 sec in scale. Taking all these aspects into consideration and the fact that the GPS scintillation signal has a wave-like structure with oscillatory behavior, the Morlet wavelet was chosen to be the mother wavelet to analyze GPS scintillation signals in this study. Another advantage of using the Morlet wavelet as the "mother" wavelet is the ease with which the signal can be reconstructed from wavelet coefficients [16, 46,

44, 67].

5.5 Wavelet Filtering

The most important advantage of the wavelet transform as compared to the Fourier transform is its ease of reconstruct the time-series signal using a different "mother" wavelet than the one used to analyze the signal. This wavelet used for reconstruction is called a synthesizing wavelet, while the one used to analyze the signal is called an analyzing wavelet. Jean Morlet has empirically developed a reconstruction formula (equation (5.13)) using the δ function as the synthesizing wavelet [16, 46, 44, 67].

$$x_n = \frac{\delta q \sqrt{\delta t}}{C_\delta \psi_0(0)} \sum_{q=0}^{Q} \frac{\Re \{W_n(s_q)\}}{\sqrt{s_q}} \tag{5.13}$$

This equation is merely the sum of the real part of the wavelet coefficients for all scales. Here $\psi_0(0)$ is used to remove energy scaling and $\sqrt{s_q}$ converts the wavelet transform to energy density. The constant C_δ comes from reconstructing the δ function using the analyzing wavelet ψ_0.

C_δ can be derived for any given wavelet in the following way. First a time series is considered with a δ function at time n=0, given by $x_n = \delta_{n0}$. The Fourier transform of such a series is $\hat{X_k} = N^{-1}$ and the wavelet coefficients of that signal can be obtained by substituting $\hat{X_k}$ in equation (5.7). This would result in

$$W_\delta(s) = \frac{1}{N} \sum_{k=0}^{N-1} \hat{\psi}^*(s\omega_k) \tag{5.14}$$

which in turn when substituted in equation (5.13) would give C_δ, (equation (5.15)) for that particular wavelet ψ_0.

$$C_\delta = \frac{\delta q \sqrt{\delta t}}{\psi_0(0)} \sum_{q=0}^{Q} \frac{\Re\{W_n(s_q)\}}{\sqrt{s_q}} \tag{5.15}$$

Equation (5.13) represents the reconstruction of the whole signal using all available scales. Sometimes, the whole signal need not be reconstructed as the interest may lie between two specific scales/frequencies, i.e., the signal has to be band-pass filtered. This can be achieved by modifying equation (5.13) to the form:

$$x_n = \frac{\delta q \sqrt{\delta t}}{C_\delta \psi_0(0)} \sum_{q=q_1}^{q_2} \frac{\Re\{W_n(s_q)\}}{\sqrt{s_q}} \tag{5.16}$$

where q_1 and q_2 represent the lower and upper cutoff scale values. These limits can be obtained both analytically as well as from observing scalograms. Scalograms are considered the best way to analyze wavelet transforms.

An example of such a scalogram for both amplitude and phase scintillation signals is shown in Figure 5.7. Here the X-axis represents time, while the Y-axis represents scale. The colour-coded Z-axis shows the relative wavelet power (ϵ(s,t)). This relative power, ϵ(s,t), is defined as the square modulus

of the wavelet coefficients ω(s,t):

$$\epsilon(s,t) = |\omega(s,t)|^2 \tag{5.17}$$

This scalogram (Figure 5.7) was obtained by analyzing a GPS scintillation signal using a Morlet wavelet as the mother wavelet. The scintillation signature, the region of relatively high power that is seen in most of the scales for a particular time, can be seen in this scalogram. This demonstrates that scalograms are very useful in analyzing how power density evolves in time and scale. Further more, as mentioned earlier, analyzing a wavelet transform of a signal with a scalogram helps the user to easily identify regions of interest which may need to be further analyzed by filtering out the unwanted regions/scales in the scalogram. This is a very important result as it can be used to detrend signals like the GPS scintillation signals. In Chapter 6, it will also be shown that the wavelet transform is a optimum method to analyze a non-stationary signal like the GPS scintillating signal. In addition to this, the advantages and implications of using the wavelet method of filtering over the default Butterworth filtering will be discussed [16, 46, 44, 67].

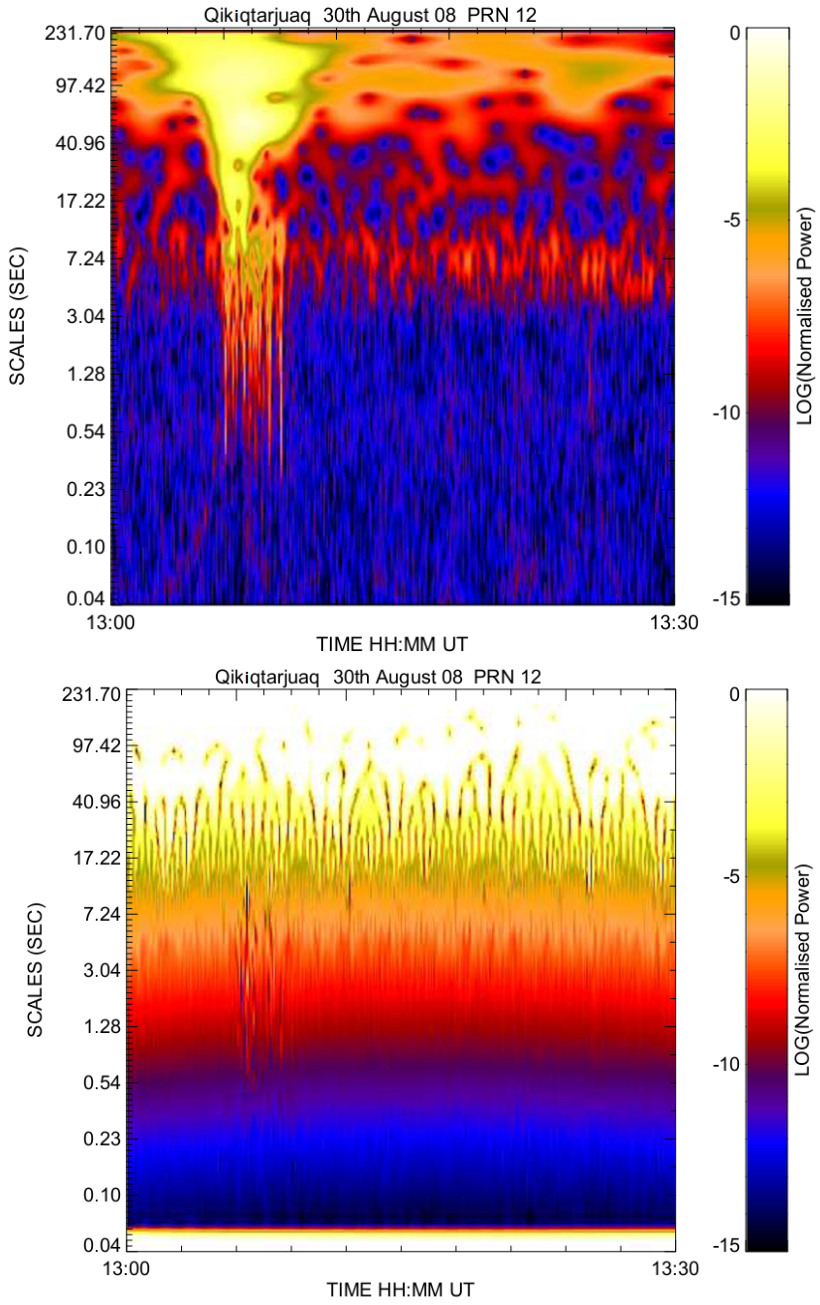

Figure 5.7: Scalogram of amplitude (top) and phase (bottom) of a scintillating GPS signal at Qikiqtarjuaq on 30 August 2008 on PRN 12 between 13:00 UT and 13:30 UT.

Chapter 6

CHAIN Scintillation Index

6.1 Canadian High Arctic Ionospheric Network (CHAIN)

The high latitude ionosphere is directly coupled to the solar wind and the inter-planetary magnetic field. A thorough knowledge of this complex coupled system requires an understanding of all the individual processes that are taking place in the system. This in turn requires a large quantity of observation data. Thus there is a need for a network of radio instruments to provide observational data that could be helpful in understanding the physical processes necessary for the fundamental understanding of the solar terrestrial coupling and its influence on our planetary environment. The Canadian High Arctic Ionospheric Network (CHAIN) is exactly such a network [31]. CHAIN is a distributed array of ten custom-made Global Positioning System

Ionospheric Scintillation and Total Electron Content Monitors (GISTM) [31]. These monitors are distributed from the auroral oval to the polar cap as shown in the Figure 6.1.

Along with these ten monitors, six Canadian Advanced Digital Ionosondes (CADIs) are co-located with the GPS receivers at Eureka, Resolute, Pond Inlet, Cambridge Bay, Hall Beach, and Iqaluit. Details of the CADI were discussed in Chapter 2. The main scientific objectives of CHAIN can be broadly classified as understanding of [31]:

1) Drivers and variabilities of polar cap convection.
2) Generation and dynamics of ionization structures in the polar cap; namely,
a) Macroscale - Structures greater than 1000 km in size, for example the tongue of ionization
b) Mesoscale - Structures, which are a few hundred kilometres in size, for example, polar patches.
c) Microscale - Structures, which are of few kilometres in size, for example, scintillation producing structures.
3) Improving handling and modeling ionospheric effects on Global Navigation Satellite Systems (GNSS).

Figure 6.1: Map showing geographical locations of Canadian High Arctic Ionospheric Network (CHAIN) GPS receivers.

6.1.1 GPS Ionospheric Scintillation and TEC Monitor

The main instrument used in the CHAIN network is the GISTM, also known as the GSV4004B. The GSV4004B uses a NovAtel GPS702 L1/L2 GPS antenna and a specifically modified NovAtel Europak-3M GPS receiver. The NovAtel Europak-3M GPS receiver can be considered the heart of the GISTM as it houses a low phase noise oven-controlled crystal oscillator. This is essential for obtaining reliable phase scintillation data because if the phase noise is more, it can flood out the phase scintillation signal. The GPS receiver can track up to 10 GPS signals simultaneously at the L1 (1575.42 MHz) and L2 (1227.6 MHz) and 3 satellite-based augmentation system (SBAS) geostationary satellites [15, 31].

GISTM's primary purpose is to compute and log total electron content (TEC) and scintillation parameters for up to 10 GPS satellites. TEC values are computed by combining L1, L2 pseudo-range and carrier phase measurements. These TEC values are logged at a resolution of 1 Hz along with azimuth and elevation of the satellite, which are logged at 4 Hz resolution. One thing to note here is that these TEC values are biased and the user has to determine the satellite and receiver bias to generate un-biased TEC values. The receiver can also log L1 raw power and raw phase at 50 Hz resolution for all satellites. These raw measurements alone cannot be used to study scintillation as they mainly include low frequency components mainly due to Doppler shift from the satellite motion. Hence, these raw measurements must be

detrended before scintillations can be observed clearly. GISTM uses a 6th-order Butterworth filter with a default cutoff frequency of 0.1 Hz to detrend the signals. This receiver-detrended power and phase data are then used to compute scintillation parameters S_4 and σ_ϕ. These parameters are computed for every minute. The receiver also has an option to log receiver-detrended phase and power at 50 Hz cadence.

6.2 Data Analysis

Recent studies [72, 44] have mentioned that for GPS scintillation signals, an invariant Butterworth filter, like the one used in the receivers, may not work satisfactorily while detrending signals that have their frequencies changing with time. These studies have suggested that to detrend non-stationary signals, a filter which is more localized in frequency and time, like the wavelet-based filter, should be used. Along with these sources, other studies [19, 10] have questioned the usage of σ_ϕ as the default phase scintillation index. The problems with σ_ϕ are manifold [10]. In Chapter 4, how the shift in scintillation spectra with change in ionospheric drift velocity effects σ_ϕ is discussed. It is observed that multipath, receiver phase noise, low phase fluctuations in the signal can also introduce additional variability in the σ_ϕ. In short, the problem with σ_ϕ is "primarily due to the dominance of the low-frequency component of the phase power spectrum in its make up" [10].

Thus a more precise detrending filter and a more accurate and robust phase scintillation index, especially in the high latitudes, are the need of the day. These are exactly what this thesis proposes to do. A new wavelet-based filtering method and a new phase scintillation index σ_{chain} are developed and are explored. Around 400 scintillation events were selected for this analysis from data obtained from the CHAIN network over the years 2009-2011. It should be noted that criteria for selecting the events were that whenever a scintillation ($S_4 > 0.1$) was observed in a particular hour, data from that whole hour were considered, so that both scintillation and non-scintillation data are analyzed. Data obtained from satellites below 30 degrees elevation angle were discarded from the analysis to reduce multipath effects. All the observed 400 scintillation events are in the weak scintillation category ($S_4 < 0.4$).

The raw power and phase data for these scintillation events were obtained from CHAIN receivers and then detrended by the wavelet filtering method (to be discussed in Section 6.2.1). This detrended data was then used to calculate scintillation indices (S_4, σ_ϕ, σ_{CHAIN}). The scintillation indices obtained from the receiver are called the Butterworth filter-derived scintillation indices as GISTM uses the Butterworth filter, while the scintillation indices derived from filtering the 50 Hz raw GPS power and phase signal using wavelet filtering are called wavelet-derived scintillation indices.

6.2.1 Comparison of Wavelet Filter and Receiver Butterworth Filter

As mentioned in Chapter 5, scalograms are the best way to analyze a wavelet transform of a signal as it helps to identify regions of interest in the signal spectrum. While perusing such scalograms of high latitude GPS scintillation events, it was observed that there is a three-band scale structure present in these scalograms. These bands as shown in Figure 6.2 are [44, 47]:

1. Trend/Large scale band: These large scales or low frequencies are mainly related to the satellite motion and the slowly changing ionosphere. Scales that are greater than ≈5 sec can be considered to represent this band. Most of the power resides in this band.

2. Scintillation band/mid-scale band: This band of scales is where most of the scintillation signatures were observed. Scales in the range of ≈0.09 sec to ≈5 sec are considered to be representing this band.

3. Noise/Small scale band: This band of scales, which are smaller than ≈0.09sec and are considered noise in the signal as these represent very high frequencies.

Recent studies [44] that used wavelet filtering to detrend the GPS signals, performed it by removing the large scale band or the low frequency part of the signal. In this study, the GPS scintillation signal is not only detrended by removing the large scale bands but also the signal is de-noised by remov-

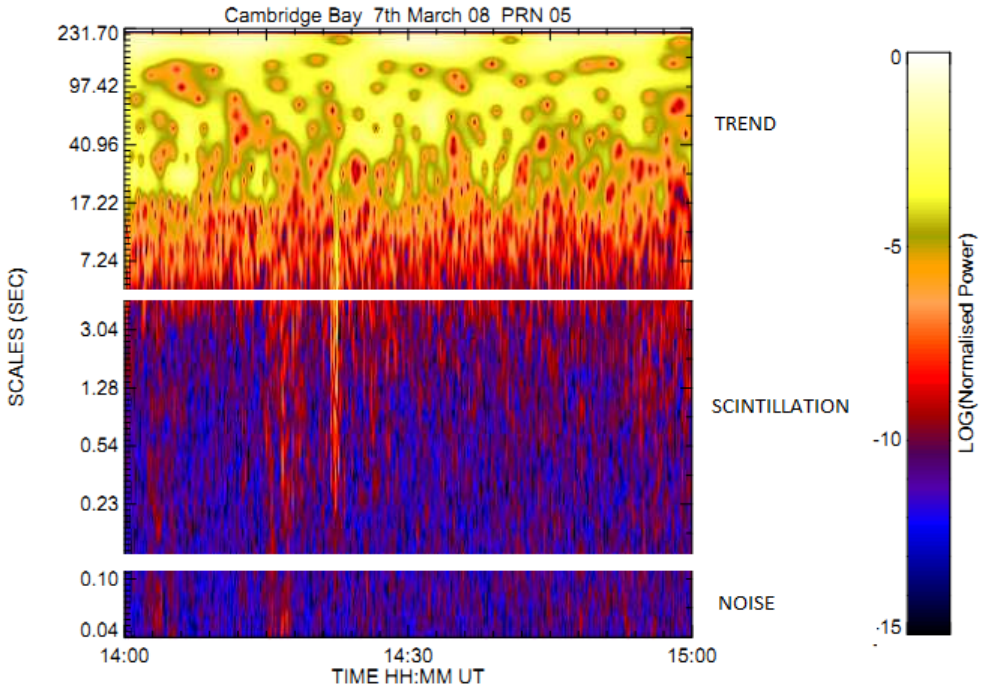

Figure 6.2: Scalogram of a scintillation event observed at Cambridge Bay (69.12^{o}N, 254.97^{o}E geog.). A three-band structure is also shown depicting the large scale band/trend, mid-scale band/scintillation and a low-scale band or noise.

ing the small scale band. The detrended signal is reconstructed from the wavelet coefficients using Equation 5.15. An important point to emphasize here is that one cannot differentiate between noise and scintillation at high frequencies. The approximate cut-off frequency used in this study is 10.7 Hz (scale=0.09 sec). For the ionosphere to induce fluctuations above 10.7 Hz in the GPS L1 signal, it should vary at a rate of 11 TECU/sec [39]. This rate of change of the ionosphere is very unlikely and hence it was decided that by using 10.7 Hz as the noise cut-off, only the high frequency noise was to be removed. These wavelet-detrended signals were then used to calculate the wavelet-derived S_4 and σ_ϕ. Examples of such an analysis are shown in Figures 6.3, 6.4 and 6.5.

These figures illustrate the comparison between the Butterworth filter used in the receiver and the wavelet detrending filter introduced in this work. These scintillation events were obtained from Cambridge Bay on 7 March 2008 on PRN 31 at 14:10-14:30 UT, Cambridge Bay on 20 December 2010 on PRN 22 at 00:10-00:40 UT and at PondInlet on 15 October 2010 on PRN 17 at 18:10-18:40 UT. In all three figures, panels (a) and (b) show the raw amplitude and phase respectively while panels (c) and (d) show the wavelet-transform of the raw amplitude and phase of the signal, respectively. The scintillation signature, the spike-like structure, in the wavelet transforms can be seen in both amplitude and phase wavelet transforms. Note that these signatures are much clearer in the amplitude scalogram than in the phase scalogram

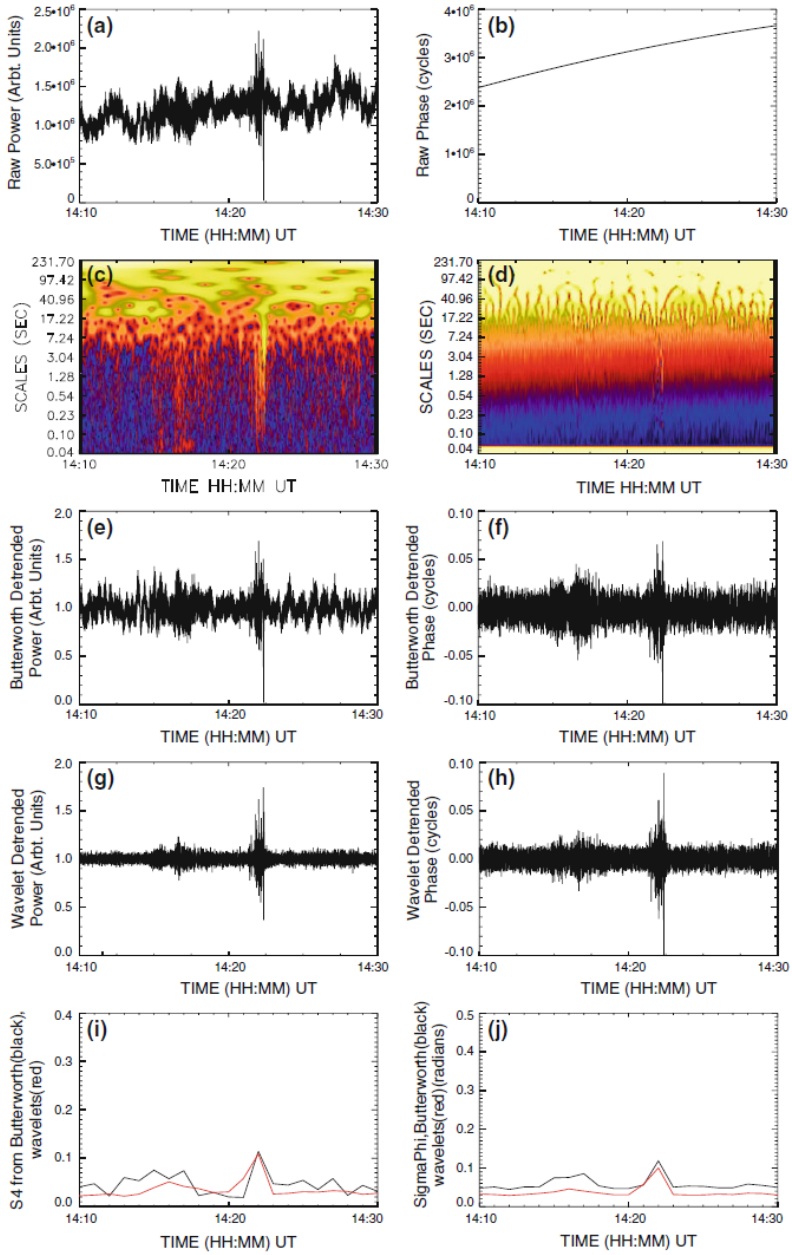

Figure 6.3: Comparison of detrending performance between Butterworth filter and wavelet filter for a scintillation event observed at Cambridge Bay (69.120^{o}N, 254.970^{o}E geog.) on 7 March 2008 on PRN 31 between 14:10 UT and 14:30 UT.

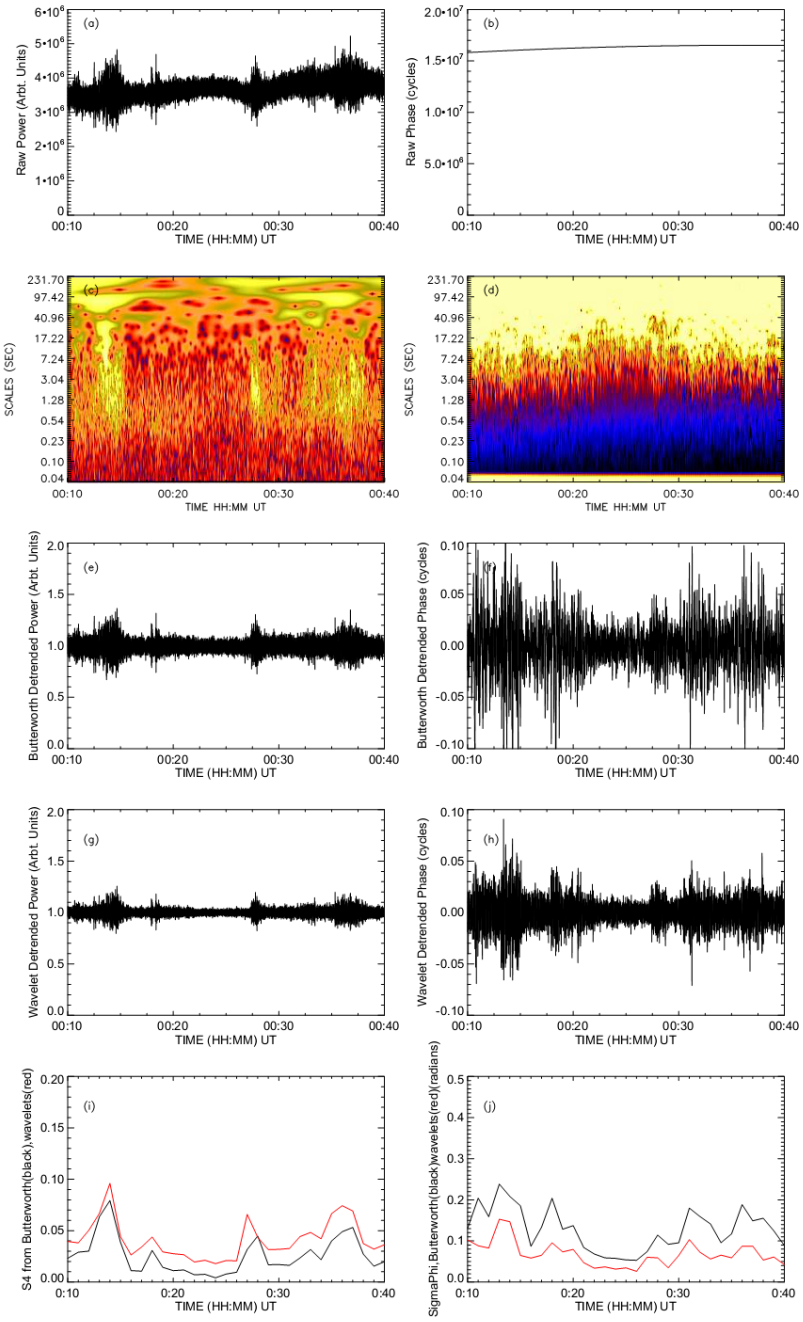

Figure 6.4: Comparison of detrending performance between Butterworth filter and wavelet filter for a scintillation event observed at Cambridge Bay (69.120^{o}N, 254.970^{o}E geog.) on 20 December 2010 on PRN 22 between 00:10 UT and 00:40 UT.

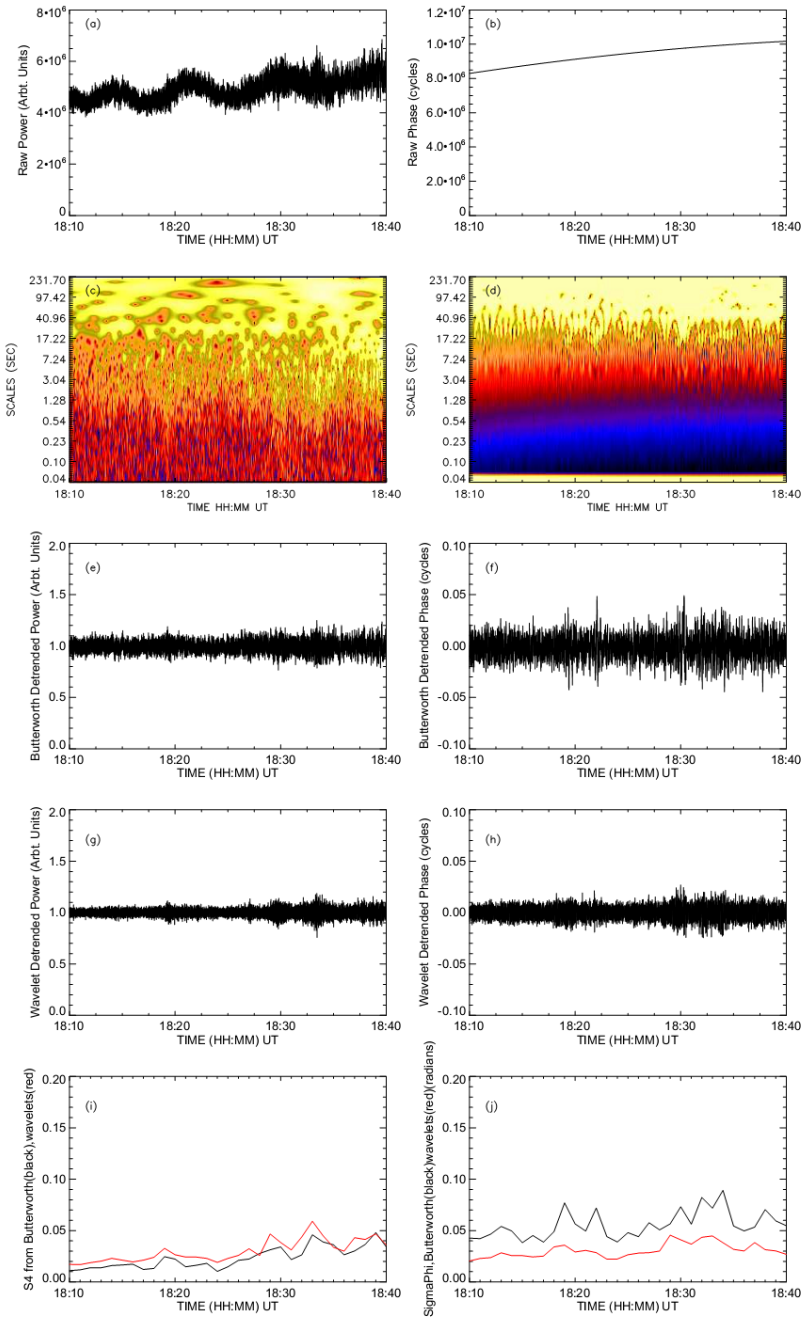

Figure 6.5: Comparison of detrending performance between Butterworth filter and wavelet filter for a scintillation event observed at Pond Inlet (72.69^{o}N, 282.040^{o}E geog.) on 15 October 2010 on PRN 17 between 18:10 UT and 18:40 UT.

because in the phase scalogram those signatures are small compared to the large power seen in the lower frequencies. In the amplitude scalograms, due to Fresnel filtering, lower frequencies are filtered out making the signatures easier to distinguish. Panels (e) and (f) represent the Butterworth-filtered power and phase respectively while panels (g) and (h) represent the wavelet-filtered power and phase respectively. Panels (i) and (j) represent scintillation indices S_4 and σ_ϕ respectively and these values are calculated from wavelet (red) and Butterworth (black) filtered power and phase respectively. From panel (e) it can be seen that the power signal is inadequately detrended by the Butterworth filter as there is still a small trending, wavy structure with non-constant mean, remaining in the signal (seen predominantly in Figure 6.3). This sometimes causes the Butterworth-detrended S_4 values, which are obtained from the receiver, to have high values of S_4 (seen around 14:28 UT in Figure 6.3i (black line) even though there is no scintillation). Panel (f) shows that the Butterworth-detrended phase usually looks noisy making it hard to distinguish it from scintillation. In contrast, in panels (g) and (h) the wavelet-detrended signals seem to have no apparent trend remaining in the signal and also the scintillation signatures are clearly visible. These scintillation signatures are well reproduced in wavelet-derived scintillation indices S_4 and σ_ϕ, shown as red lines in panels (i) and (j), where one can clearly distinguish the scintillations as well as their intensity.

These examples seem to indicate that the wavelet filtering method is a bet-

ter filter compared to the default Butterworth filter used in the receivers. In order to test this result more rigorously, all 400 scintillation events obtained from CHAIN sites were detrended using the wavelet filter and the corresponding scintillation indices (S_4 and σ_ϕ) were compared. Panel 6.6(a) shows the scatter plot between the Butterworth-derived S_4 and Butterworth-derived σ_ϕ obtained from the receiver (0.1 Hz cutoff frequency) for all 400 scintillation events considered in this evaluation. The "phase scintillation without amplitude scintillation" events which are represented by high phase scintillation values of $\sigma_\phi > 0.6$ for corresponding low S_4 values $S_4 < 0.1$ are clearly observed in panel 6.6(a). This result seem to validate the hypothesis that, as discussed in Chapter 4, high latitude GPS scintillation data can be prone to "phase scintillation without amplitude scintillation" when analyzed with the same techniques that are used to analyze mid- and low-latitude data. The hypothesis also states that at high latitudes, the "phase scintillation without amplitude scintillation" can be reduced if a higher cutoff value, closer to the Fresnel frequency, is used in the detrending filter [19, 17, 44].

While analyzing the scalograms of different scintillation events observed from the CHAIN, it was found that the large scale band usually starts below 0.193 Hz and thus this 0.193 Hz was used as the cutoff frequency for the Butterworth filter instead of 0.1 Hz to calculate S_4 and σ_ϕ. Panel 6.6(b) shows the scatter plot between the Butterworth-derived S_4 and Butterworth-derived σ_ϕ obtained from the same 400 scintillation events but with 0.193 Hz cutoff fre-

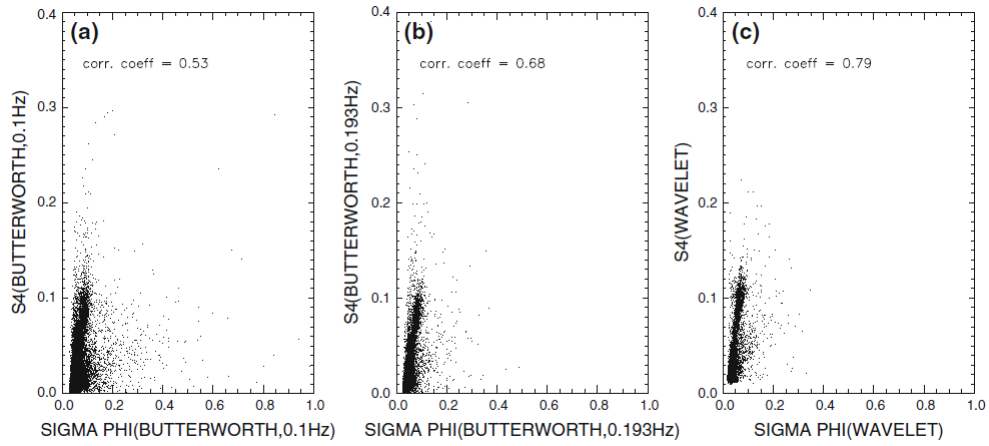

Figure 6.6: Correlation analysis between scintillation indices is plotted here. Panel (**a**) shows the scatter plot between S_4 and σ_ϕ values obtained from receivers using a Butterworth-detrending filter with 0.1 Hz cutoff frequency. Weak correlation was observed between the indices. Panel (**b**) shows the scatter plot for the same indices but computed with a Butterworth filter with 0.193 Hz cutoff frequency showing better correlation compared to panel (**a**). Panel (**c**) shows the scatter plot for indices computed from wavelet-detrended data showing a significantly high correlation value of 0.79. Around 400 scintillation events (one hour of data for each event) are considered in this plot.

quency. The "phase scintillation without amplitude scintillation" events have been significantly reduced in panel 6.6(b) as well as the correlation between the amplitude-scintillation index, S_4, and the phase-scintillation index(σ_ϕ), increased from 0.53 to 0.68, indicating that by using a better cutoff frequency in the Butterworth filter, these "phase scintillation without amplitude scintillation" events can be reduced but there is still a low correlation between S_4 and σ_ϕ.

Panel 6.6(c) shows the scatter plot between the wavelet-derived S_4 and wavelet-derived σ_ϕ from the same 400 scintillation events considered above. In panel 6.6c not only were the number of "phase scintillation without amplitude scintillation" events reduce significantly, but the correlation between the values of the amplitude-scintillation index, S_4, and the phase-scintillation index, σ_ϕ, was as high as 0.79. Studies [11] have shown that in a weak scintillation regime (S_4 <0.4), if the scintillation signal is detrended precisely, the phase scintillation index and the amplitude scintillation index should have a high correlation as the phase scintillation pattern should follow the pattern of amplitude scintillation above the Fresnel frequency. Thus, this improvement in correlation between amplitude-scintillation index and phase-scintillation index clearly indicates that at high latitudes the wavelet filter is superior to the time-invariant Butterworth filter present in the CHAIN GISTM receivers even when the cut-off frequency of the Butterworth filter is increased to take into account the shift in Fresnel frequency at high latitudes.

6.2.2 New Phase Scintillation Index (σ_{CHAIN})

As indicated before, in the place of σ_ϕ there is a need for a better and more robust phase scintillation index especially for high latitude GPS data. A recent study [17, 18] introduced a phase-scintillation index, σ_s, which takes into account the rate of change of phase, is considered independent of the cutoff frequencies and was shown to be a better index than σ_ϕ. In this study, this scintillation index (σ_s) is called Forte's scintillation index (σ_{Forte}) after

its inventor and is given by :

$$\sigma_{Forte} = \sqrt{\left\langle (\frac{\partial \phi}{\partial t})^2 \right\rangle} \tag{6.1}$$

The symbol ϕ is the detrended phase of the L1 signal that is computed every 0.02 s and $\langle\rangle$ denotes a one-minute average. Figures 6.7 and 6.8 show examples of σ_{Forte} observed during scintillation events as well as non-scintillation events. In Figure 6.7, during the active period of the ionosphere (right column), one can see three intervals of stronger scintillations in the detrended phase at 6:20 UT, 6:30 UT, and 6:40 UT. If those three intervals of stronger scintillation are ordered according to their scale of intensity, it can be observed that the scintillation at 6:40 UT is the most intense followed by the scintillation at 6:20 UT and 6:30 UT. Similarly in Figure 6.8, scintillation at 00:40 UT is stronger than 00:45 UT. When observing σ_{Forte} values for the active period of the ionosphere, it is observed that all three scintillation signatures have very similar values and it is hard to distinguish between them with respect to their scale of intensity. It can also be observed that the value of σ_{Forte} is similar for both quiet and active periods of the ionosphere.

In this study, a new scintillation index for wavelet-detrended high latitude GPS data called the CHAIN phase-scintillation index (σ_{CHAIN}) is introduced. This $\sigma_{CHAIN}$is defined as:

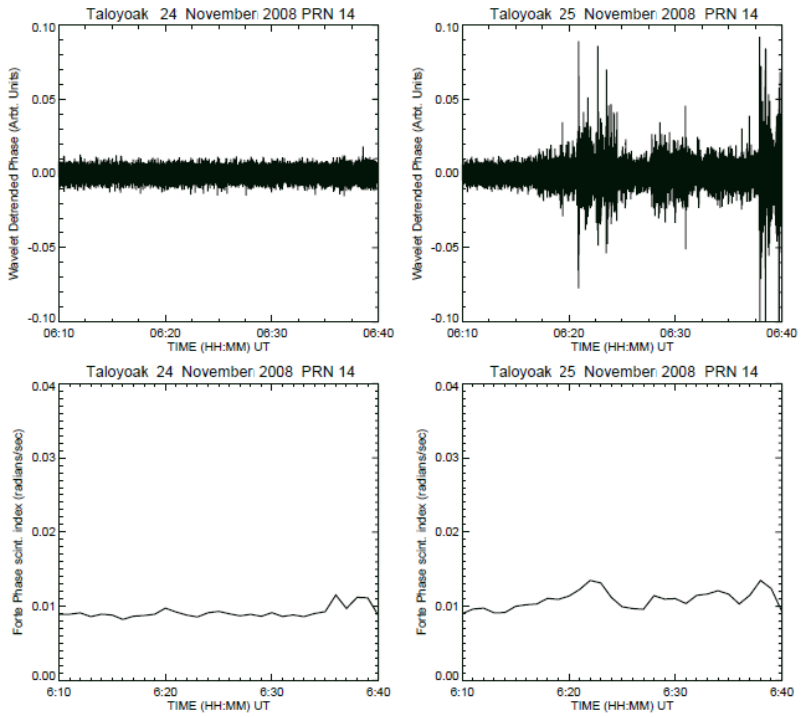

Figure 6.7: Performance of σ_{Forte} during scintillation and non-scintillation events. Detrended phase and the corresponding σ_{Forte} is shown for both quiet (left column) and active (right column) ionospheric periods as observed at Taloyoak (69.540^{o}N, 266.440^{o}E, geog.) on 24 November 2008 and 25 November 2008, respectively, for PRN 14 between 6:10 UT and 6:40 UT on both days.

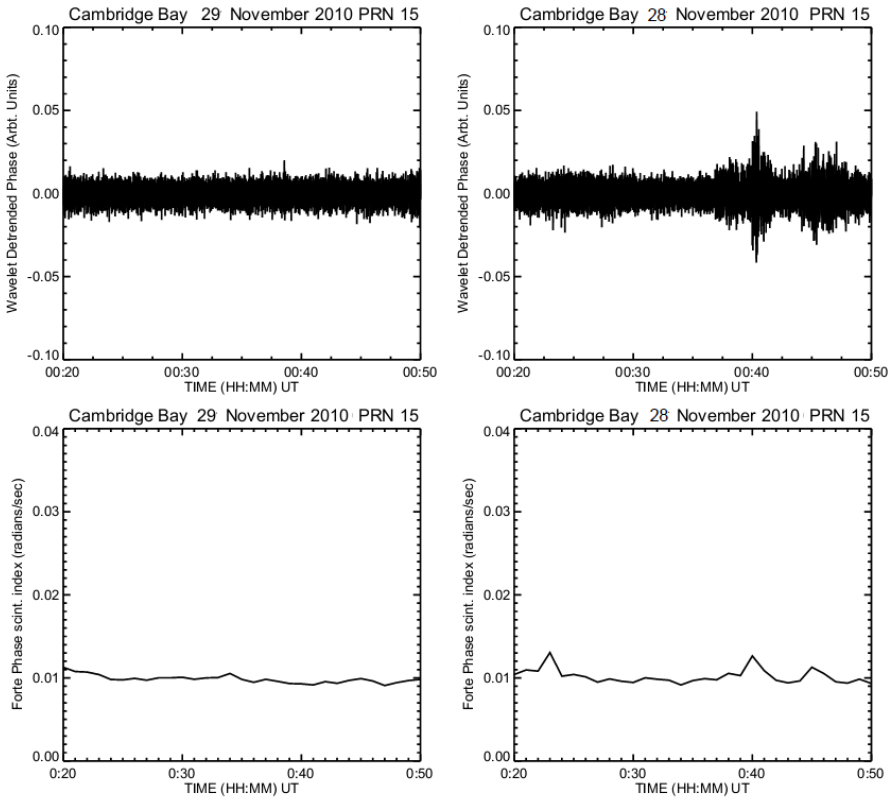

Figure 6.8: Performance of σ_{Forte} during scintillation and non-scintillation events. Detrended phase and the corresponding σ_{Forte} is shown for both quiet (left column) and active (right column) ionospheric periods as observed at Cambridge Bay (69.120^{o}N, 254.970^{o}E geog.) on 29 November 2008 and 28 November 2008, respectively, for PRN 15 between 00:20 UT and 00:50 UT on both days.

$$\sigma_{CHAIN} = \sqrt{\left\langle (\frac{\partial \phi}{\partial t})^2 \, |\phi| \right\rangle} \tag{6.2}$$

σ_{CHAIN} is a modification of this scintillation index, taking into account not only the rate of change of phase fluctuations but also how large the fluctuations are. This is achieved by introducing a phase-amplitude term ($|\phi|$) into the equation. This amplitude term is receiver-dependent, uncalibrated, and can be affected by detrended-induced smoothing. However since the only interest in this term lies in how large the fluctuations are with respect to the mean value of the detrended phase, this value ($|\phi|$) can be considered independent of receiver, calibration and detrending.

The advantage of having the phase-amplitude term ($|\phi|$) in σ_{CHAIN} can be clearly seen in Figures 6.9 and 6.10, which compare the phase scintillation indices σ_{Forte} and σ_{CHAIN} for the same events shown in Figures 6.7 and 6.8. The lack of clarity which was observed in σ_{Forte} is reduced by using σ_{CHAIN} since one can see three distinct scintillation signatures clearly indicating different levels of scintillation. These examples demonstrate that σ_{CHAIN} may be a more useful phase-scintillation index than σ_{Forte}.

6.2.3 Comparison of Performance Between σ_ϕ and σ_{CHAIN}

The next obvious step was to compare the performance of the default phase-scintillation index σ_ϕ and the CHAIN phase-scintillation index, σ_{CHAIN}. Ex-

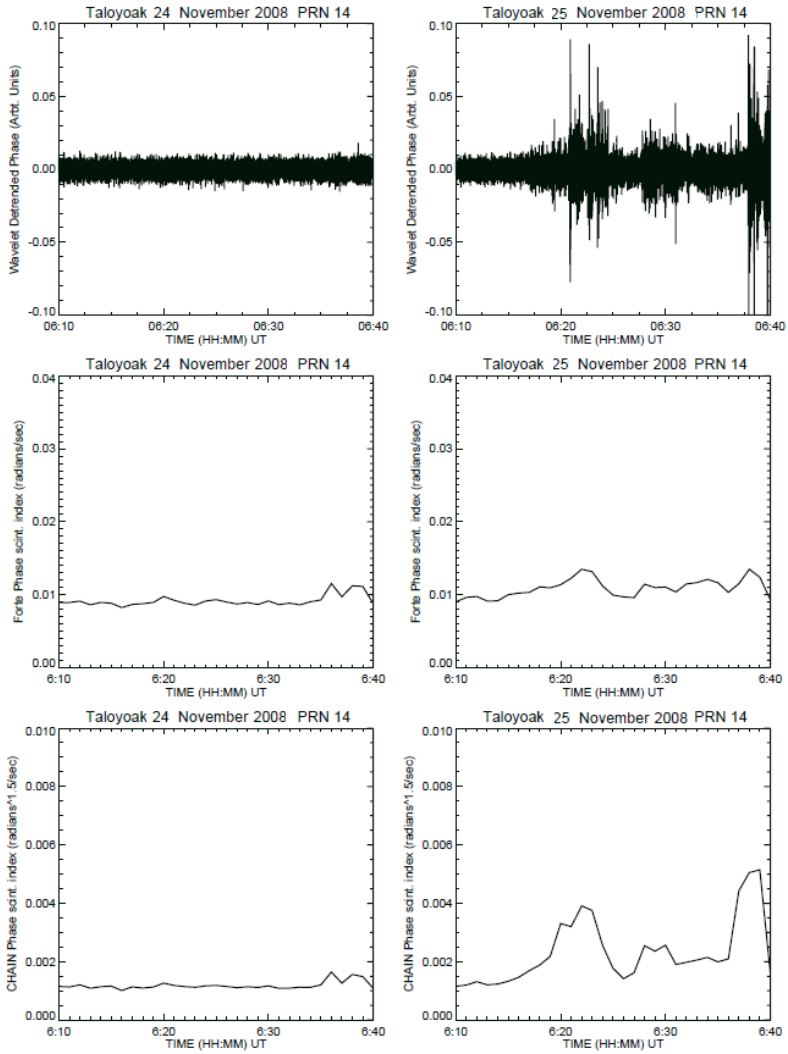

Figure 6.9: Comparing the performance between σ_{Forte} and σ_{CHAIN}. Detrended phase and the corresponding σ_{Forte} and σ_{CHAIN} values are shown for both quiet (left column) and active (right column) ionospheric periods as observed at Taloyoak (69.540°N, 266.440°E, geog.) on 24 November 2008 and 25 November 2008, respectively, for PRN 14 between 6:10 UT and 6:40 UT on both days. σ_{Forte} is not able to give as accurate a measure of the scintillation compared to σ_{CHAIN}.

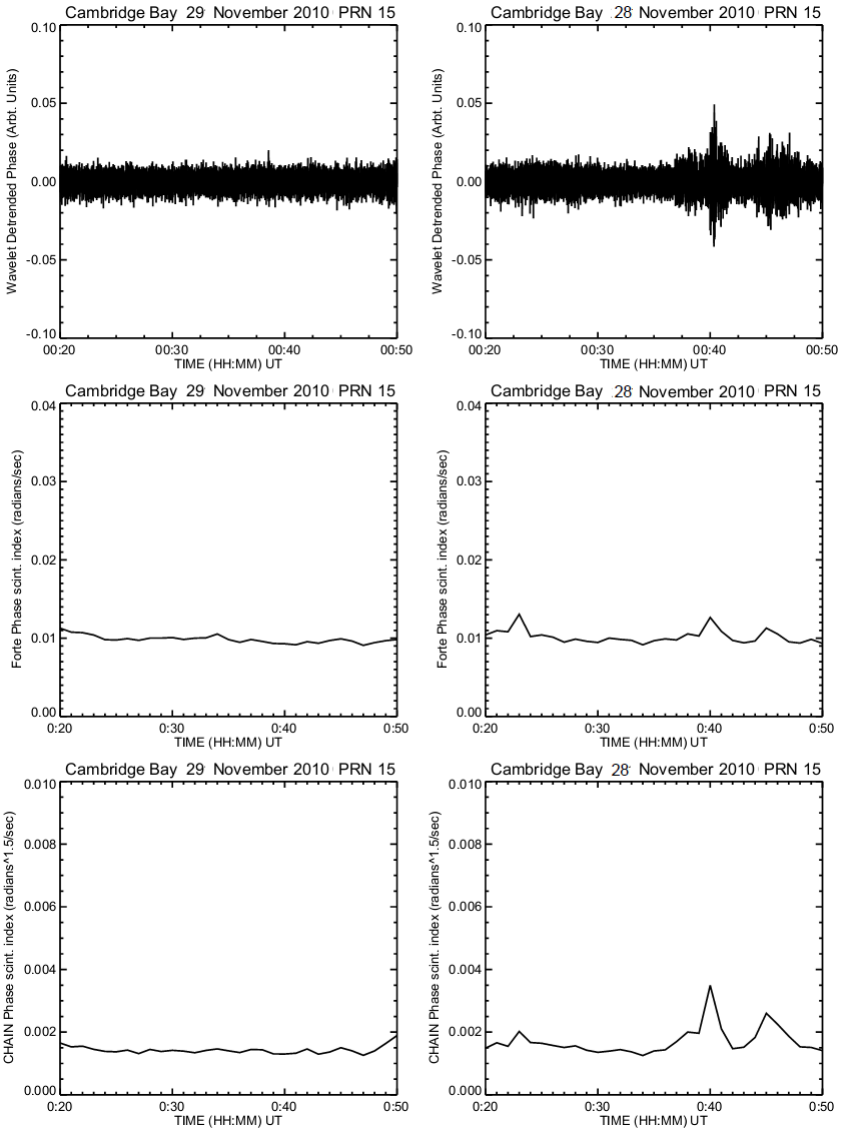

Figure 6.10: Comparing the performance between σ_{Forte} and σ_{CHAIN}. Detrended phase and the corresponding σ_{Forte} and σ_{CHAIN} values are shown for both quiet (left column) and active (right column) ionospheric periods as observed at Cambridge Bay (69.120^{o}N, 254.970^{o}E geog.) on 29 November 2008 and 28 November 2008, respectively, for PRN 15 between 00:20 UT and 00:50 UT on both days. σ_{Forte} is not able to give as accurate a measure of the scintillation compared to σ_{CHAIN}.

amples of such a comparison are shown in Figures 6.11 and 6.12, where wavelet-derived σ_ϕ, wavelet-derived σ_{CHAIN}, and wavelet-derived S_4 are shown for six different scintillation events observed at different times and locations. σ_{CHAIN} was scaled by a factor of 10 to make both S_4 and σ_{CHAIN} be on the same scale. It can be easily seen from these figures that σ_{CHAIN} is a better phase scintillation index compared to σ_ϕ. It can be observed that σ_ϕ is being overestimated and it does not follow S_4 most of the time. Contrary to this, variations in σ_{CHAIN} are very similar to S_4. Since the weak scintillation theory indicates that the phase scintillation variation should be very similar to the amplitude scintillation [11], these results seem to be indicating that σ_{CHAIN} is a better phase scintillation index.

In order to do a more thorough comparison between σ_{CHAIN} and σ_ϕ, a correlation analysis, as shown initially in Figure 6.6, was performed between wavelet-derived S_4 and σ_{CHAIN} (Figure 6.13) using the same data as that used in panel 6.6(c). From Figure 6.13, it is clearly seen that the correlation between the amplitude-scintillation index (S_4) and the phase-scintillation index is greatly improved to 0.90 when σ_{CHAIN} is used compared to 0.79 when using σ_ϕ(panel 6.6(c)). This high correlation between S_4 and σ_{CHAIN} supports the contention that σ_{CHAIN} is a better phase-scintillation index for high latitude measurements compared to σ_ϕ. One more point to emphasize here is that the "phase scintillation without amplitude scintillation" phenomenon is reduced significantly when we use wavelet-based detrending.

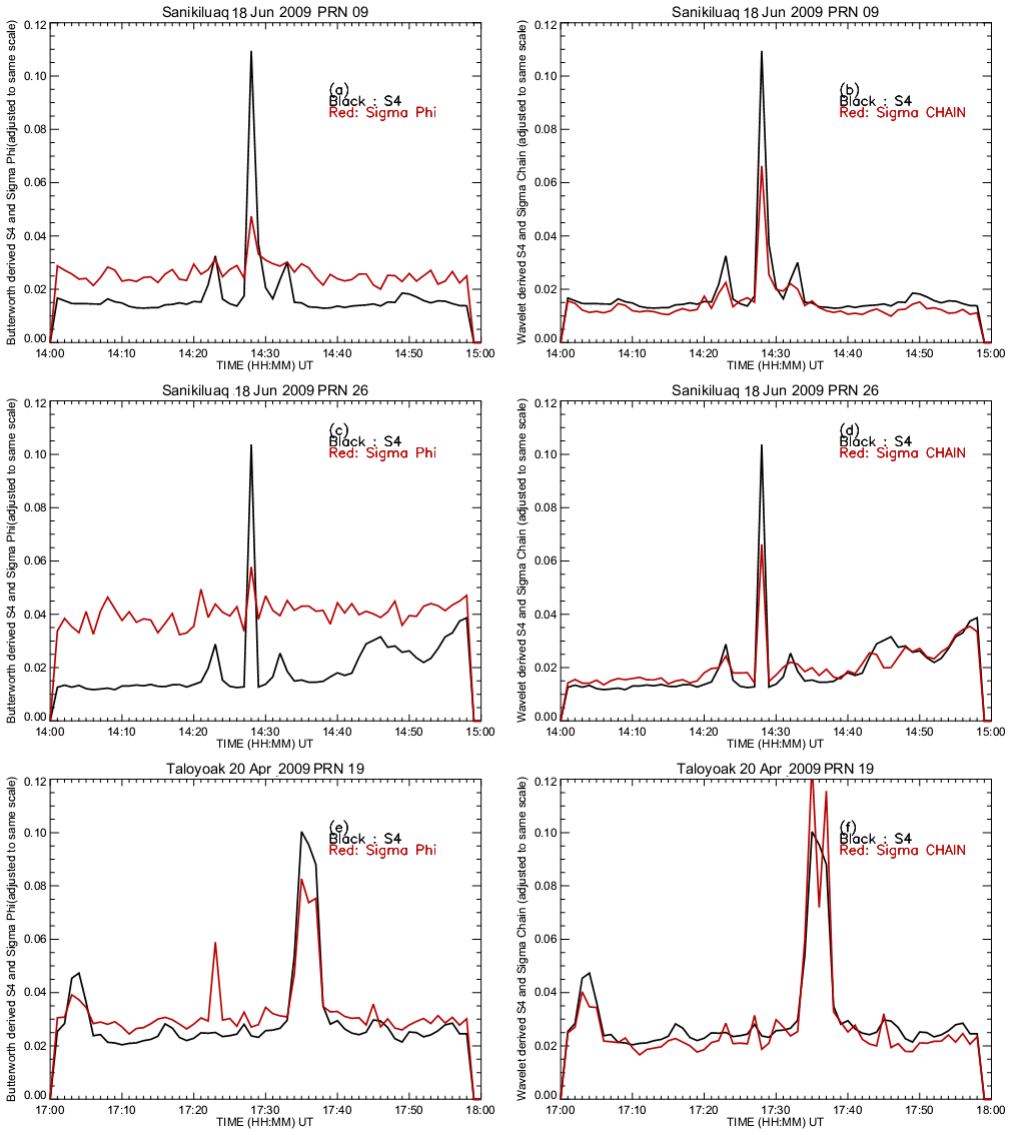

Figure 6.11: Comparing the performance between σ_ϕ and σ_{CHAIN}. Three different scintillation events observed at the mentioned location and date are shown. Left side panels show wavelet-derived σ_ϕ (red) with wavelet-derived S_4 (black) while the right side panels show wavelet-derived σ_{CHAIN} (red) with wavelet-derived S_4 (black). σ_{CHAIN} was multiplied by 10.0 to bring it to the same scale as S_4. Superior performance of σ_{CHAIN} can be clearly seen from the panels as it follows S_4 much better than σ_ϕ.

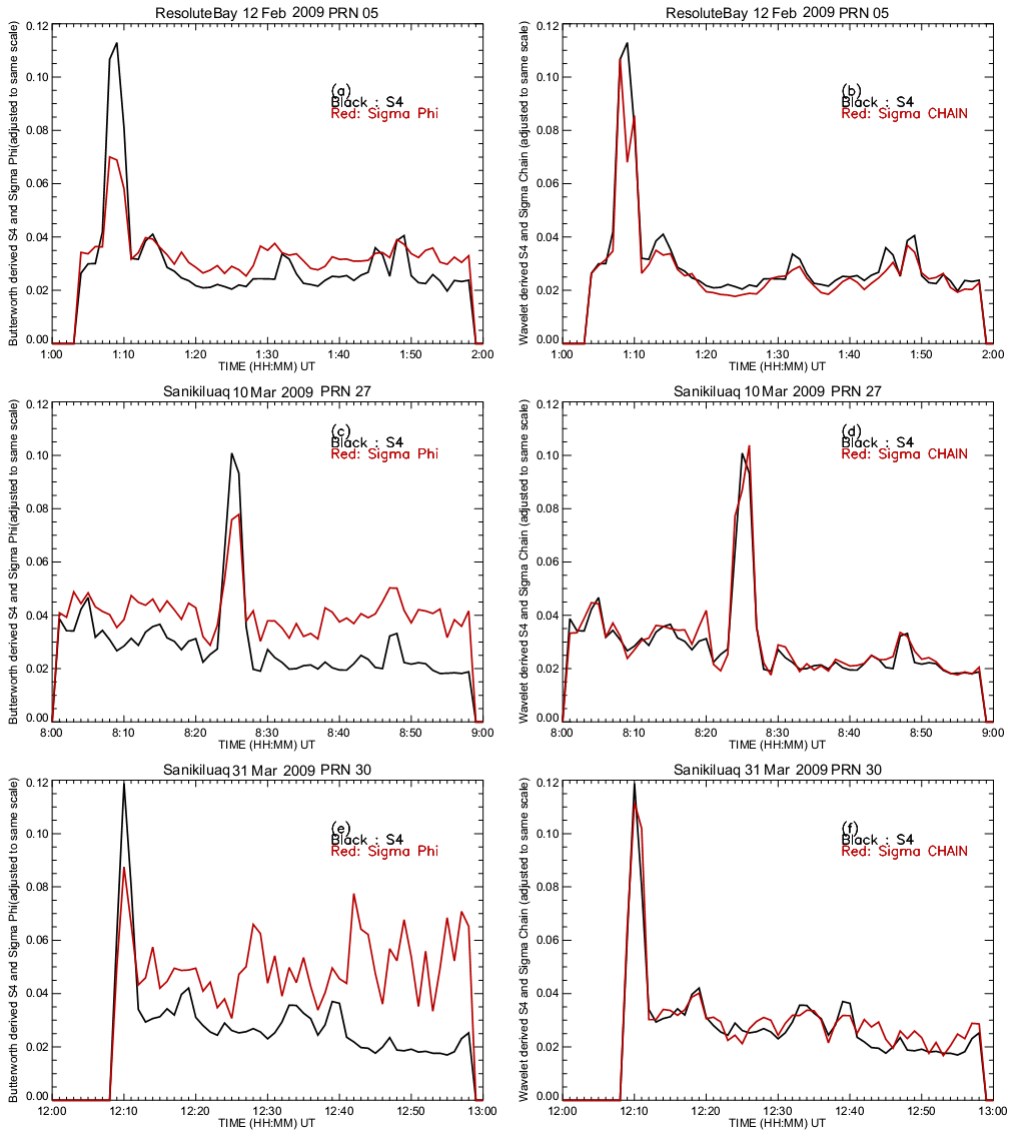

Figure 6.12: Comparing the performance between σ_ϕ and σ_{CHAIN}. Three different scintillation events observed at the mentioned location and date are shown. Left side panels show wavelet-derived σ_ϕ (red) with wavelet-derived S_4 (black) while the right side panels show wavelet-derived σ_{CHAIN} (red) with wavelet-derived S_4 (black). σ_{CHAIN} was multiplied by 10.0 to bring it to the same scale as S_4. Superior performance of σ_{CHAIN} can be clearly seen from the panels as it follows S_4 much better than σ_ϕ.

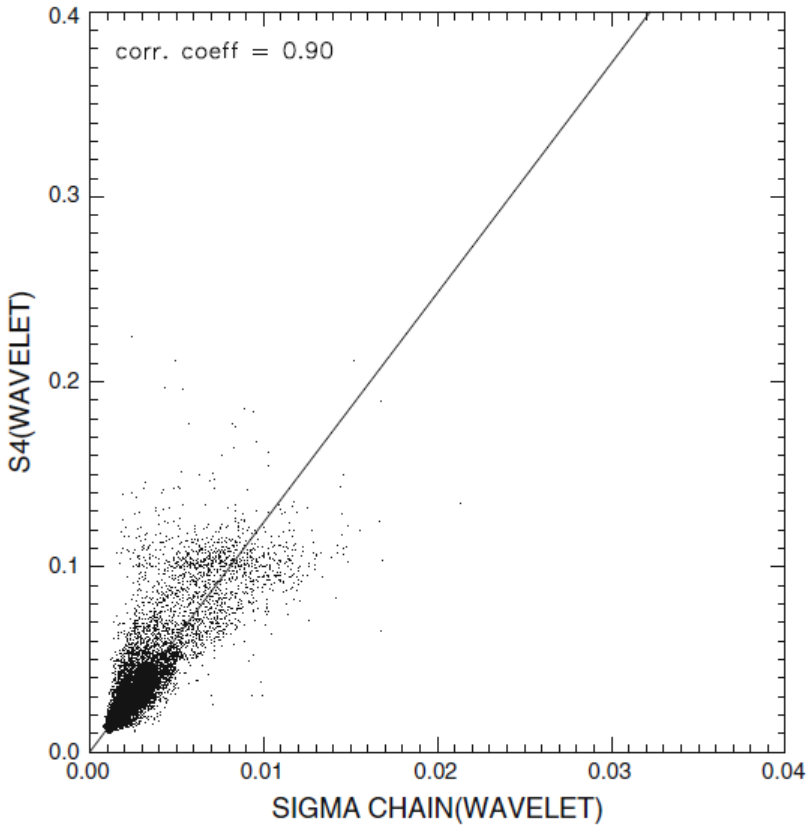

Figure 6.13: Correlation analysis using a scatter plot between wavelet-derived S_4 and σ_{CHAIN}, showing progressively improved correlation coefficient of 0.90 with no "phase scintillations without amplitude scintillation" events. Around 400 scintillation events (1 hour of data for each event) are considered in this plot.

6.2.4 Conclusion

In this work, the observed scintillations never had S_4 values greater than 0.4, and so a very high correlation was expected between the amplitude and phase scintillation index. These results agree with that expectation and it shows that if one can eliminate precisely the trend and noise in the received raw power and phase of the GPS signal, the scintillation indices derived from these filtered signals are indeed very similar [11] when the scintillation magnitude is weak ($S_4 < 0.4$). These results have also shown that by using a better detrending method and a better scintillation index, artifacts like "phase scintillation without amplitude scintillation" can be mitigated. As some previous works predicted [72, 44], wavelets seem to be better suited for detrending GPS signals as they seem to remove the slow fluctuations and noise significantly better than previously used methods. As also shown in previous studies [19, 17], it is illustrated (Figures 6.3, 6.4, 6.5) that like the phase scintillation indices, S_4 is affected by the detrending process. The magnitude of this effect is significant enough that it should be considered in all scintillation studies. One aspect to keep in mind is that even though a constant cutoff scale/frequency in place of an ever changing Fresnel frequency was used, better results were obtained by using wavelets and σ_{CHAIN}. This is because wavelets give a better detrended signal as local features of the signals are preserved. Futher, it is also observed that the lower cutoff frequency of 0.193Hz (derived from GPS data) is a better approximation to the Fresnel frequency at these high latitudes compared to 0.1 Hz (derived from

mid- and low-latitude Wide-band satellite system data). Taking these results as precedent, the raw phase and power data obtained from all CHAIN receivers for the years March 2009-March 2011 were detrended using the wavelet filtering method. S_4 and σ_{CHAIN} were calculated from these wavelet detrended signals to represent GPS high latitude amplitude scintillation and phase scintillation respectively. These scintillation indices were then used to create GPS scintillation climatologies of the amplitude and phase scintillation in high latitudes. These climatologies are important as they give us information about the spatial and temporal changes of scintillation and an insight into the physical processes that cause them. The next chapter, Chapter 7, discusses these GPS scintillation climatologies observed in high latitudes.

Chapter 7

Climatology of GPS Scintillation

7.1 Introduction

The climatology of scintillation is one of the important characteristics needed to model ionospheric scintillation [72, 63]. Since scintillation climatology provides information about how scintillation varies spatially and temporally, this information can also provide insights into mechanisms that are producing scintillation. These climatologies can then be used as input for scintillation models [58, 59]. Initial studies on high latitude scintillation climatology were done primarily using satellite signals in the UHF/VHF range. These signals were usually from middle or low Earth orbiting satellites or geostationary satellites. In order to obtain a better understanding of the high

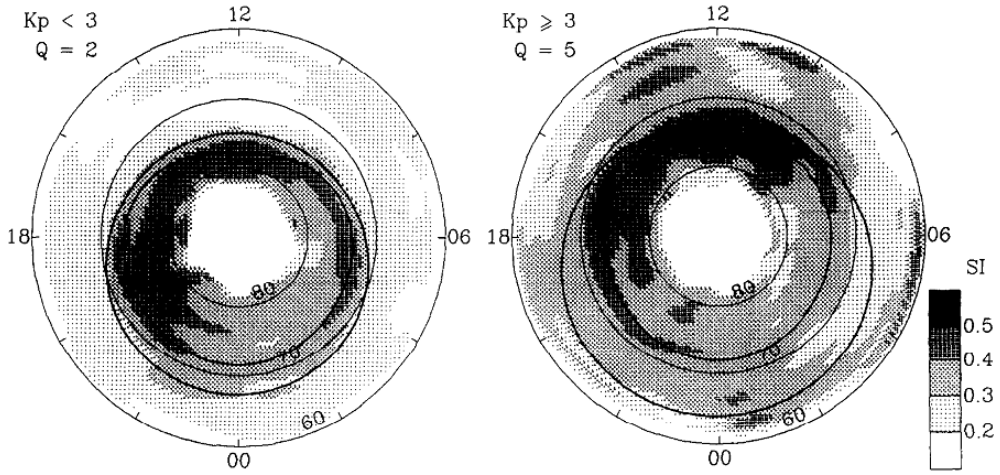

Figure 7.1: Maps of amplitude scintillation index in a corrected magnetic latitude-magnetic local time coordinate system for low (left panel) and high (right panel) geomagnetic activity [23]

latitude scintillation, a satellite called the High Latitude Research Satellite (HILAT) was launched in the mid 1980s which transmitted at five different frequencies; namely, 138, 390, 413, 536, 1239 MHz [23]. Several studies have been performed using data from the HILAT satellite, which led to the better understanding of high latitude plasma structures and scintillation in the UHF/VHF range. Figure 7.1 shows one such result derived from HILAT satellite data at a Polish polar station Hornsund, Spitsbergen. This figure shows the maps of the amplitude scintillation index (SI) for both low and high geomagnetic activity.

It is important to mention that these studies used only amplitude scintillation data, and these amplitude scintillation climatologies were later used to

build scintillation models that are useful in predicting and mitigating scintillation effects. Early scintillation studies [1], that were typically limited to intensity scintillation characterized by intensity (amplitude) fading or S_4 index, found seasonal and diurnal variations of scintillation at all latitudes. In the auroral zone it was shown that VHF/UHF scintillation activity was high even when geomagnetic conditions were quiet. In the polar cap, amplitude scintillation exhibited clear seasonal and UT variation, which was consistent with mesoscale plasma density modeling results [1].

The main disadvantage that was inherent in these studies was the sparse spatial coverage of the receivers. With the advent of GPS and the creation of networks like CHAIN, scintillation climatology for high latitudes with better spatial coverage is now possible [63, 51]. Before GPS, L-band scintillation climatologies were created mainly by extrapolating results from other frequencies into L-band [7]. An important advantage of using custom-made GPS receivers, like those used in CHAIN, is their ability to obtain high resolution phase scintillation data. These can then be used to create a phase scintillation climatology that can be used to better understand the phenomenon responsible for scintillation.

7.2 Method of Analysis

In this analysis, CHAIN data for the period, March 2009 to March 2011, were used to create a scintillation climatology. The undetrended/raw phase and power data were detrended by using the wavelet-detrending method as discussed in Chapters 5 and 6. This detrended data was then used to calculate the scintillation indices (S_4 and σ_{CHAIN}). In order to process this enormous data set, the Atlantic Computational Excellence Network (ACEnet), a consortium of Atlantic Canada universities providing researchers with high performance computing (HPC) resources, was used. It took one year to process these data at ACEnet compared to ≈120 years it would have taken to process the same data on a PC.

Since the ionosphere at high latitudes is mainly dependent on the interactions between the Earth's magnetic field and the inter-planetary magnetic field, and scintillation being a phenomenon in the Earth's ionosphere, a coordinate system based on the magnetic field is often used. In this study, the Altitude Adjusted Corrected Geomagnetic Coordinates (AACGM) [2] are used as the magnetic field coordinates since they are well defined and smooth over the entire globe. The magnetic coordinate system is defined in terms of magnetic latitude (MLAT) and magnetic longitude. It should be noted that magnetic longitude is usually replaced by magnetic local time (MLT) as this would make it easier to relate the phenomenon to the Sun's position with respect to

the Earth's magnetic field [2, 51, 63]. Assuming the Ionospheric Pierce Points (IPP) are at an altitude of 350 km, magnetic latitudes and magnetic local time were calculated for all satellite passes with an elevation of more than 30^o. Along with this elevation cutoff, scintillation events were also manually sifted to make sure that most of the multipath is removed. A list of all CHAIN sites and their respective geographical and magnetic coordinates is given in Table 7.1.

Table 7.1: Geographic and corrected geo-magnetic coordinates of CHAIN stations [51]

Station	Geog. Lat.(^oN)	Geog. Long.(^oE)	Corrected Geomag. Lat.(^oN)	Corrected Geomagnetic Longitude(^oE)
Eureka	79.99	274.10	88.10	329.86
Resolute Bay	74.75	265.00	83.13	320.61
Pond Inlet	72.69	282.04	81.67	0.69
Cambridge Bay	69.12	254.97	77.24	310.11
Taloyoak	69.54	266.44	78.75	329.70
Hall Beach	68.78	278.74	78.33	353.45
Qikiqtarjuaq	67.53	295.97	75.77	22.57
Iqaluit	63.73	291.46	72.85	14.04
Sanikiluaq	56.54	280.77	67.19	356.44
Ministik Lake	53.35	247.03	61.50	307.57

To understand the climatology or seasonal and spatial variability of scintillation, the data set from all 10 sites of CHAIN were divided into four 3-month intervals that are approximately centered on equinoxes and solstices [51]:
Summer = May to July

Autumn = August to October

Winter = November to January

Spring = February to April

These four data sets were then used to form corresponding scintillation maps of S_4 and σ_{CHAIN}. These data were then merged into bins of 1h MLT $\times$ 2^o MLAT. Figure 7.2 shows a map of the number of data points for each bin which indicates that for a particular magnetic latitude, there is constant data coverage at all times of the day. It can be also observed that since most of the data is present in the polar regions (above 75^0 MLAT), this is the region of interest in this analysis.

Using these data, scintillation maps, which are maps of the percentage of occurrence of the scintillation indices, are created. The percentage of occurrence in the maps is evaluated for each bin as :

$$percentage\ occurrence = N(S_4\ or\ \sigma_{CHAIN} > Threshold)\ /\ N_{Total} \quad (7.1)$$

where $N(S_4\ or\ \sigma_{CHAIN} > Threshold)$ is the number of data points corresponding to a scintillation index above a given threshold, and N_{Total} is the number of data points in the bin. The thresholds selected are 0.05 for S_4 and 0.004 for σ_{CHAIN} to differentiate between scintillation and no scintillation. The range of magnetic latitudes used in these maps is from 42 MLAT to 90 MLAT. To remove the contribution of bins with poor statistics, the selected

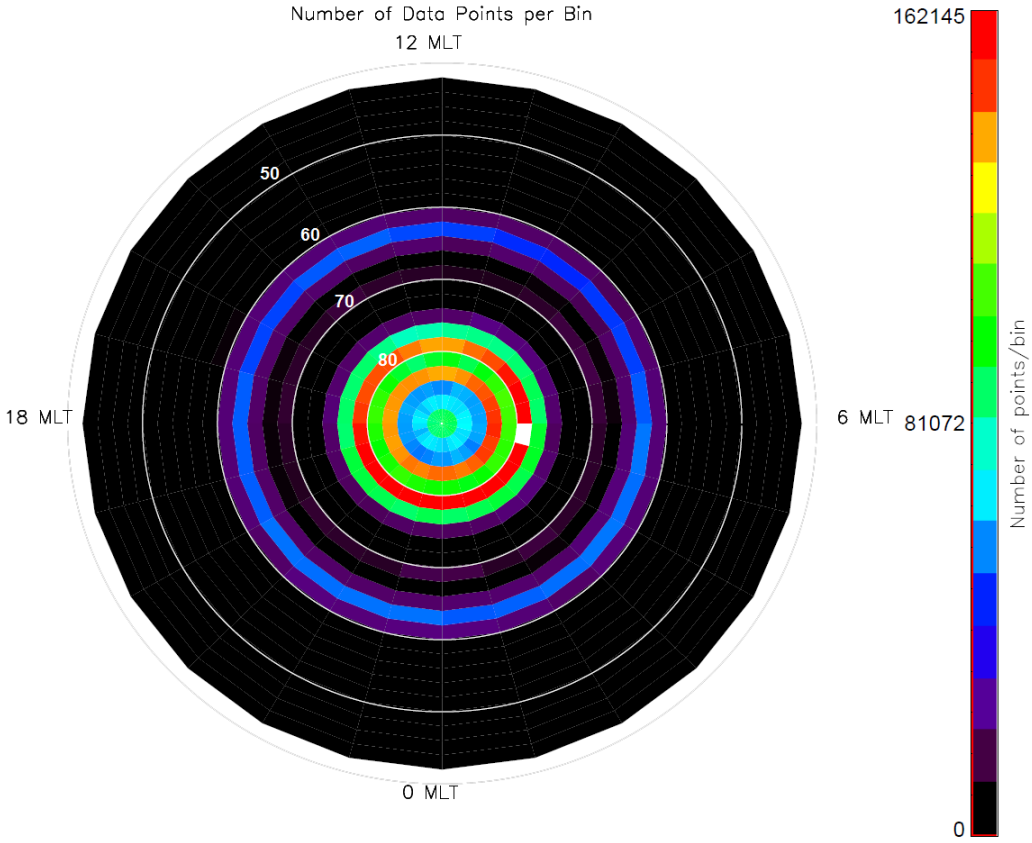

Figure 7.2: CHAIN data coverage for the period March 2009 to March 2011 represented as a magnetic latitude vs magnetic local time map. With the center being the magnetic pole and concentric circles representing different magnetic latitudes.

accuracy is defined as [63, 51]

$$R = 100 \times \frac{\sigma(N_{Total})}{N_{Total}} \tag{7.2}$$

has to be less than 2.5 percent and $\sigma(N_{Total}) = (N_{Total})^{\frac{1}{2}}$ is the standard deviation of the number of data points in the bin. Usually, bins in the border of the field of view of the stations are the ones not satisfying the condition on accuracy. Figure 7.3 is such an example of a scintillation map produced in this analysis. The colour coding represents the percentage of occurence while "s" represents the position of the solar terminator at the start of the time interval used to create this map. "e" represents the position of the solar terminator at the end of the time interval.

Also, as stated in equation (4.27) in Chapter 4, scintillation is related to $\frac{\Delta N}{N}$ where ΔN is the fluctuations in the electron density of the ionosphere, while N is the background electron density of the ionosphere along the signal. In this analysis, $TECgradient = \frac{\Delta TEC}{TEC} \times 100$, which represents the fluctuations in the TEC with respect to the background TEC as a percentage, was used as a quantitative variable to represent $\frac{\Delta N}{N}$. Similar to S_4 and σ_{CHAIN}, TEC gradient maps were created and the percentage of occurrence in these TEC gradient maps is also evaluated for each bin as :

$$percentage\ occurrence = N(TECgradient > Threshold)/N_{Total} \tag{7.3}$$

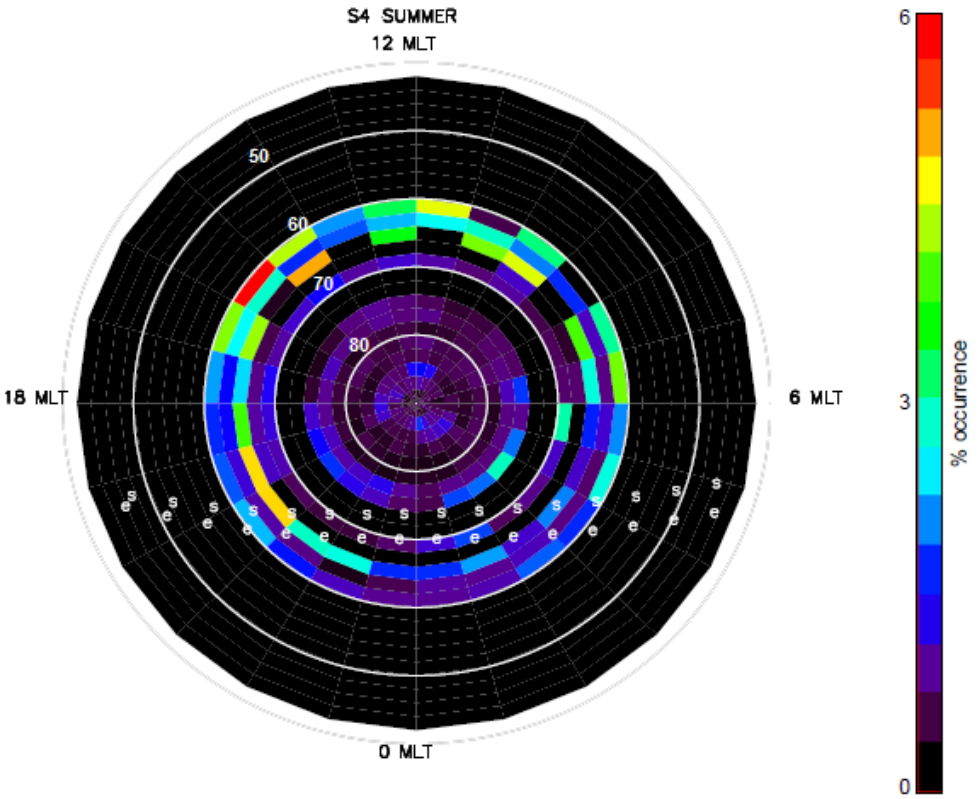

Figure 7.3: Example of scintillation map with center being the magnetic north pole and concentric circles representing different magnetic latitudes. Magnetic local time can also be observed along with the position of the terminator at different times. "s" represents the position of the terminator at the start of the time interval used to create this map. "e" represents the position of the terminator at the end of the time interval.

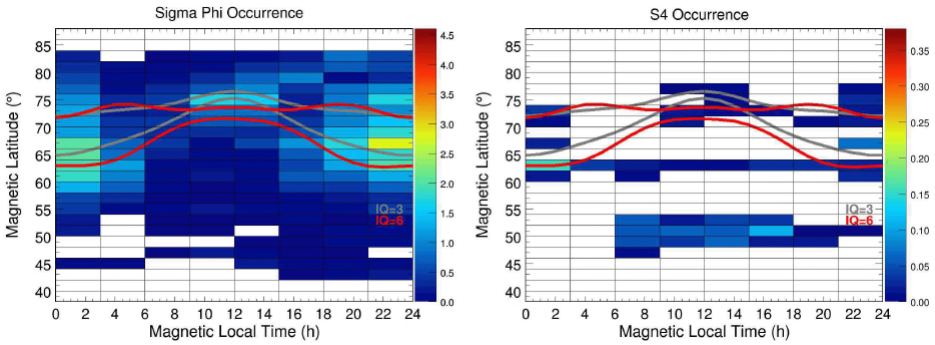

Figure 7.4: Maps of σ_ϕ percentage occurrence (left) and maps of S_4 percentage (right). Note the color scales are different. Maps are all for all 4 stations for a period of 3 months (October-December 2003). [63]

where $N(TECgradient)$ is the number of data points corresponding to the TEC gradient above a given threshold, and N_{TOTAL} is the number of data points in the bin. The threshold value for the TEC gradient chosen for this study is 5 percent.

7.3 Results

Previous studies, [63, 51], that have dealt with GPS high latitude scintillation have not considered the amplitude scintillation climatology as amplitude scintillation occurrence was considered to be much lower than phase scintillation. An example of such a result, [63], is illustrated in Figure 7.4 where amplitude scintillation is quantified by S_4 and phase scintillation by σ_ϕ.

This I think is the result of "phase scintillation without amplitude scintil-

lation", which resulted due to the use of default detrending of the data. By using the new detrending method and the new phase scintillation index (σ_{CHAIN}), which were introduced in Chapter 6, amplitude scintillation and phase scintillation maps (Figures 7.5 and 7.6 respectively) were created for all four seasons taking into consideration the two years of data. It is observed from Figures 7.5 and 7.6 that both amplitude and phase scintillation are spatially and temporally equally probable in contrast to previous high latitude GPS climatologies. This is a significant result as it confirms the weak scintillation theory. This will be further discussed later in Section 7.4.

A significant seasonal variation was also observed in both amplitude and phase scintillation climatology maps especially in the polar regions (70^0 MLAT to 90^0 MLAT). An annual cycle in the percentage of occurrence of scintillation with maximum in the winter and minimum in the summer is observed. These results are similar to other studies [63], which indicate higher phase scintillation occurrence in winter compared to summer. From the terminator positions shown in Figures 7.5 and 7.6, it also can be seen that scintillations are more pronounced when there is sunlight for a shorter period of time and less pronounced when there is sunlight for a longer period of time. Scintillation in the polar cap occurred mostly in the cusp region (75^0 MLAT to 85^0 MLAT) and temporally most of this scintillation observed in the cusp region was around ± 2 hours of magnetic local noon. TEC gradient maps, Figure 7.7, also follow similar seasonal and temporal variations as

illustrated in the cusp region of the scintillation maps (Figures 7.5 and 7.6).

7.4 Discussion

Scintillation Occurrence in the Cusp

As discussed in Chapter 2, the cusp region is where the footprints of the open magnetic field lines are located, and electrons are precipitated along these magnetic field lines into these regions. Figure 7.8 shows the probability of observing cusp precipitation as a function of MLAT and MLT [49]. It is also observed that the scintillation maps (Figures 7.5, 7.6) show a predominance of scintillation around the same latitude and time indicating that one of the main cause of scintillation could be particle precipitation at the cusp. It is believed that these precipitated electrons form irregularities/gradients in the ionosphere which in turn can cause scintillation [7].

TEC gradient maps (Figure 7.7) also show similar seasonal and spatial variations as seen in the scintillation maps (Figures 7.5 and 7.6). This result agree with the notion that TEC gradients are one of the main causes of scintillation. Although this result indicate the cause of the scintillation, it does not explain the observed seasonal variations since there is particle precipitation in the cusp all year around [26]. To explain this variation, the effect of sunlight on electron density gradients should be considered. In summer, the

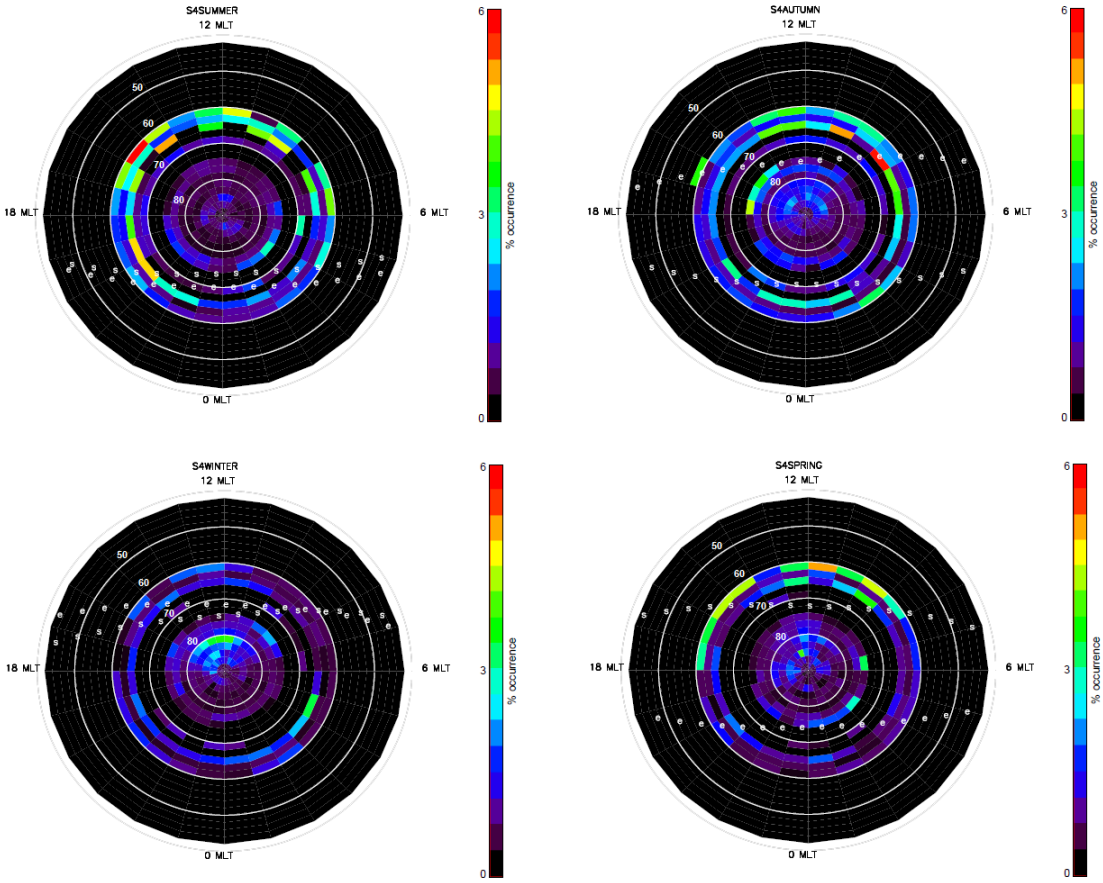

Figure 7.5: Climatology of S_4 / amplitude scintillation occurrence for 4 different seasons (summer, autumn, winter, spring). The position of the terminator at starting (s) and ending (e) of the particular season is also shown.

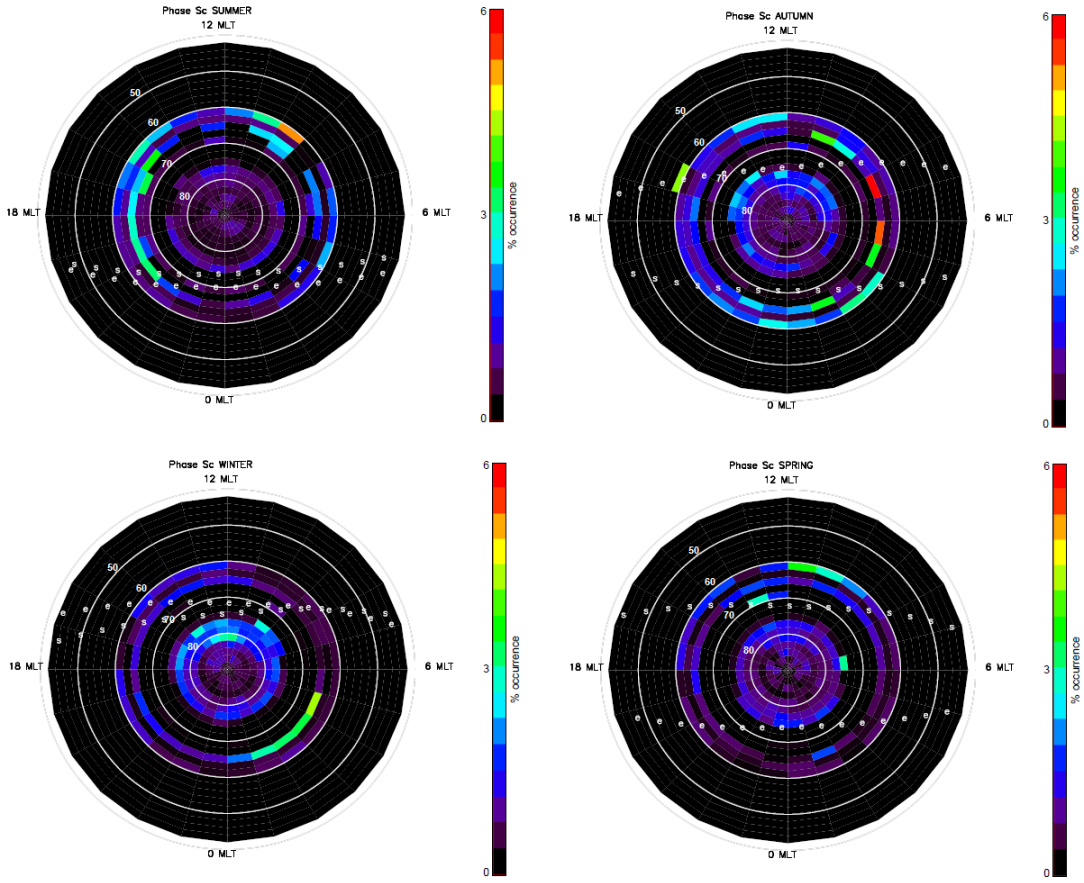

Figure 7.6: Climatology of σ_{CHAIN} / phase scintillation occurrence for 4 different seasons (summer, autumn, winter, spring). The position of the terminator at starting (s) and ending (e) of the particular season is also shown.

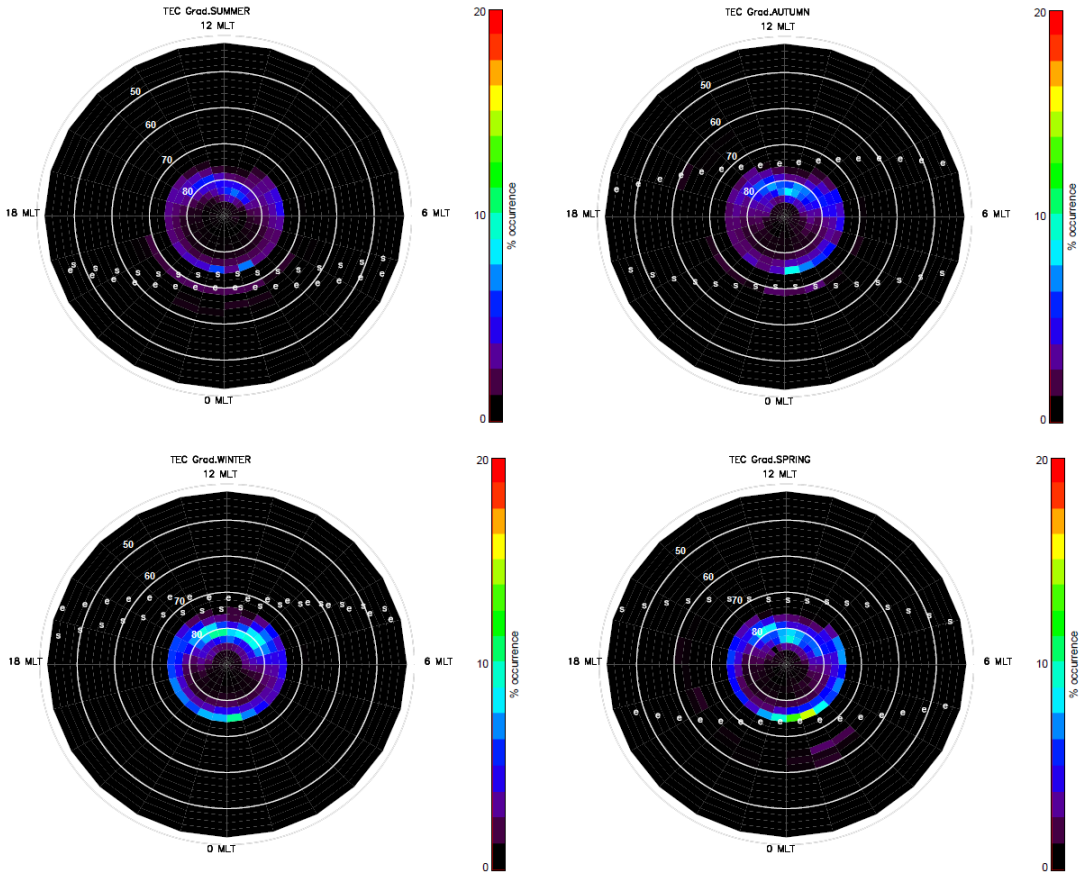

Figure 7.7: Climatology of total electron content (TEC) gradient occurrence for 4 different seasons (summer, autumn, winter, spring). The position of the terminator at starting (s) and ending (e) of the particular season is also shown.

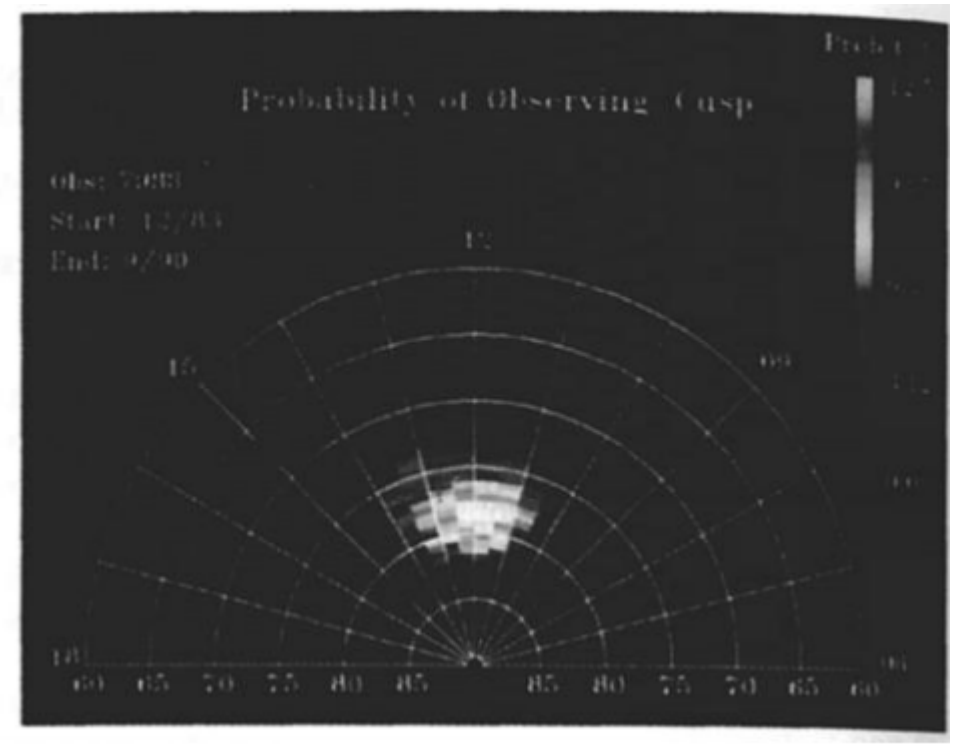

Figure 7.8: Probability of cusp precipitation with respect to MLT and MLAT [49]

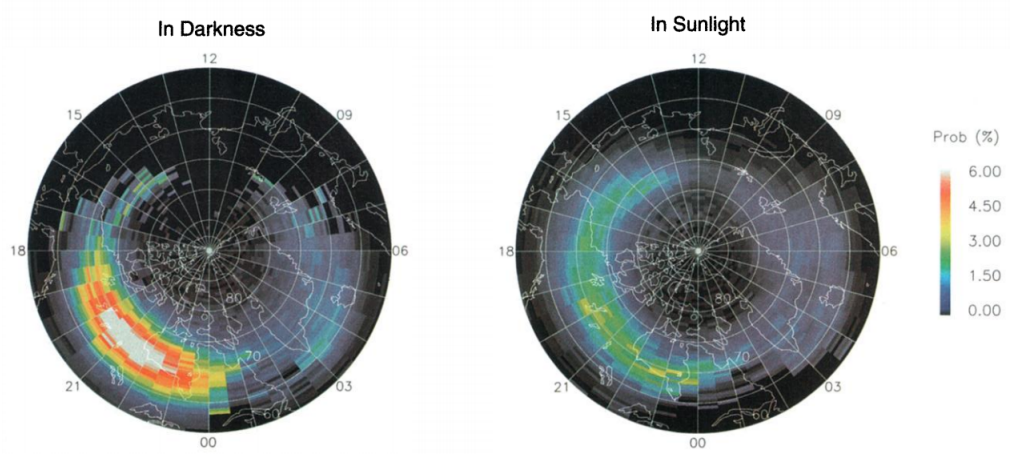

Figure 7.9: Intense discrete aurora occur more frequently in darkness than in sunlight. This effect is attributed to the change in electron density due to photoionization. [48]

sun never goes below the horizon at these latitudes, which means that there is photoionozation all day long. As a result there is a higher background electron density in the ionosphere which suppresses gradients so that scintillation is less likely. In winter as the sun is never above the horizon at these latitudes, consequently the electron density gradients are sustained. Similar results [48] have been observed in the auroral region, where it has been observed that the occurrence of aurora has been quelled in summer compared to winter (Figure 7.9) since there is no sunlight and hence no photoionization in winter.

Equal Probability of Phase and Amplitude Scintillation

Previous GPS high latitude climatology results [51, 63] have indicated that

of phase scintillation is more probable than amplitude scintillation. These results contradict the scintillation theories that predict phase and amplitude scintillation to have equal probability of occurrence under weak scintillation. And "Phase Scintillation without Amplitude Scintillation" effects that have been discussed in Chapter 5 and Chapter 6 and the associated development of scintillation models to support the existence of these effects. In contrast, from Figures 7.5 and 7.6, one can clearly see that there is an equal probability of occurrence of both phase and amplitude scintillation both temporally and spatially.

Note that the scintillation data used in this analysis were detrended by the wavelet-detrending method introduced in Chapter 6. This detrended data was then used to calculate the scintillation indices. The new phase scintillation index (σ_{CHAIN})that was also introduced in Chapter 6 was used in place of σ_{ϕ}. The resulting climatology results is very important as it shows that by using a proper detrending method and a better scintillation index, one can obtain results that agree with the theory. These results can be used to create improved scintillation models, which would help in predicting and mitigating scintillation. Given the spatial and temporal distribution of phase and amplitude scintillation, these results also suggest the same irregularities are causing both amplitude and phase, again in agreement with the scintillation theory.

7.5 Conclusion

By using wavelet-detrended data and the CHAIN scintillation index as the phase scintillation index, it is demonstrated that both phase and amplitude scintillation have similar climatalogies in agreement with scintillation theories. These results also support previous works, which indicated that by using better and new ways to analyze and represent scintillation data unwanted artifacts would be removed from the data. Using these results, one can also observe that the spatial and seasonal variation of the sun's position plays an important role in scintillation climatology.

Scintillation climatologies do not provide all the information needed to determine the source of scintillation producing irregularities in the ionosphere. It can be clearly seen from TEC gradient maps (Figure 7.7) which show similar spatial and temporal variability as the scintillation maps (Figures 7.5 and 7.6) that TEC gradients can be one of the main sources for scintillation.

In order to obtain a much more comprehensive knowledge of the ionospheric irregularities that are causing scintillation in GPS signals, one has to apply methods such as spectral analysis to the GPS scintillation signals. This has been undertaken and is described in Chapter 8.

Chapter 8

Irregularity Characteristics

8.1 Introduction

Understanding the characteristics of scintillation-producing ionospheric irregularities is an essential piece of the puzzle that has to be solved in order to obtain a complete interpretation of ionospheric scintillation. Characteristics such as spectral slope, fading rate, and characteristic size of irregularities are not only used in ionospheric studies but also in creating scintillation models and designing better receivers [58, 59, 65]. These characteristics, which give information about the irregularities, are usually obtained by analyzing electromagnetic scintillation signals that have traversed through or been reflected from the ionosphere and are received at the ground. Thus one has to somehow relate these ground measurements to irregularities that occur from 200 km to 450 km from the ground. As discussed in Section 4.3, one

can relate the power spectra of fluctuations observed in the radio signal to fluctuations in the refractive index in the ionosphere which in turn can be used to define the characteristics of the irregularities [75].

Initial studies [33, 14, 56, 57, 69, 5, 8, 6, 68, 4] that dealt with irregularity spectra used radar and low-Earth orbiting satellites. These studies mainly concentrated on mid- and low-latitudes, and most of the studies used amplitude scintillation data for their analyses since obtaining phase scintillation data required custom-made receivers which were not available. Although these early studies were constrained both temporally and spatially, important breakthroughs were made. An example of such a breakthrough is that, based on results from experiments involving radar, satellites, and in-situ measurements, it was observed that power spectra of the ionospheric irregularities follows a power-law spectrum [33, 14, 56, 57, 69, 5, 8, 6, 68, 4]. An illustration of a spectrum of ionospheric irregularities which obeys a power-law structure of ionospheric irregularities as a function of wavenumber is shown in Figure 8.1.

From Figure 8.1, it can be observed that no single size of irregularity is responsible for generating scintillation,and instead the irregularities that cause ionospheric scintillation range in size from tens to hundreds of metres. The advent of GPS, introduced a new and popular tool to study the ionosphere and create scintillation models, because of its excellent temporal and spatial

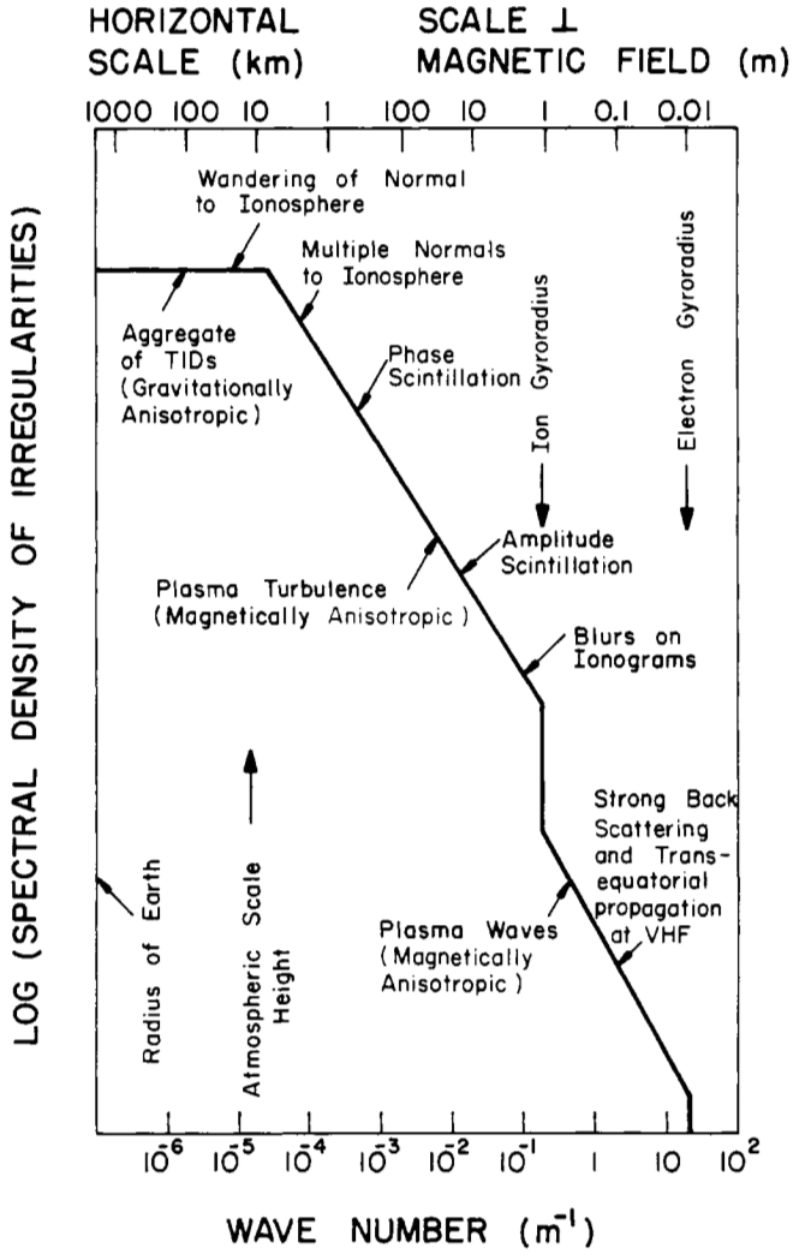

Figure 8.1: A composite spectrum summarizing intensity of ionospheric irregularities as a function of wavenumber over a spatial scale from the electron gyro-radius to the radius of the Earth. [75]

coverage [37]. However, it should be noted here that these models were not suitable for high latitude scintillation as not enough data were available from the high latitudes ensure that the physics relevant to high latitudes was incorporated. Given the variability and importance of high latitude ionosphere, a scintillation model specifically for high latitudes is needed.

8.2 Data Analysis

In order to obtain the spectral characteristics of scintillation data from high latitudes, amplitude and phase scintillation signals obtained from CHAIN were detrended using the wavelet detrending filter described in Section 5.5, with a lower cutoff frequency of 0.1 Hz. This frequency was chose to observe the behaviour of the power spectra just below the Fresnel frequency which was shown in Section 6.2 to be typically higher than 0.1 Hz. Once detrended, auto-correlation values were calculated [61] for every minute of scintillation data with the assumption that the characteristics for irregularity producing scintillation do not change in this time interval. In this analysis $\approx$1000 "one minute" auto-correlation values were calculated. Another important parameter used in this analysis was the relative velocity, V_r, between the satellite ionospheric pierce point (IPP) velocity and the ionospheric drift. The principal requirement for calculating the relative velocity between the ionosphere and the satellite is identifying a common reference frame for both these velocities. The ionospheric drift velocity is obtained from the ionoson-

des co-located with some of the GPS receivers in the CHAIN network. As shown in Section 2.5, the ionosonde provides the magnitude of the horizontal ionospheric drift velocity, the azimuth angle, and the vertical velocity with respect to the ionosonde's location. Thus the east(E), north(N), and up(U) components of the ionospheric drift velocity can be calculated with respect to the ionosonde's position on the ground. Hence ionospheric drift velocities are determined in the ENU reference frame.

To obtain the satellite IPP velocity in the ENU frame, the height at which the IPPs should be calculated should be known. In this study, ionosonde data are used to obtain the height of the ionosphere. It was found that 300 km was the average height of the ionosphere for the scintillation events taken into account in this analysis. Hence 300 km is chosen as the height at which the satellite IPP velocity is to be calculated. The coordinates of the IPP are calculated at this height. Noted that the IPP coordinates are in the Earth centered Earth fixed (ECEF) frame, that is, the point (0,0,0) in the reference frame is defined as the center of mass of the Earth, hence the name Earth-Centered. Its axes are aligned with the International Reference Pole (IRP) and the International Reference Meridian (IRM) that are fixed with respect to the surface of the Earth, hence the name Earth-fixed [71, 40]. Figure 8.2 illustrates both the ENU reference frame and the ECEF reference frame.

In order to calculate the relative velocity, V_r, these ECEF IPP coordinates

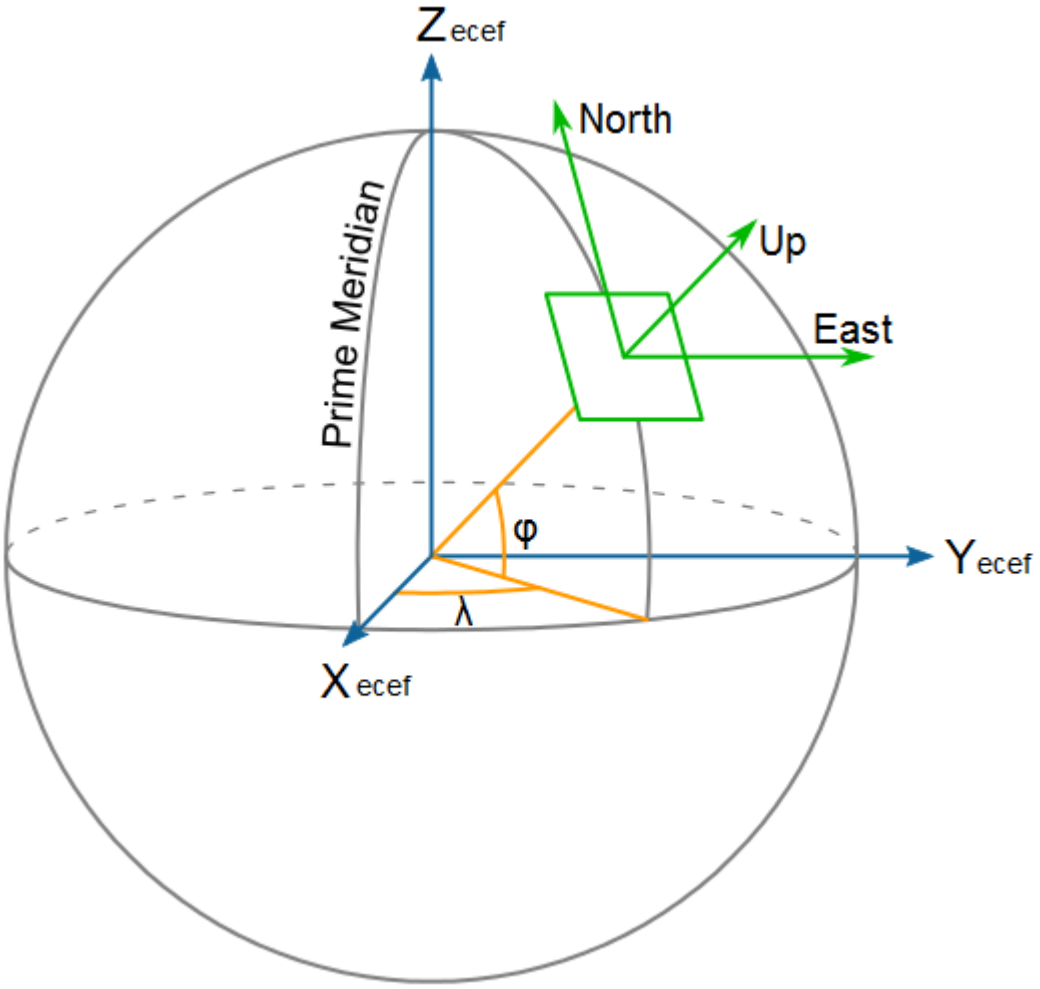

Figure 8.2: Illustration of Earth Centered Earth Fixed (ECEF) frame and East, North, Up (ENU) frame on the Earth's surface. Courtesy of Wikipedia.

are converted to the ENU reference frame using equation (8.1) with the position of the GPS receiver's position as the reference point [71].

$$\begin{bmatrix} x \\ y \\ z \end{bmatrix} = \begin{bmatrix} -sin\lambda_r & cos\lambda_r & 0 \\ -sin\phi_r cos\lambda_r & -sin\phi_r sin\lambda_r & cos\phi_r \\ cos\phi_r cos\lambda_r & cos\phi_r sin\lambda_r & sin\phi_r \end{bmatrix} * \begin{bmatrix} X_p - X_r \\ Y_p - X_r \\ Z_p - Z_r \end{bmatrix} \tag{8.1}$$

Here, $[x, y, z]$ are the ENU coordinates of the satellite IPP.

$[X_p, Y_p, Z_p]$ are the ECEF coordinates of the satellite IPP.

$[X_r, Y_r, Z_r]$ are the ECEF coordinates of the receiver location.

$\lambda_r,\ \phi_r$ are the geo-centric longitude and latitude of receiver location.

More details about this conversion can be found in [71]. These converted IPP coordinates are then utilized to calculate the satellite velocity by using the distance between consecutive ionospheric points and the time taken for the satellite to travel this distance. Since the GPS receivers and the ionosondes are not more than one kilometre apart at any of the CHAIN locations, it was assumed that these instruments were looking at the same part of the ionosphere. These two velocity vectors, therefore, are added using vector analysis to find the relative velocity V_r. This relative velocity is then used to obtain the average size of the irregularity [37].

8.3 Results

8.3.1 Spectral Analysis of Amplitude and Phase Scintillation Signals

Ionospheric scintillation studies in the early 1970s [56] used power spectra obtained from natural radio sources like Cygnus A. As the satellite era dawned, more spectral studies using satellite signals were performed [33, 14, 56, 57, 69, 5, 8, 6, 68, 4]. Analyzing these spectra supplied information on the range of irregularity scales involved and their relative contribution to the creation of scintillation in the signal. An example of such a power spectra consisting of a 250 MHz signal emitted by a quasi stationary Air Force satellite and observed at Goose Bay on 7 March 1982 is shown in Figure 8.3 [5]. Although these studies [6, 68, 4] used data from high latitude regions, the number of stations were few and out of them not many were from the polar cap region.

As indicated in Section 8.2, and observed in Figure 8.3, the intensity power spectra/irregularity spectra have a power-law spectrum associated with them. A power-law behaviour helps relate a particular phenomenon to the specific physical mechanisms that underlie the natural phenomenon in question. This is usually done by calculating the slope of the irregularity spectra and then comparing it to the power spectra of other related phenomenan that may have a similar slope. This similarity in the slope indicates that a similar mechanism is dominant in both these phenomena [6, 68, 4]. An illustration

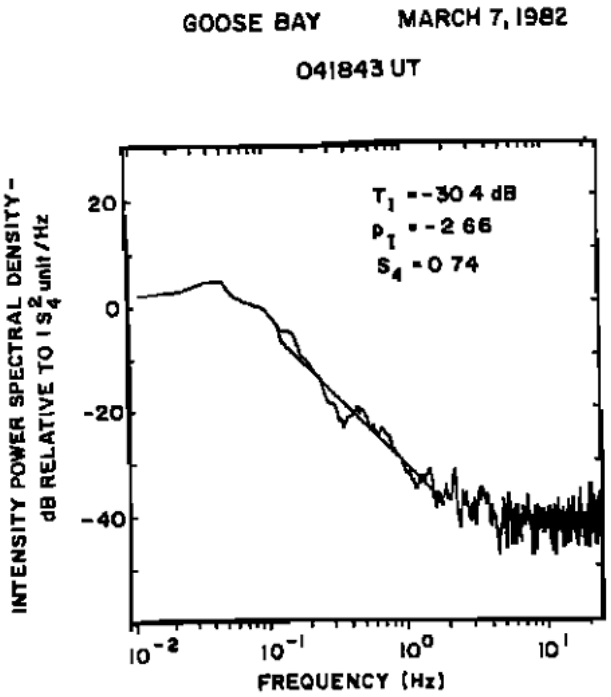

Figure 8.3: Spectra of intensity scintillation index S_4 from Goose Bay on 7 March 1982 at 0418.43 UT. The intensity spectral index is 2.66. [5]

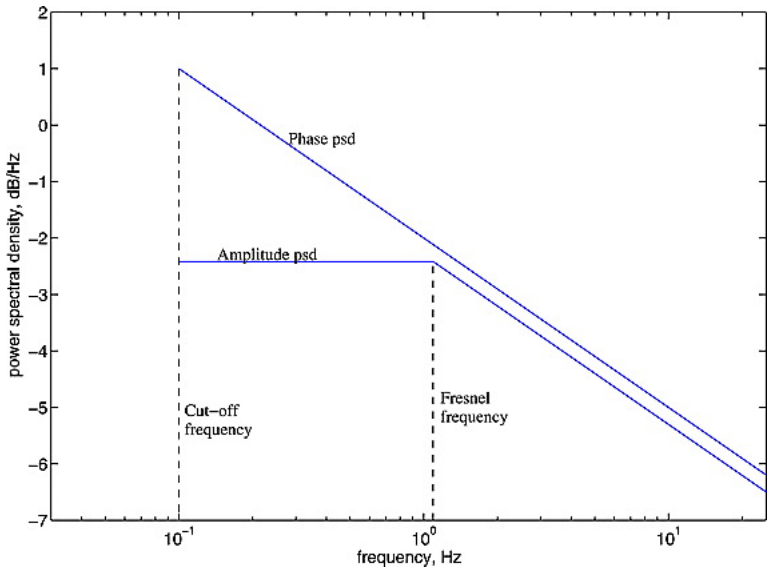

Figure 8.4: Illustration of phase and amplitude spectra [64].

of how a GPS amplitude and phase scintillation power spectra should appear is shown in Figure 8.4. In this figure, the Fresnel frequency is defined as the frequency above which a spectral roll-off is observed in amplitude spectra. It should be noted that Figure 8.4 conforms to the weak scintillation theory, discussed in Chapter 4, which indicates that

(1) The amplitude scintillation power spectra are filtered below the Fresnel frequency, while the power spectra of the phase scintillation signal are unfiltered;

(2) The value of the spectral slope for both amplitude and phase scintillation spectra is the same for frequencies above the Fresnel frequency.

As the auto-correlation function and power spectra are Fourier pairs, auto-

correlation functions that were calculated from the CHAIN data are also used to calculate power spectra of the signals. These spectra are then used to calculate the spectral index by performing a line of best fit between two manually chosen points on the spectral roll-off. Usually, this task is automated and the slope is calculated between 0.1 Hz and 10 Hz. This method of analysis cannot be performed for data at high latitudes because the ionosphere is more active causing the Fresnel frequency vary away from 0.1 Hz. Thus to make the analysis more precise, the points for slope calculations are manually chosen. Examples of power spectra of both GPS amplitude and phase signals calculated in this manner are shown in Figure 8.5.

From Figure 8.5, it can be clearly observed that the amplitude scintillation spectra (blue) are indeed filtered below a certain frequency (Fresnel frequency). They start rolling off above that frequency and are constant below that frequency. On the other hand, the phase scintillation spectra (black) are not filtered and have a constant slope for all frequencies. It is also to be noted that the spectral index of both phase and amplitude scintillation spectra is usually very similar above the Fresnel frequency. The spectral slope/index was also calculated for 1014 scintillation events under consideration, making this one of the most comprehensive studies to date of high latitude ionospheric structures using GPS.

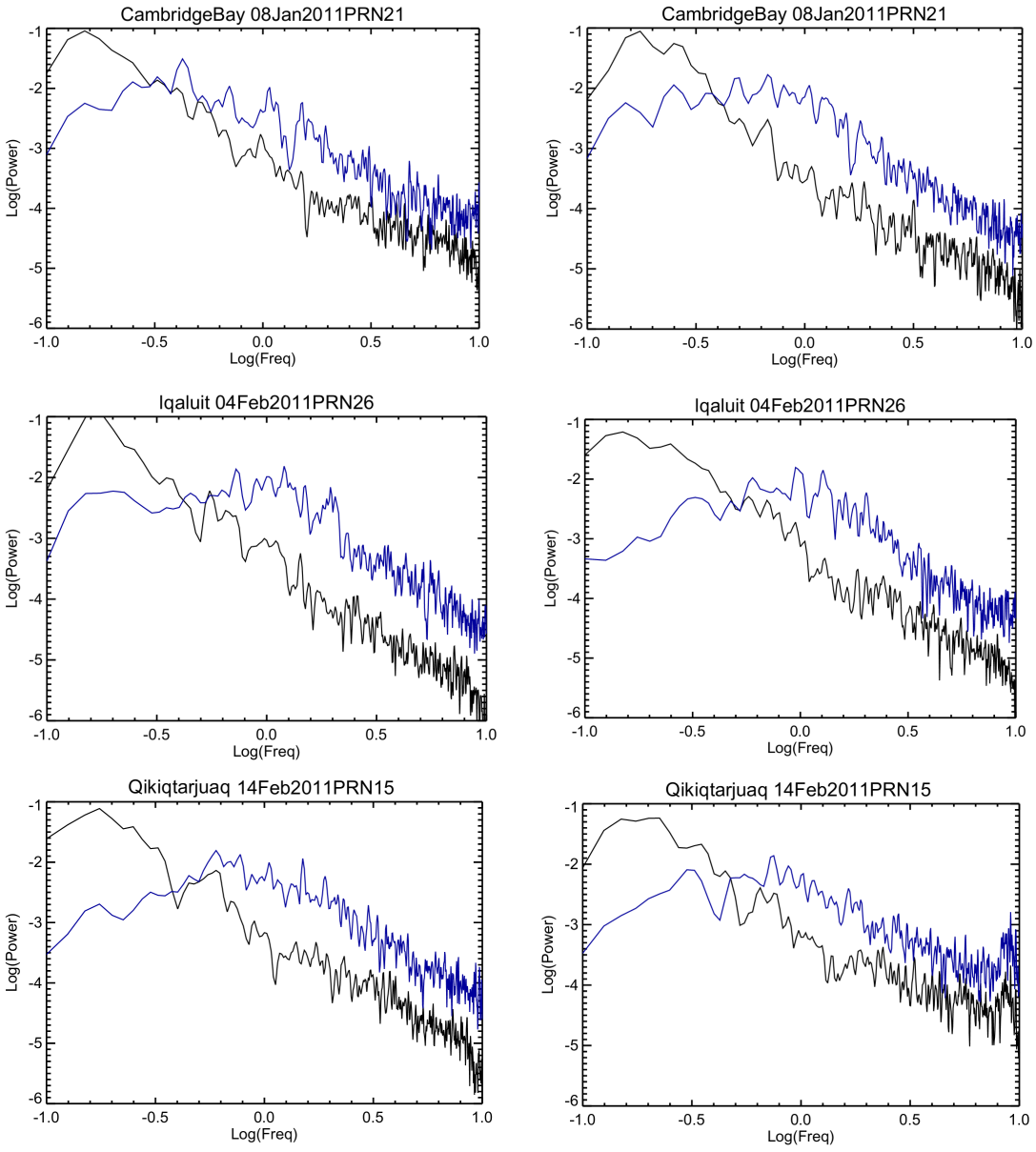

Figure 8.5: Corresponding phase (black) and amplitude (blue) scintillation spectra observed at 3 different locations and times. Fresnel filtering is clearly observed in the amplitude spectra while there is no Fresnel filtering in phase spectra.

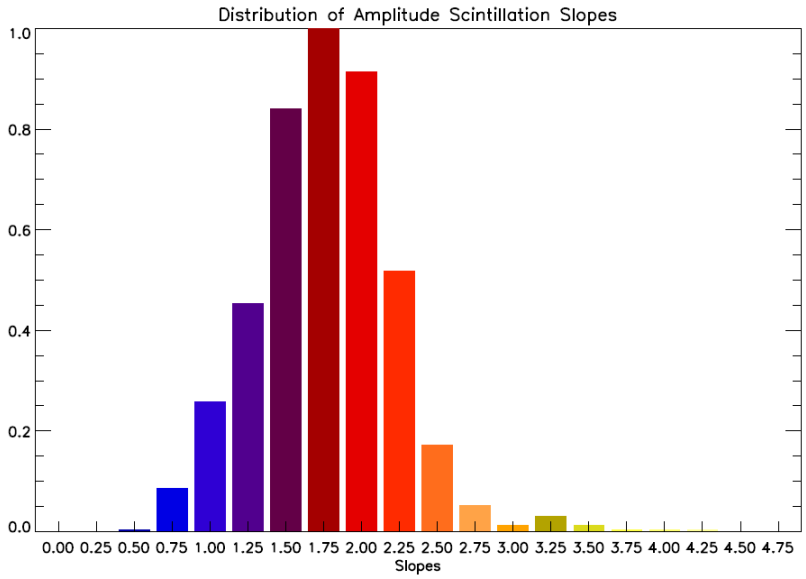

Figure 8.6: Normalized distributions of spectral indices of 1000 amplitude scintillation events obtained from CHAIN during the years 2009-2011. The average value seems to be 1.75

Distribution of Amplitude and Phase Spectral Indices

Weak scintillation theory indicates that both phase and amplitude scintillation spectra should have similar slopes [11]. To check the validity of this prediction for this particular data set from CHAIN, normalized distributions of all the amplitude and phase scintillation power spectral indices used in this stude, are calculated as shown in Figure 8.6 and Figure 8.7, respectively. It can be observed that on average the spectral index values were near 1.75 for both amplitude and phase scintillation signals.

It can also be observed that the phase scintillation spectral index distribution

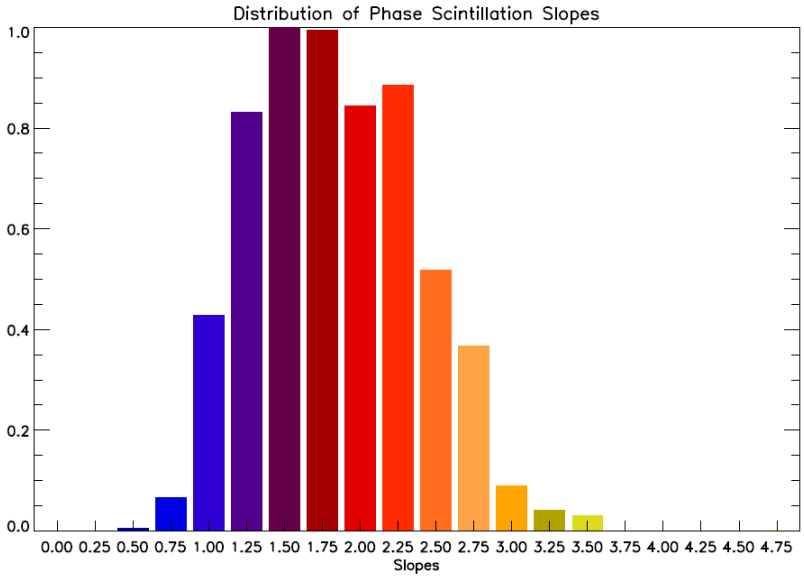

Figure 8.7: Normalized distributions of spectral indices of 1000 phase scintillation events obtained from CHAIN during the years 2009-2011. Average value seems to be around 1.75

(Figure 8.7) is broader compared to the amplitude scintillation spectral index distribution (Figure 8.6). This indicates that phase scintillation spectral indices have more variance than the amplitude scintillation spectral indices.

Relation Between Spectral Index of a Scintillation Signal and the Level of Scintillation

In order to examine how the spectral slope changes when the signal encounters irregularities, an amplitude scintillation signal which occurred at Qikiqtarjuaq on 14 February 2011 on GPS satellite PRN 14 from 17:20 UT to 17:40 UT is examined. As shown in Figure 8.8, spectral slopes were calculated at specific time intervals in order to show how a radio signal behaves when it encounters a scintillation-producing ionospheric irregularity.

Panel 8.8(a) shows the detrended amplitude scintillation signal, while the other panels 8.8(b)-8.8(f) show the power spectra of the signal (with the line of best fit(red)) during particular one minute periods. Values of the spectral index / slope of best fit line and corresponding S_4 value are also shown in the power spectra panels. Panel 8.8(b) shows the power spectra at 19:20 where there is minimum scintillation as S_4=0.029 and the slope value was observed to be -1.49. But as the scintillation level increased the slope became steeper as shown in panel 8.8(c) where S_4=0.106 and corresponding slope is -2.185. This also can be observed in panels 8.8(d)-8.8(f). In order to do a

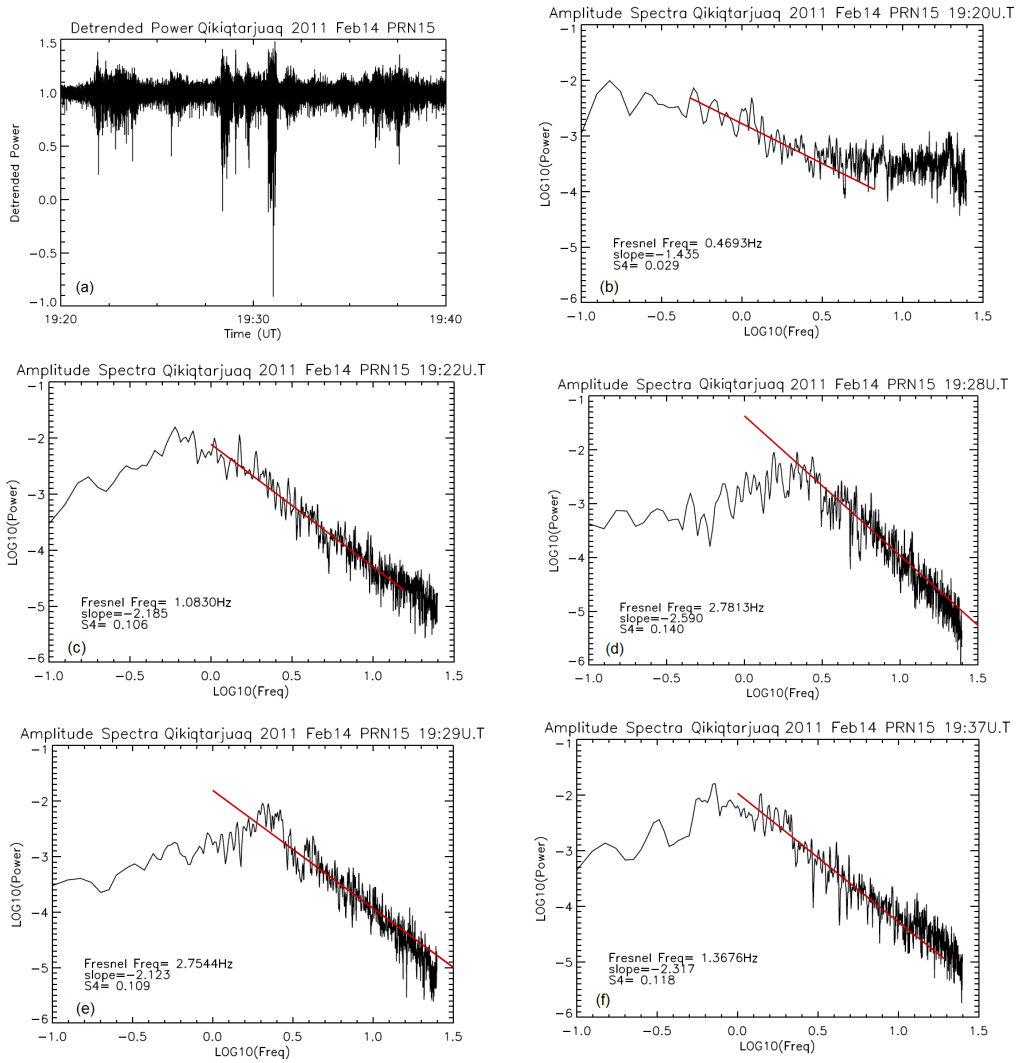

Figure 8.8: Spectral indices during scintillation; panel (a) shows the detrended amplitude scintillation signal while the other panels (b)-(f) show the power spectra of the signal (with the line of best fit in red), S_4, spectral index/slope, Fresnel frequency during those particular minutes.

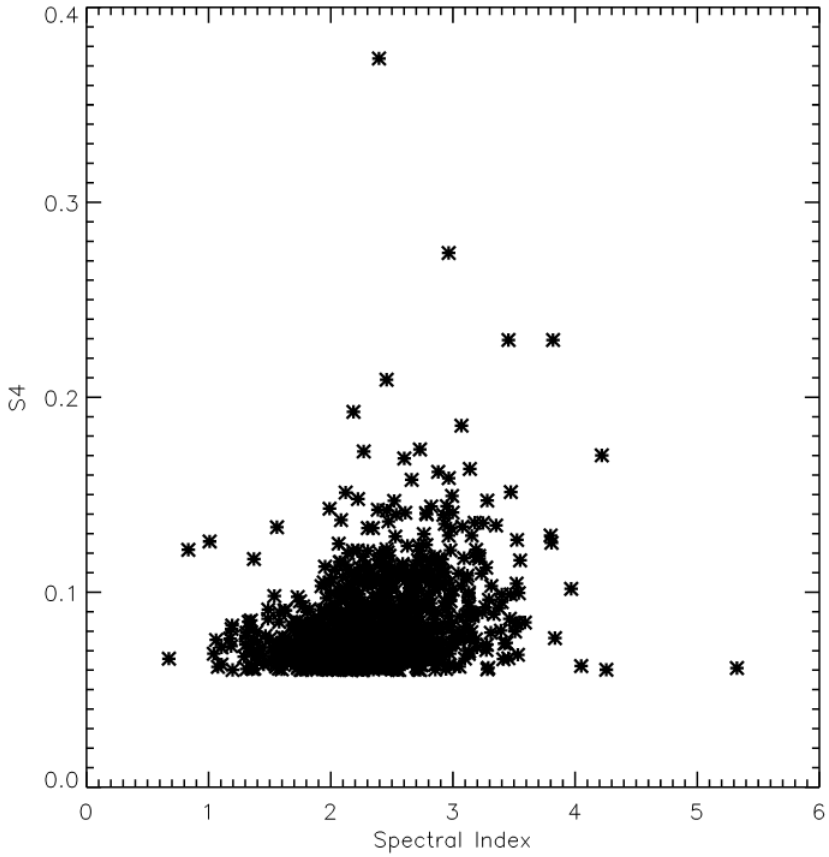

Figure 8.9: Scatter plot between S_4 and spectral index. It suggests that spectral index increases as S_4 increases.

more through correlation between S_4 and the spectral indices, a scatter plot of the spectral indices and their corresponding S_4 values for the scintillation events that are considered in this study, is shown in Figure 8.9. From this figure, there is some indication that the spectral index increases with S_4 but no clear trend is observed. From these results, it can be hypothesized that the contribution from smaller irregularities is smaller when the scintillation index is larger and hence a steeper slope is present in the spectra. Thus it is hypothesized that most of the contribution comes from irregularities near the Fresnel scale for high scintillation.

Elevation-Angle Dependence of Spectral Index

In order to investigate elevation angle dependence on the spectral index, normalized distributions of the amplitude spectral indices (calculated in this study) for every 10^o of elevation angle between 20^o and 80^o, are calculated and plotted in Figure 8.10. From panel 8.10(a) it can be observed that the average value of the spectral slope at 20^o to 30^o was around 1.5. As the elevation increased, the average value of the spectral index of the respective elevation bin also increased, as indicated in panels 8.10(b)-8.10(f). The average spectral index increased from 1.5 in panel 8.10(a) to 2.0-2.25 in panel 8.10(f). Two possible reasons with the potential for explaining these observations are the following:

1) Different irregularity mechanisms act at different elevation-angles;

2) The geometry of the ray path varies with elevation-angless

These reasons will be discussed further in the Section 8.4.

8.3.2 Fading Rate and Irregularity Scale Length

The auto-correlation functions calculated were also used to determine the fading rate of the scintillation signal [37, 3]. As shown in Figure 8.11, the fading rate can be defined as the time lag at which the auto-correlation function of the amplitude scintillation signal falls to 0.5 [37]. The fading rate gives an estimate of the scintillation fading time scales, which are useful in designing and improving scintillation prone systems.

In this analysis, the fading rate for all scintillation "minutes" considered in this study were calculated, and the normalized distribution of these rates is shown in Figure 8.12. It can be seen from Figure 8.12 that, on average, most of the spectra have a 0.1 sec decorrelation time/fading rate. Fading rate is also known as the decorrelation time. This decorrelation time can be considered to be the average time taken for the raypath of the radio signal to move across the ionospheric irregularity. Thus by multiplying the fading rate with the relative velocity, V_r, an average irregularity scale length/decorrelation distance can be calculated [32, 50]. Even though contribution to scintillation is from irregularities with different sizes, this decorrelation distance provides an estimate of the average size of the irregularities

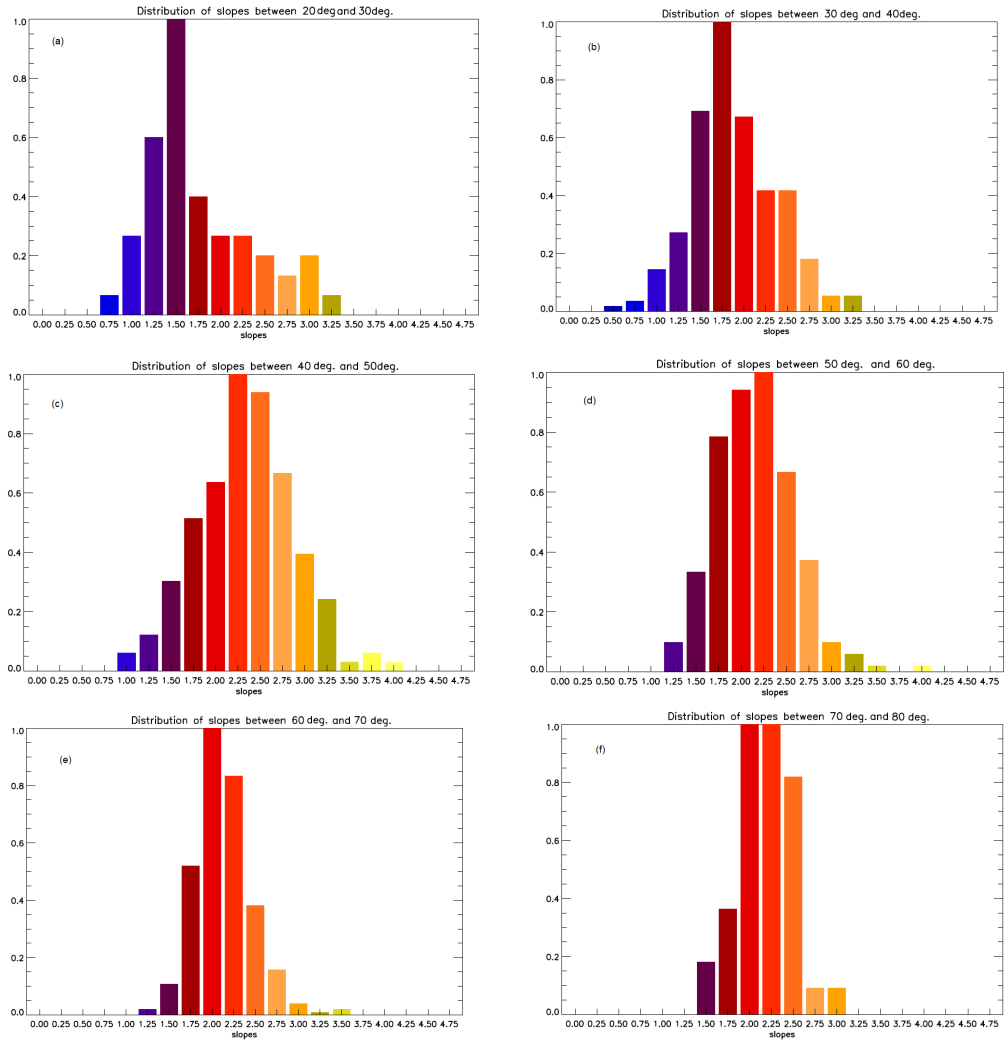

Figure 8.10: Normalized distributions of spectral slopes in specific elevation bins (10^o). There is a gradual increase in the mean spectral index as the elevation increased.

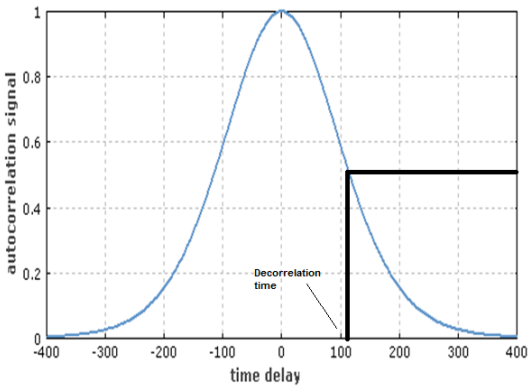

Figure 8.11: Illustration of an autocorrelation function and decorrelation time [37].

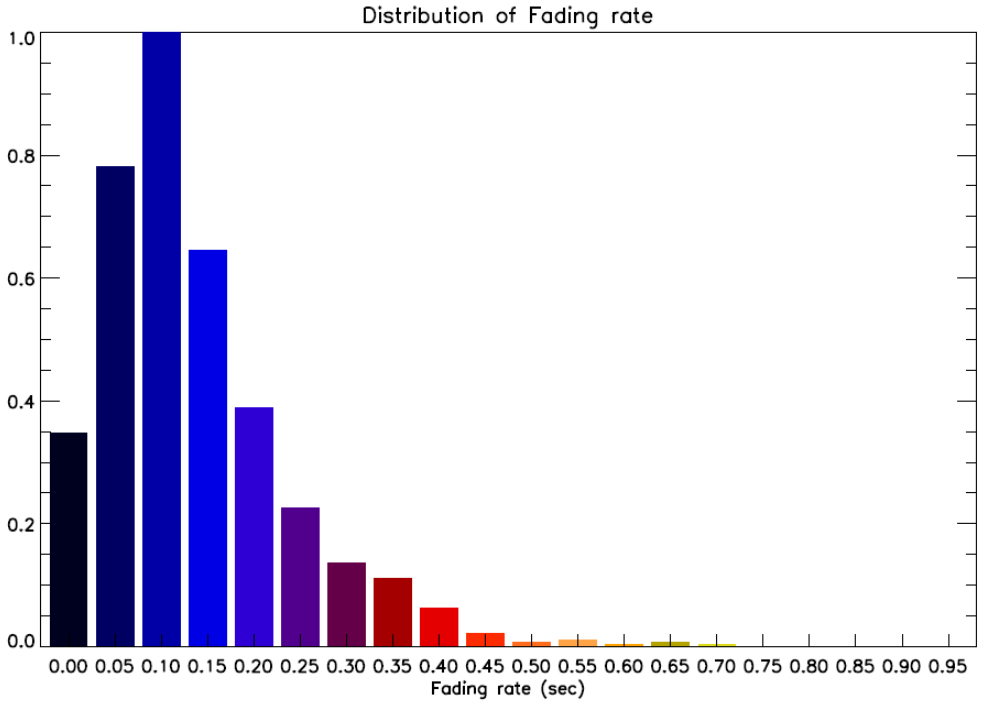

Figure 8.12: Normalized distribution of the fading rate of 1000 scintillation events obtained from CHAIN during the years 2009-2011.

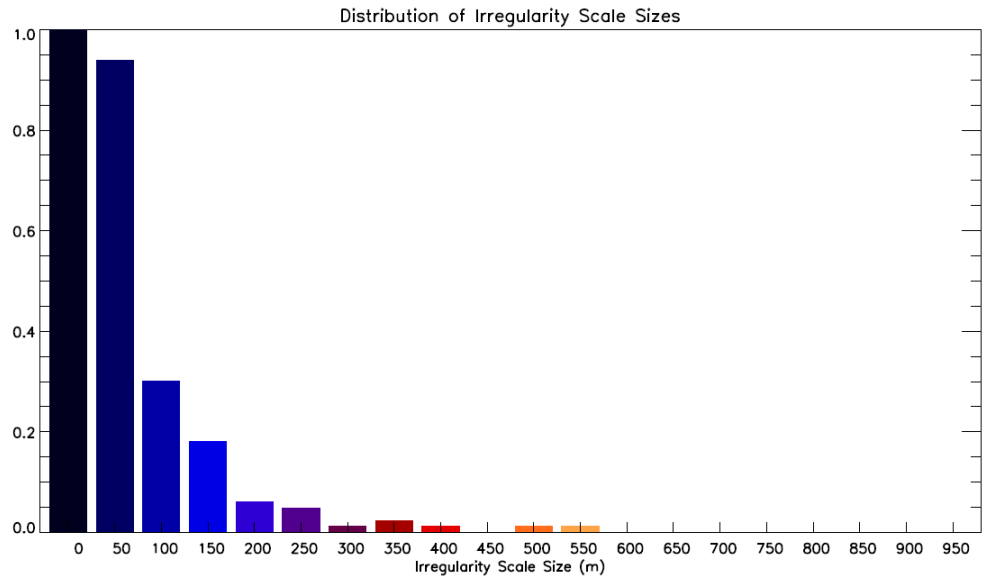

Figure 8.13: Normalized distribution of average irregularity sizes for 1000 scintillation events obtained from CHAIN during the years 2009-2011.

The distribution of the average scale size of the irregularities calculated using this method is shown in Figure 8.13. From this, it can be seen clearly that the dominant irregularity scale size is around 50 m for the scintillation events analyzed in this study.

As shown in Figure 8.14, it was also observed that the irregularity scale size increased as S_4 increased. This suggests that as the scintillation level increased, larger irregularities contribute more towards scintillation. The implications of these results will be discussed in Section 8.4.

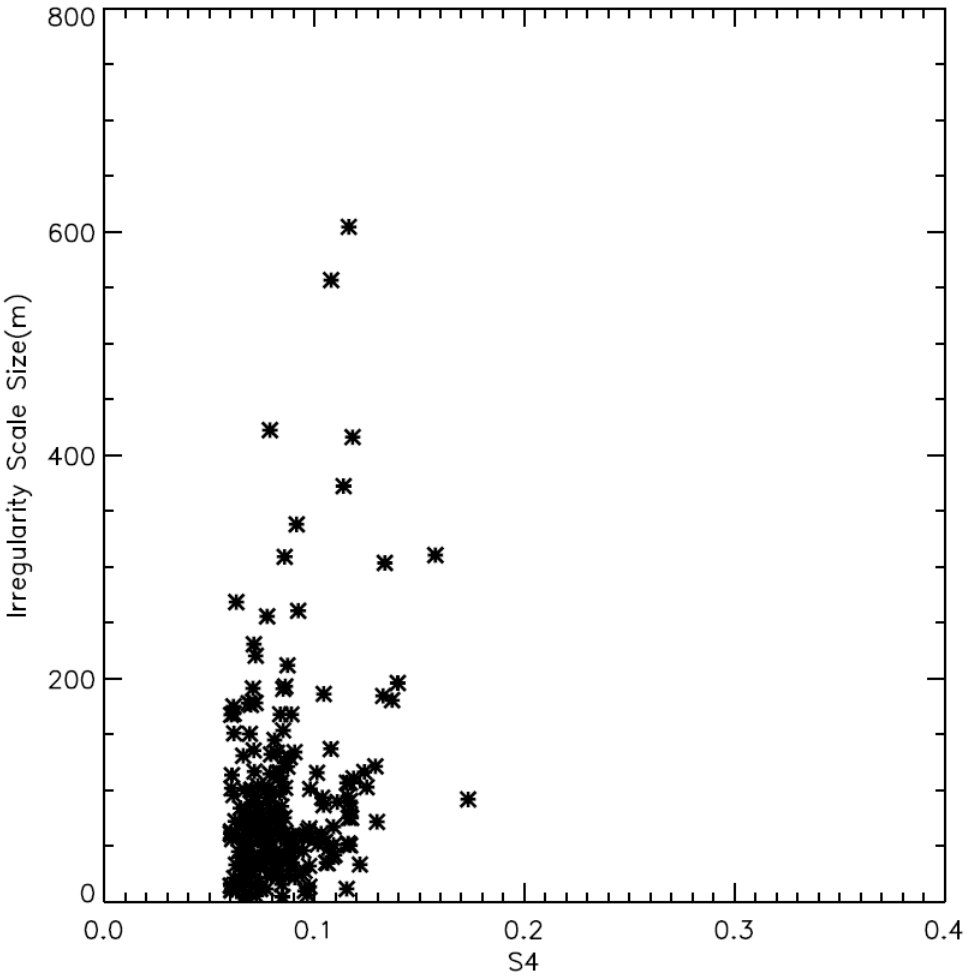

Figure 8.14: Scatter plot between S_4 and irregularity scale size. Irregularity scale size seems to increase as S_4 increases.

8.4 Discussion

From Figures 8.6 and 8.7, it can be observed that the average value of the spectral index for both GPS amplitude and phase scintillation at high latitude is around 1.75. This result supports the weak scintillation theory (Chapter 4), which predicted that both amplitude and the phase scintillation spectral indices should be equal in the weak scintillation regime ($S_4 < 0.4$). Spectral studies [6, 68, 4] of high latitude ionospheric irregularities using satellites indicate that the value of their spectral slope is around 1.8-2.4. These studies indicate that these spectral slopes support the contention that both Kelvin-Helmholtz instability and/or gradient drift instability, are the main cause for the formation of these ionospheric irregularities. An example of such a distribution of spectral indices for electron density fluctuations during gradient drift instability obtained from the DE-2 satellite for orbit number (3223) on 8 March 1982 is shown in Figure 8.15.

Despite the fact that GPS is a totally different system compared to the DE-2 satellite, these similarities in the results suggest that gradient drift instability and Kelvin-Helmholtz instability may also be the main physical processes driving the irregularity mechanisms in the high latitude ionosphere [6, 68, 4]. Further studies are needed to ascertain which physical process or processes are responsible for creating these GPS scintillation producing irregularities. The relation between the spectral index and level of scintillation can be seen

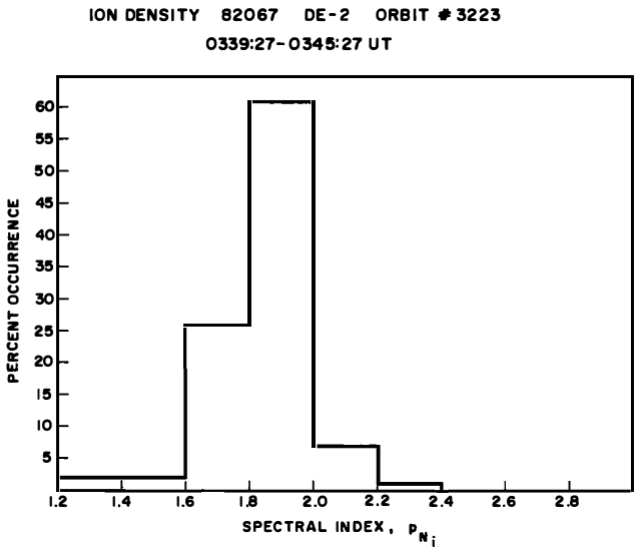

Figure 8.15: Distribution of spectral index for electron density fluctuations $\frac{\delta N}{N}$ as seen on orbit number 3223 of the DE-2 satellite on 8 March 1982 [4].

clearly from Figures 8.8 and 8.9. As the scintillation level increases, the spectral index also seems to increase. This indicates that at higher levels of scintillation, irregularities around the Fresnel scale size contribute more than smaller irregularities. Figure 8.8, it is shows that a definite power-law structure is observed at higher S_4 values.

Figure 8.10 demonstrates the elevation-angle dependence of the spectral index. It is seen that the spectral index has a lower value at lower elevations and a higher value at higher elevations. This points to two possible scenarios : 1) There are different physical mechanisms that are acting at different elevation-angles. The reason behind this scenario is that a different slope/spectral index is observed at different elevations and, as mentioned before, different

values of the slope/spectral index indicate different physical mechanisms.
2) At lower elevation-angles the contributions of smaller irregularities were greater than that higher elevation-angles. The possible reason for this second scenario, as shown in Figure 8.16, is that when the signal is at a lower elevation (blue), it has to go through a larger portion of the ionosphere compared to the signal that is at higher elevation (red). This would mean that when the signal is at a lower elevation angle, there is a greater probability of the signal encountering smaller irregularities than at higher elevation-angles simply because the signal stays for a longer time in the ionosphere. This would lead to greater contribution of smaller irregularities into the spectra that in turn would make the slope shallow at low elevations compared to higher elevation.

Also, from Figure 8.14, it was observed that as the scintillation intensity (S_4) increased, the irregularity scale size also increased. This result strengthens the hypothesis put forward in Figures 8.8 and 8.9 which showed that the low scintillation spectra had shallow slopes. This indicates a greater contribution of smaller irregularities to the spectra, while during high scintillation, most of the contribution comes from larger irregularities around the Fresnel scale.

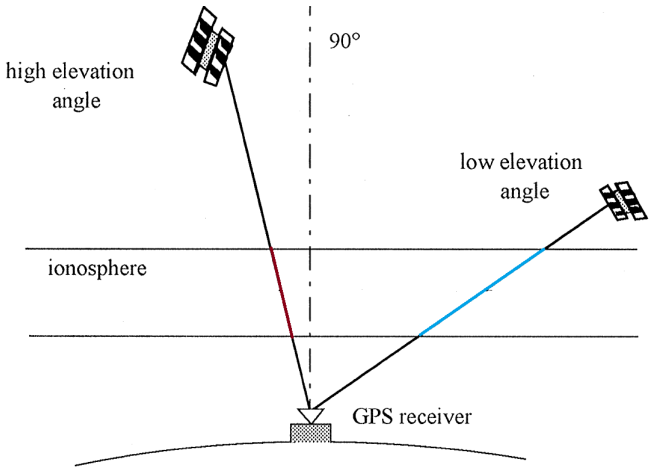

Figure 8.16: Illustration of path difference between identical ray paths with different elevation angles. Lower elevation ray paths transverse longer distance in the ionosphere compared to higher elevation ray paths. Picture Edited from [43]

8.5 Conclusion

Using the spectral analysis of the data from CHAIN, it is seen that the power spectra of the phase and amplitude scintillation follow a power-law structure indicating that the power spectra of the ionospheric irregularities in the high latitude region also follow a similar one. These results strengthen the argument that the irregularity structures in the ionosphere follow a power-law structure rather than being Gaussian [75, 68]. It is also seen from Figure 8.5 that indeed amplitude scintillation spectra are filtered for frequencies below the Fresnel frequency, while the phase scintillation spectra are not affected. This is an important result because it proves that the GPS scintillation data from high latitudes support the weak-scintillation theory when $S_4 < 0.4$. The

weak scintillation theory also predicts that the spectral index of both amplitude and phase scintillation should be very similar. It was indeed observed from the distribution analysis (Figures 8.6 and 8.7) that the average value of the spectral index for both GPS amplitude and phase scintillation index was close to 1.75.

Elevation-angle dependence (Figure 8.10) of the spectral indices seems to suggest that there may be different mechanisms producing scintillation at different elevation-angles and/or the contribution from small-scale irregularities is greater at lower elevations. This has to be further investigated taking into account possible sources of error like the change in the satellite velocity due to change in geometry. Distributions of fading rate (Figure 8.12) and average irregularity size (Figure 8.13) indicate that weak scintillation at high latitudes occurs mainly because of small-scale irregularities (mostly around 50 m) present in the ionosphere. As the intensity of these scintillations increases, most of the contribution comes from larger Fresnel-sized irregularities.

This comprehensive analysis of the GPS scintillation at high latitudes also gives an insight into the processes that create these irregularities. These results are very important as they indicate that one can use weak scintillation theory along with these results to more precisely model GPS scintillation at high latitudes. Furthermore, one can better understand the physical mecha-

nisms that create scintillation in high latitudes.

Chapter 9

Conclusion and Future Work

9.1 Summary

Scintillation indices are used to represent scintillation quantitatively, as well as being used to create scintillation models and scintillation climatologies. These models are used to understand scintillation-producing irregularities, as well as help predict and mitigate scintillation effects on satellite navigation and communication systems. Thus accuracy and validity of scintillation indices are very important. It has been shown in this thesis, how improper detrending of scintillation data can introduce errors like "phase scintillation without amplitude scintillation" events. As shown in Chapter 6, a detrending filter based on wavelets was introduced that out performs the default Butterworth filter present in the receiver. By using the wavelet filter for detrending, the "phase scintillation without amplitude scintillation" events

significantly decreased. The correlation between the wavelet-derived phase and amplitude scintillation indices was 0.79 compared to 0.58, which was the correlation coefficient for the Butterworth-derived phase and amplitude scintillation indices.

A new phase scintillation index, σ_{CHAIN}, to quantify high latitude GPS scintillation was also introduced in this thesis. The problems with the default phase scintillation index, σ_{ϕ}, were described and the reason for introducing σ_{CHAIN} was justified. From Chapter 6, it can be observed that the wavelet-derived σ_{CHAIN} performs much better than the wavelet-derived σ_{ϕ} with the correlation coefficient between wavelet-derived S_4 and wavelet-derived σ_{CHAIN} being as high as 0.90.

This wavelet-filtering technique is used to detrend GPS data from the CHAIN network for the years March 2009 to March 2011. Due to the vast amount of data, the parallel computing facility on the Atlantic Computational Excellence Network (ACEnet) was used to process the data. This wavelet-detrended data was used to calculate S_4 and σ_{CHAIN}.

In order to examine the spatial and temporal variations of scintillation occurrence at high latitudes, the wavelet-derived S_4 and σ_{CHAIN} for the years March 2009 to March 2011 were used to create scintillation climatologies. It was seen that most of the scintillation in the Polar cap occurs in the cusp

region (75^0 MLAT-85^0 MLAT) around local noon. The ionospheric irregularities formed in the cusp region due to the precipitation of electrons through the open field lines are thought to be one of the main cause of this feature. Strom enhanced densities or plasma convection into the cusp may also cause enhanced scintillation in the cusp at local noon [20]. A seasonal variation in the scintillation occurrence was also observed in the polar cap with a high occurrence of scintillation in winter and a low occurrence of scintillation in summer. This seasonal variation is attributed to the fact that in summer, there is sun all day long at these latitudes and hence photoionization is high. This results in the background ionosphere having higher densities compared to winter. This high background density quells the ionospheric gradients from being formed in the ionosphere and hence supresses scintillation. The scenario is the exact opposite in winter when there is sunlight. As a result precipitated electrons at the cusp can form gradients which in turn cause scintillation. The climatology of TEC gradients shown in Chapter 7 show similar results proving the above hypothesis given for the seasonal variations.

The characteristics of scintillation signals like the spectral slope, fading rate, and characteristic size of the irregularities were analyzed in Chapter 8. The spectral slope of both amplitude scintillation and phase scintillation appear to be 1.8-2.2. These results agree with the weak scintillation theories that suggest that the spectral index of both amplitude and phase scintillation spectra should be similar for frequencies above Fresnel frequencies. The ele-

vation angle dependence of spectral indices was also analyzed. Lower spectral indices were observed at lower elevation compared to higher elevation. These observation suggest two hypotheses, 1) Different phenomenan are contributing to scintillation at different elevations; 2) There is a greater contribution of smaller irregularities at lower elevation because the ray path spends more time in the ionosphere at low elevations compared to higher elevations. The average characteristic size of the irregularities for weak scintillation observed at high latitudes was found to be around 50 m.

9.2 Major Results

1) Technical Contribution : A new wavelet filter was designed for detrending high latitude GPS scintillation signals and a new phase scintillation index, σ_{CHAIN}, was introduced as a better choice over convential phase scintillation indices at high latitudes.

2) Phase Scintillation without Amplitude Scintillation: These artifacts, which are due to improper detrending methods, were totally removed by using the wavelet- detrending filter and σ_{CHAIN}. The correlation between amplitude scintillation index (S_4) and phase scintillation index (σ_{CHAIN}) was as high as 0.90.

3) Equal Probability of Amplitude and Phase Scintillation: Scintillation cli-

matologies produced by using wavelet-derived S_4 and σ_{CHAIN} show equal probability of amplitude and phase scintillation occurrence both spatially and temporally unlike other scintillation climatologies produced at high latitudes.

4) Spectral Studies of High Latitude Scintillation : Spectral indices of both GPS amplitude and phase scintillations are 1.75 and the average characteristic size of the irregularities was found to be around 50 m.

9.3 Future Work

9.3.1 High Latitude Scintillation Models

This study can be considered as the first step towards creating a high latitude scintillation model [63]. To date, there is no high latitude specific scintillation model created using just GPS data. The results from this work combined with results obtained by using data from solar maximum could be used to create a high latitude specific scintillation model which in turn can be joined to the mid and low latitude scintillation models to create a complete worldwide scintillation model. As indicated in this thesis, the data used in this work was taken when the solar activity is minimum. From 2012, the sun is slowly "waking up" and it is predicted to reach maximum in late 2013. The data from solar maximum should also be analyzed. This would not only help understand the effect of the solar activity on the ionosphere but

also help in creating high latitude scintillation models which are much more robust. Given the importance of the high latitude region both strategically and economically, a high latitude scintillation model would be very useful for navigation and communications in these regions.

9.3.2 Ionospheric Drift Calculations

Ionospheric drift velocity is an important variable to know for understanding the ionosphere and is also a key indicator of space weather. The most common means of finding ionospheric drift velocity is by using ionosondes or by installing GPS receivers, which are suitably close to each other. This means that there is a need for extra infrastructure to obtain ionospheric drift. Fresnel frequency determinations obtained from power spectra of amplitude scintillation can provide an estimate about the ionospheric drift, given knowledge of the ionospheric shell height, satellite velocity at that height, and the wavelength of the satellite's signal. By creating a data-base of ionosonde-derived ionospheric drift velocities, corresponding shell heights, Fresnel frequencies from scintillation data obtained from co-located GPS receivers, and space weather indices, a relation between Fresnel frequency and drift velocity could be obtained. This relation then would be useful for estimating the ionospheric drift by just using the Fresnel frequency obtained from the spectra of GPS amplitude scintillation.

9.3.3 Future is Unlimited

CHAIN being the only high latitude GPS network with co-located ionosondes is an important asset to the scientific community. With the approval of CHAIN's expansion, where the addition of 15 more GPS receivers is planned, immense scientific opportunities would be created that would help in better understanding of the high latitude ionosphere as well as its effect on GPS signals. These new GPS receivers can be used to find the ionospheric drift using correlation analysis that can be compared with ionosonde-derived drift and spectra-derived drift. Another important investigation that could be started is the real-time implementation of the wavelet filter. The wavelet filter introduced in this dissertation has so far been used as a post-processing tool. Real-time implementation of this filter in a GPS receiver would be a interesting project as it has both scientific and industrial applications. In the next few years, CHAIN could provide one of the largest databases of high latitude GPS scintillation data from both solar maxima and minima. These databases then can be used to create much larger collections of scintillation statistics that would help in better understanding the high latitude ionosphere.

Bibliography

[1] J. Aarons, *Global Morphology of Ionospheric Scintillations*, Proceedings of IEEE **70** (1982), 324–360, doi:10.1109/PROC.1971.8122.

[2] K. B. Baker and S. Wing, *A New Magnetic Coordinate System for Conjugate Studies at High Latitudes*, Journal of Geophysical Research **94** (1989), 9139–9143, doi:10.1029/JA094iA07p09139.

[3] S. Banola, B. M. Pathan, D. R. K. Rao, and H. Chandra, *Spectral Characteristic of Scintillation Producing Ionospheric Irregularities in Indian Region*, Earth Planets Space **57** (2005), 47–59.

[4] S. Basu, S. Basu, and E. MacKenzie et al., *Plasma Structuring by the Gradient Drift Instability at High Latitudes and Comparison with Velocity Shear Driven Processes*, Journal of Geophysical Research **95(A6)** (1990), 7799–7818, doi:10.1029/JA095iA06p07799.

[5] S. Basu, S. Basu, and E. Mackenzie, *Morphology of Phase and Intensity Scintillations in Auroral Oval and Polar Cap*, Radio Science **20(3)** (1985), 347–356, doi:10.1029/RS020i003p00347.

[6] S. Basu, S. Basu, E. Mackenzie, P. F. Fougere, W. R. Coley, N. C. Maynard, J. D. Winningham, M. Sugiura, W. B. Hanson, and W. R. Hoegy, *Simulataneous Density and Electric Field Fluctuation Spectra Associtaed with Velocity Shears in the Auroral Oval*, Journal of Geophysical Research **93(A1)** (1988), 115–136, doi:10.1029/JA093iA01p00115.

[7] S. Basu, E. Mackenzie, and S. Basu, *Ionospheric Constraints on VHF/UHF Communication Links During Solar Maximum and Minimum Periods*, Radio Science **23(3)** (1988), 363–378, doi:10.1029/RS023i003p00363.

[8] S. Basu, E. MacKenzie, and S. Basu et al., *250 MHz/GHz Scintillation Parameters in the Equatorial, Polar and Auroral Environments*, IEEE Journal on Selected Areas in Communication **SAC-5(2)** (1987), 102–114, doi:10.1109/JSAC.1987.1146533.

[9] T. L. Beach, *Global Positioning System Studies of Equatorial Scintillations*, Ph.D. thesis, Cornell University, USA, 1998.

[10] T. L. Beach, *Perils of the GPS Phase Scintillation Index(σ_ϕ)*, Radio Science **41** (2006), RS5S31, doi:10.1029/2005RS003356.

[11] A. Bhattacharyya, T. L. Beach, S. Basu, and P. M. Kintner, *Nightime Equatorial Ionosphere:GPS Scintillations and Diffrential Carrier Phase Fluctuations*, Radio Science **35(1)** (2000), 209–224, doi:10.1029/1999RS002213.

[12] J. Butcher, *Canadian Advanced Digital Ionosonde (cadi) User Manual*, Scientific Instrumentation Ltd., 2007.

[13] S. Chapman, *The Absorption and Dissociative or Ionizing Effect on Monochromatic Radiation in an Atmosphere on a Rotating Earth*, Proceeding of the Physical Soc. **43(1)** (1931), 26–45, doi:10.1088/0959-5309/43/1/305.

[14] W. M. Cronyn, *The Analysis of Radio Scattering and Space-Probe Observations of Small-Scale Structure in the Interplanetary Medium*, The Astrophysical Journal **161** (1970), 755–763, 10.1086/150576.

[15] A. J. Van Dierendonck, J. Klobuchar, and Q. Hua, *Ionospheric Scintillation Monitoring using Commercial Single Frequency C/A Code Receivers.*, Proceedings of ION GPS-93 (1993), 333–334.

[16] M. Farge, *Wavelet Transforms and their Applications to Turbulence*, Annual reviews of fluid mechanics **24** (1992), 395–457, 10.1146/annurev.fl.24.010192.002143.

[17] B. Forte, *Optimum Detrending of Raw GPS Data for Scintillation Measurements at Auroral Latitudes*, Journal of Atmospheric and Terrestial Physics **67(12)** (2005), 1100–1109, doi:10.1016/j.jastp.2005.01.011.

[18] B. Forte, M. Materassi, L. Alfonsi, V. Romano, G. De Franceschi, and P. Spalla, *Optimum Parameter for Estimating Phase Fluctuations on*

Transionospheric Signals at High Latitudes, Advances in Space Research **47(2)** (2010), 21882193, doi:10.1016/j.asr.2010.04.033.

[19] B. Forte and S. M. Radicella, *Problems in Data Treatment for Ionospheric Scintillation Measurement*, Journal of Atmospheric and Solar-Terrestial Physics **37(6)** (2002), 1096, doi:10.1029/2001RS002508.

[20] J. C. Foster, A. J. Coster, P. J. Erickson, F. J. Rich, and B. R. Sandel, *Stromtime Observations of the Flux of Plasmaspheric Ions to the Dayside Cusp/Magnetopause*, Geophysical Research Letters **31** (2004), L08809, doi:10.1029/2004GL020082.

[21] E. J. Fremouw, R. L. Leadabrand, R. C. Livingston, M. D. Cousins, C. L. Rino, B. C. Fair, and R. A. Long, *Early Results from the DNA Wide-Band Satellite Experiment - Complex-Signal Scintillation*, Radio Science **13(1)** (1978), 167–187, doi:10.1016/j.jastp.2005.01.011.

[22] C. Frohlich, *Evidence of a Long-Term Trend in Total Solar Irradiance*, Astronomy and Astrophysics **501** (2009), L27–L30, doi:10.1051/0004-6361/200912318.

[23] M. Gola, A. W. Wernik, S. J. Franke, C. H. Liu, and K. C. Yeh, *Behaviour of HILAT Scintillation over Spitsbergen*, Journal of Atmospheric and Terrestrial Physics **54(9)** (1992), 12071213, doi:10.1016/0021-9169(92)90146.

[24] Satellite-Based Augmentation Systems Ionospheric Working Group, *Ionospheric scintillations: How irregularities in electron density peturb satellite navigation systems*, GPS World **23(4)** (2012), 44–50.

[25] T. R. Hartz, *Radio Star Scintillations and the Ionosphere*, Canadian Journal of Physics **33** (1955), 476–482, doi:10.1139/p55-057.

[26] W. J. Heikkila and J. D. Winningham, *Penetration of Magnetosheath Plasma to Low Altitudes through the Dayside Magnetospheric Cusps*, Journal of Geophysical Research **76(4)** (1971), 883, doi:10.1029/JA076i004p00883.

[27] J. S. Hey, S. J. Parsons, and J. W. Phillips, *Fluctuations in Cosmic Radiations at Radio Frequencies*, Nature (London) **158** (1946), 247, doi:10.1038/158234a0.

[28] I. Horvath and S. Crozier, *Software Developed for Obtaining GPS-Derived Total Electron Content Values*, Radio Science **42** (2007), RS2002, doi:10.1029/2006RS003452.

[29] X. Huang and B. W. Reinisch, *Vertical Electron Content from Ionograms in Real Time*, Radio Science **36(2)** (2001), 335, doi:10.1029/1999RS002409.

[30] R. D. Hunsucker and J. K. Hargreaves, *The High-Latitude Ionosphere and its Effects on Radio Propagation*, Cambridge University Press, New York, NY, USA, 2003.

[31] P. T. Jayachandran, R. B. Langley, J. W. MacDougall, and S. C. Mushini et al., *Canadian High Arctic Ionospheric Network*, Radio Science **44** (2009), RS0A03, doi:10.1029/2008RS004046.

[32] J. L. Jespersen and George Kamas, *Satellite Scintillation Observations at Boulder, Colorado*, Journale of Atmospheric and Terrestrial Physics **26** (1964), 457–473, doi:10.1016/0021-9169(64)90027-3.

[33] I. L. Jones, *Further Observations of Radio Stellar Scintillation*, Journal of Atmospheric and Terrestial Physics **19** (1960), 26–36, doi:10.1016/0021-9169(60)90104-5.

[34] G. Kaiser, *A Friendly Guide to Wavelets*, Springer Publications, Natick,MA, USA, 1994.

[35] D. Kenneth, *Ionospheric Radio*, IEE Electromagnetic Wave Series, 31, Peter Peregrinus Ltd., 1990.

[36] G. S. Kent, *High Frequency Fading Observed on the 40Mc/s Wave Radiated from Artificial Satellite 1957a*, Journal of Atmosphere and Terrestrial Physics **16** (1959), 10–20, doi:10.1016/0021-9169(59)90003-0.

[37] P. M. Kintner and H. Kil, *Fading Timescales Associated with GPS Signals and Potential Consequences*, Radio Science **36(4)** (2001), 731–743, doi:10.1029/1999RS002310.

[38] M. G. Kivelson and C. T. Russel, *Introduction to Space Physics*, Cambridge University Press, New York, USA., 1995.

[39] J. A. Klobuchar, *Ionospheric Effects on GPS, in Global Positioning Systems: Theory, Applications, Vol 2*, Progress in astronautics and aeronautics, Vol 164, American Institute of Aeronautics and Astronautics, 1996.

[40] A. Komjathy, *Global Ionospheric Total Electon Content Mapping using Global Positioning System*, Ph.D. thesis, Dept. of. GGE, University of New Brunswick, Canada, 1997.

[41] C. L.Rufenach, *Power-Law Wavenumber Spectrum Deduced from Ionospheric Scintillation Observation*, Journal of Geophysical Research **77(25)** (1972), 4761–4772, doi:10.1029/JA077i025p04761.

[42] J. MacDougall and P. T. Jayachandran, *Polar Patches : Auroral Zone Precipitation Effects*, Journal of Geophysical Research **112(A5)** (2007), A05312, doi:10.1029/2006JA011930.

[43] J. L. Martinez, M. A. Martinez, and A. Garcia-Cerezo, *New Method of Generating Differential GPS Corrections*, Control Engineering Practice **8** (2000), 253–258.

[44] M. Materassi and C. N. Mitchell, *Wavelet Analysis of GPS Amplitude Scintillatin: A Case Study*, Radio Science **42** (2007), RS1004, doi:10.1029/2005RS003415.

[45] L. A. McKinnell, B. Opperman, and P. J. Cilliers, *GPS TEC and Ionosonde TEC over Grahamstown, South Africa: First Com-*

parisons, Advances in Space Research **39(5)** (2007), 816–820, doi:10.1016/j.asr.2006.10.018.

[46] M. Misiti, Y. Misiti, G. Oppenheim, and J.M. Poggi, *Wavelet Toolbox for use with Matlab*, The MathWorks Inc., Natick,MA, USA, 1996.

[47] S. C. Mushini, P. T. Jayachandran, R. B. Langley, J. W. MacDougall, and D. Pokhotelov, *Improved Amplitude- and Phase-Scintillation Indices Derived from Wavelet Detrended High Latitude GPS Data*, GPS solutions **16(3)** (2012), 363–373, doi:10.1007/s10291-011-0238-4.

[48] P. T. Newell, R. A. Greenwald, and J. M. Ruohoniemi, *The Role of the Ionosphere in Aurora and Space Weather*, Reviews of Geophysics **39(2)** (2001), 137149, doi:10.1029/1999RG000077.

[49] P. T. Newell and C. Meng, *Mapping the Dayside Ionosphere to the Magnetosphere According to Particle Precipitation Characteristics*, Geophysical Research Letters **19(6)** (1992), 609612, doi:10.1029/92GL00404.

[50] K. Patel, A. K. Singh, R. P. Patel, and R. P. Singh, *Ionospheric Scintillations by Sporadic-E Irregularities over Low Latitude*, Bulletin of Astronomical Society of India **35** (2007), 625–630.

[51] P. Prikryl, P. T. Jayachandran, S. C. Mushini, and R. Chadwick, *Climatology of GPS Phase Scintillation and HF Radar Backscatter for the High Latitude Ionosphere under Solar Minimum Conditions*, Annales Geophysicae **29(2)** (2011), 377–392, doi:10.5194/angeo-29-377-2011.

[52] B. W. Reinish, J. L. Scali, and D. M. Haines, *Ionospheric Drift Measurements with Ionosondes*, Annali di Geofisica **41** (1998), 5–6, doi:10.4401/ag-3812.

[53] W. Rideout and A. Coster, *Automated GPS Processing for Global Electron Content Data*, GPS Solutions **10(3)** (2006), 219–228, doi:10.1007/s10291-006-0029-5.

[54] C. L. Rino, *Ionospheric Scintillation Theory- A Mini-Review*, IEEE Transactions of Antennas and Propagation **24(6)** (1976), 912–915, doi:10.1109/TAP.1976.1141439.

[55] C. L. Rino, *A Power Law Phase Screen Model for Ionospheric Scintillation 1.Weak Scatter*, Radio Science **14(6)** (1979), 1135–1145, doi:10.1029/RS014i006p01135.

[56] C. L. Rufenach, *A Radio Scintillation Method of Estimating the Small-Scale Structure in the Ionosphere*, Journal of Atmospheric and Terrestial Physics **33** (1971), 1941–1951, doi:10.1016/0021-9169(71)90170-X.

[57] V. H. Rumsey, *Scintillations due to a Concentrated Layer with a Power-Law Turbulence Spectrum*, Radio Science **10(1)** (1975), 107–114, 10.1029/RS010i001p00107.

[58] J. A. Secan, R. M. Bussey, E. J. Fremouw, and S. Basu, *An Improved Model of Equatorial Scintillation*, Radio Science **30** (1995), 607–617, doi:10.1029/94RS03172.

[59] J. A. Secan, R. M. Bussey, E. J. Fremouw, and S. Basu, *High Latitude Upgrade to the Wide Band Ionospheric Scintillation Model*, Radio Science **32** (1997), 1567–1574, doi:10.1029/97RS00453.

[60] S. G. Sheperd and J. M. Ruohoniemi, *Electrostatic Potential Patterns in the High-Latitude Ionosphere Constrained by SuperDARN Measurements*, Journal of Geophysical Research **105(A10)** (2000), 23005, doi:10.1029/2000JA000171.

[61] D. G. Singleton, *Power Spectra of Ionospheric Scintillation*, Journale of Atmospheric and Terrestrial Physics **36** (1974), 113–133, doi:10.1016/0021-9169(74)90071-3.

[62] F. G. Smith, C. G. Little, and A. C. B. Lovell, *Origin of the Fluctuations in the Intensity of Radio Waves from Galactic Sources*, Nature **165** (1950), 422–424, doi:10.1038/165422a0.

[63] L. Spogli, L. Alfonsi, G. De Franceschi, V. Romano, M. H. O. Aquino, and A. Dodon, *Climatology of GPS Ionospheric Scintillation over High and Mid-Latitude European Regions*, Annales Geophysicae **27(9)** (2009), 3429–3437, doi:10.5194/angeo-27-3429-2009.

[64] H. J. Strangeways, Y. H. Ho, M. H. O. Aquino, Z. G. Elmas, H. A. Marques, J. F. G. Monico, and H. A. Silva, *On Determining Spectral Parameters, Tracking Jitter, and Gps Positioning Improve-*

ment by Scintillation Mitigation, Radio Science **46** (2011), RS0D15, doi:10.1029/2010RS004575.

[65] J. H. Strangeways, *Determining Scintillation Effects on GPS Receivers*, Radio Science **44** (2009), RS0A36, doi:10.1029/2008RS004076.

[66] J. E. Titheridge, *Ionogram Analysis: Least Squares Fitting of Chapman-Layer Peak*, Radio Science **20(2)** (1985), 247–256, doi:10.1029/RS020i002p00247.

[67] C. Torrence and G. P. Compo, *A Practical Guide to Wavelet Analysis*, Bulletin of the American Meteorological Society **79** (1998), 69–78.

[68] Roland T. Tsunoda, *High-Latitude F Region Irregularities: A Review and Synthesis*, Reviews of Geophysics **26(4)** (1988), 719–760, doi:10.1029/RG026i004p00719.

[69] R. Umeki, C. H. Liu, and K. C. Yeh, *Multifrequency Studies of Ionospheric Scintillation*, Radio Science **12(2)** (1977), 311–317, doi:10.1029/RS012i002p00311.

[70] C. Watson, *GPS TEC and Riometer Techniques for Observing Absorption Events in the High Latitude Ionosphere*, Master's thesis, Dept. of Physics, University of New Brunswick, Canada, 2011.

[71] D. Wells, N. Beck, D. Delikaraolou, A. Kleusberg, E. J. Krakiwsky, G. Lachapelle, R. B. Langley, M. Nakiboglu, Klaus-Petere Schwarz,

J. M. Tranquilla, and P. Vanicek, *Guide to GPS Positioning*, Canadian GPS Associates, Fredericton, New Brunswick, Canada., 1986, Reprinted as Department of Geodesy and Geomatics Engineering Lecture Note No:58, University of New Brunswick, Fredericton, New Brunswick, Canada.

[72] A. W. Wernik, L. Alfonsi, and M. Materassi, *Ionospheric Irregularities, Scintillation and its Effect on Systems*, Acta Geophysica Polonica **52(2)** (2004), 237–249.

[73] A. D. Wheelon, *Electromagnetic Scintillation 1. Geometrical Optics*, Cambridge University Press, Cambridge, UK, 2004.

[74] K. C. Yeh and C. H. Liu, *Propagation and Application of Waves in the Ionosphere*, Reviews of Geophysics and Space Physics **10(2)** (1972), 631–702, doi:10.1029/RG010i002p00631.

[75] K. C. Yeh and C. H. Liu, *Radio Wave Scintillation in the Ionosphere*, Proceedings of the IEEE **70(4)** (1982), 324–360, 10.1109/PROC.1982.12313.

[76] K. C. Yeh and G. W. Swenson, *The Scintillation of Radio Signals from Satellites*, Journal of Geophysical Research **64** (1959), 2281–2286, doi:10.1029/JZ064i012p02281.

Vita

Candidate's full name: Sajan Chandra Mushini

University attended:

Chalmers University of Technology, Master of Science, 2005

Nagarjuna University, Bachelor of Technology, 2003

Publications:

Jayachandran, P. T., Hosokawa, K. , Shiokawa, K., Otsuka, Y., Watson, C., **Mushini, S. C.**, MacDougall, J. W., Prikryl, P., Chadwick, R., Kelly, T. (2012), GPS Total Electron Content Variations Associated with Poleward Moving Sun Aligned Arcs, Journal of Geophysical Research, Space Physics, volume. 117, A05310.

Mushini, S. C., Jayachandran, P. T., Langley, R. B., MacDougall, J. W. and Pokhotelov, D. (2011) Improved amplitude and phase scintillation indices derived from wavelet detrended high latitude GPS data, GPS Solutions, Springer Publications, volume 16, issue 3, 363-373, doi: 10.1007/s10291-011-0238-4

Prikryl, P., Jayachandran, P. T., **Mushini, S. C.**, Chadwick, R., (2011), Climatology of GPS phase scintillation and HF radar backscatter for the high-latitude ionosphere under solar minimum conditions, Annals of Geophysics., volume 29, Issue 2, 377 - 392.

Prikryl, P., Jayachandran, P. T., **Mushini, S. C.**, Pokhotelov, D., MacDougall, J. W., Donovan. E., Spanswick, E., and St-Maurice, J. P. (2010), GPS TEC, Scintillations and cycle slips observed at high latitudes during solar minimum, Annals of Geophysics., Volume 28, Issue 6, 1307- 1316.

Mushini, S. C., Jayachandran, P. T., Langley, R. B., MacDougall, J. W. (2009), Use of varying shell heights derived from ionosonde data in calculating vertical total electron content (TEC) using GPS - New method, Journal of Advances in Space Research, Volume 44, Issue 11, 1309-1313.

Jayachandran, P.T., Hosokawa, K., MacDougall, J. W., **Mushini, S. C.**, Langley, R. B., and Shiokawa, K. (2009), GPS total electron content variations associated with a polar cap arc, Journal of Geophysical Research, 114, , A12304, doi:10.1029/2009JA014916.

Jayachandran, P. T., Langley, R. B., MacDougall, J. W., **Mushini, S. C**., Pokhotelov, D., Hamza, A. M., Mann, I. R., Milling, D. K., Kale, Z. C., Chadwick, R., Kelly. T., Danskin, D. W. and Carrano, C. S. (2009), The Canadian high arctic ionospheric network (CHAIN), Radio Science, 44, RS0A03, doi:10.1029/2008RS004046.

Conference Presentations:

Mushini, S. C., Jayachandran, P. T., Langley, R. B., MacDougall, J. W., Prikryl, P. (2012), Canadian High Arctic Ionospheric Network (CHAIN) : A Report, Invited talk at TRANSMIT Summer School, Neustrelitz, Germany.

Mushini, S. C., Jayachandran, P. T., Langley, R. B., MacDougall, J. W. (2011),Climatology of GPS scintillations at high-latitudes in solar minimum, Ionospheric Effects Symposium, Alexandria, USA.

Mushini, S. C., Jayachandran, P. T., Langley, R. B., MacDougall, J. W., and Pokhotelov, D. (2010), Improved amplitude and phase scintillation indices derived from wavelet detrended high latitude GPS data, The International Beacon Satellite Symposium BSS2010, P. Doherty, M. Hernndez-

Pajares, J.M. Juan, J. Sanz and A. Aragon-Angel (Eds.), Campus Nord UPC, Barcelona, Spain.

Mushini, S. C., Jayachandran, P. T., Langley, R. B. and MacDougall, J. W. (2009), Comparison of two phase scintillation estimators for GPS data obtained from high latitudes, DASP, Winter workshop, Banff, Canada.

Mushini, S. C., Jayachandran, P. T., Langley, R. B. and MacDougall, J. W. (2009), Comparison of two phase scintillation estimators for GPS data obtained from high latitudes, AGU Spring meeting, Toronto, Canada.

Mushini, S. C., Jayachandran, P. T., Langley, R. B. and MacDougall, J. W. (2008), Use of varying shell heights derived from ionosonde data in calculating vertical total electron content (TEC) using GPS - New method, , COSPAR General Assembly, Montreal, Canada.

Mushini, S. C., Jayachandran, P. T., Langley, R. B. and MacDougall, J. W. (2008), Use of varying shell heights derived from ionosonde data in calculating vertical total electron content (TEC) using GPS - New method, URSI General Assembly, Chicago, USA.